

# POLITECNICO DI TORINO

Master of Science in Automotive Engineering

Master Thesis

## **Analysis of Turbulent Jet Ignition (TJI) Single-Cylinder Engine through 3D-CFD Simulation**



**Politecnico  
di Torino**

**Supervisors:**

prof. Federico MILLO

Andrea BIANCO

Andrea PIANO

**Candidate:**

Gianmaria DA ROLT

July 2022



# Abstract

In the framework of a continuous strive for better efficiency in internal combustion engines, the Turbulent Jet Ignition (TJI) technology presents itself as a valid option to decrease fuel consumption and emissions. Nevertheless, careful design and optimization is required to fully exploit the advantages of TJI combustion, with 3D-CFD analysis acting as a fundamental tool in this regard. In this context, the present work aims at describing a Turbulent Jet Ignition single cylinder engine with 3D-CFD modelling and was performed in the context of a joint research activity between POWERTECH Engineering and Politecnico di Torino.

The research activity was divided in two parts: the first one focused on in-cylinder simulations and the second one concerning investigations on flame-holes interactions.

As far as in-cylinder simulations are concerned, the main features of TJI combustion were characterized using 3D-CFD for a high speed engine operating point, and a comparison between stoichiometric and lean mixture conditions was carried out and presented in the thesis. A calibration campaign, aimed at improving the accuracy of the model, was then performed focusing on the parameters affected by uncertainties:

- Turbulence: using a Reynolds-Averaged-Navier-Stokes (RANS) simulation approach, the role of the turbulent heat transfer in flame propagation was explored by means of dedicated sensitivity studies
- Pre-Chamber (PC) holes diameter: due to the lack of tomographic data characterizing pre-chamber holes and the possibility of deviations between nominal and effective geometries, the diameter of PC holes was considered uncertain. A sensitivity study of simulation results to PC hole diameter was hence performed.
- PC holes orientation: sensitivity of simulation results to holes orientation was studied, as other researched performed on the same engine suggested the possibility of a positioning error of the pre-chamber holes.

The calibration campaign showed that it was not possible to reproduce experimental average cycles without significative modification of modelling parameters. 3D-CFD results, instead, were able to correctly reproduce fast burning cycles. Additional tests lead to the conclusion that uncertainties and possible errors in boundary conditions are influencing the modelling results. It is also possible, though, that limitations in the adopted modelling methodology, such as the neglect of direct flame-turbulence interaction, are causing differences between experimental average cycles and simulation results. Given that simulation results are, however, representative of fast burning cycles in most of the engine operating conditions, useful information concerning combustion development were obtained. The local conditions within the PC at spark timing and the interaction of turbulent jets with exhaust valves, for example, proved to be two aspects significantly affecting combustion development in PC and Main Chamber (MC) respectively.

As far as flame-holes interactions are concerned, specific studies were carried out in order to characterize the potential flame passage or extinction event in PC holes. The methodology adopted is based on literature evidences showing that the ratio between Laminar Flame Thickness (LFT) and hole diameter is a critical factor differentiating jet ignition and flame ignition within the MC for a specific threshold value. The interaction between a flame and single hole passage was studied in a 3D-CFD model representing a real combustor for which experimental data were available at ambient

pressure. The RANS approach proved to be able to distinguish a jet ignition from a flame ignition event, consistently with experimental data. The ratio of LFT and hole diameter showed differences compared to literature references for such cases, suggesting that a revision of the threshold differentiating jet ignition and flame ignition could be made. Characteristic ratios of LFT and holes diameter were calculated on an extended set of experimental data at ambient pressure and new threshold values differentiating jet ignition and flame ignition were hence defined. Lastly, critical ratios of laminar flame speeds and hole diameters were calculated also in engine cases, and it was found that pressure and temperature levels can significantly modify the value of such ratios compared to ambient conditions. Further studies would be required, though, to further investigate such influence and derive critical threshold of ratios between laminar speeds and PC holes diameters in engine-like conditions.

Dedicated to my dearest friend Tommaso and his family, Sara, Marco and Francesco.  
Friends will be friends, right till the end.



# Table of Contents

|   |    |
|---|----|
| <b>1 Introduction</b> .....   | 7  |
| 1.1 Global Framework and Environmental Issues .....                               | 7  |
| 1.2 Lean Burn Concept .....   | 11 |
| 1.3 Turbulent Jet Ignition.....   | 12 |
| 1.4 Aim Of The Work.....  | 14 |
| <b>2 Methodology</b> .....  | 15 |
| 2.1 In-Cylinder Analysis .....  | 15 |
| 2.1.1 Engine Parameters and Experimental Data .....                               | 15 |
| 2.1.2 Workflow .....  | 18 |
| 2.1.3 1-D Models .....  | 19 |
| 2.1.4 3D-CFD MODEL .....  | 21 |
| 2.2 Flame/Hole Interaction Model.....   | 26 |
| 2.2.1 Literature Research .....   | 26 |
| 2.2.2 Converge Chemistry Tool .....   | 27 |
| 2.2.3 3D-CFD Model .....  | 27 |
| <b>3 Results</b> .....  | 31 |
| 3.1 4000 rpm .....  | 31 |
| 3.1.1 4000 rpm x $\lambda=1$ .....  | 31 |
| 3.1.2 4000 rpm x $\lambda=1.2$ .....  | 45 |
| 3.2 Model Calibration .....   | 53 |
| 3.2.1 Change in Prandtl Number – 4000 rpm x $\lambda=1$ .....                     | 53 |
| 3.2.2 Pre-Chamber Holes Diameter Sweep – 4000 rpm x $\lambda=1$ .....             | 56 |
| 3.2.3 Pre-Chamber Holes Rotation – 4000 rpm .....                                 | 69 |
| 3.2.4 Pre-Chamber Holes Rotation at 2000 rpm – $\lambda=1$ VS $\lambda=1.4$ ..... | 78 |
| 3.3 Effect of Boundary Conditions .....   | 89 |
| 3.4 Flame Hole Interaction.....   | 91 |
| 3.4.1 Flame/Hole Interaction Model.....   | 91 |
| 3.4.2 Application of Mastorakos’ Theory .....                                     | 94 |
| 3.4.3 Extension of Biswas Experiments.....  | 94 |
| 3.4.4 Engine Application .....  | 96 |
| <b>4 Conclusions</b> .....  | 98 |

**Appendix** ..... 100  
    TPA Model (GT-Suite) ..... 100  
**References** ..... 101

# List of Figures

|  |    |
|--|----|
| Figure 1: Share of primary pollutants emissions for different sectors [2] .....  | 7  |
| Figure 2: Examples of Diesel and Gasoline Exhaust Gases Composition [3] .....  | 8  |
| Figure 3: Share of EU CO <sub>2</sub> Emissions by Sector [4] .....  | 9  |
| Figure 4: Global Electric Car Stock from 2010 to 2019 [5] .....  | 9  |
| Figure 5: Prospect on Compressed Natural Gas Demand by Sector [6].....   | 10 |
| Figure 6: CO <sub>2</sub> Reduction Potential for Different Engine Technologies [7].....   | 11 |
| Figure 7: Single-cylinder Engine Representation (without Intake Line), Detail of Pre-Chamber Dimensions (Right), Detail of Holes Orientation (Left)..... | 16 |
| Figure 8: Valve Lift Profiles .....  | 17 |
| Figure 9: 1D-3D Synergy and Workflow .....   | 18 |
| Figure 10: CPOA Model.....   | 20 |
| Figure 11: Embedded Grid, Detail on PC Refinement (Right), Detail on Exhaust Valve and Valve Seat Refinement (Left).....                                 | 22 |
| Figure 12: Example of AMR during Pre-Chamber Combustion.....   | 24 |
| Figure 13: CFD Turbulence Solution Approaches ( [21]) .....  | 25 |
| Figure 14: Experimental Setup used in [26] .....   | 28 |
| Figure 15: Flame/Hole Interaction Model .....  | 28 |
| Figure 16: Starting Mesh (left) and Non-Orthogonality (right).....   | 29 |
| Figure 17: 4000 rpm x $\lambda=1$ – Gas Exchange Process .....   | 32 |
| Figure 18: 4000 rpm x $\lambda=1$ – Intake Mass Comparison (TPA vs 3D-CFD).....  | 32 |
| Figure 19: 4000 rpm x $\lambda=1$ - Pressure and HRR Profiles .....  | 33 |
| Figure 20: 4000 rpm x $\lambda=1$ – Mass Fraction Burned.....  | 34 |
| Figure 21: 4000 rpm x $\lambda=1$ - Residuals and Intake Charge Mass Fractions inside PC .....   | 35 |
| Figure 22: 4000 rpm x $\lambda=1$ - Residuals and Intake Mass inside PC.....   | 35 |
| Figure 23: 4000 rpm x $\lambda=1$ - Residuals Distribution inside PC at 25 CAD BTDC.....   | 36 |
| Figure 24: 4000 rpm x $\lambda=1$ - SP Residuals Distribution.....   | 36 |
| Figure 25: 4000 rpm x $\lambda=1$ – Turbulent Kinetic Energy (PC Average and Spark Plug).....  | 37 |
| Figure 26: 4000 rpm x $\lambda=1$ - Turbulent Kinetic Energy Distribution in PC at 25 CAD BTDC.....  | 38 |
| Figure 27: 4000 rpm x $\lambda=1$ - Turbulent Kinetic Energy Distribution along PC at 25 CAD BTDC..  | 38 |
| Figure 28: 4000 rpm x $\lambda=1$ – PC Flame Propagation .....   | 39 |
| Figure 29: 4000 rpm x $\lambda=1$ – PC Flame Propagation Features.....   | 39 |
| Figure 30: 4000 rpm x $\lambda=1$ – PC Combustion and Jet Injection.....   | 40 |

|  |    |
|--|----|
| Figure 31: 4000 rpm x $\lambda=1$ – PC/MC Pressure Profiles and Mass Flow Rate .....                                       | 41 |
| Figure 32: 4000 rpm x $\lambda=1$ – Jet and Flame Propagation in MC represented by gas iso-surface at T=1700 K.....        | 41 |
| Figure 33: 4000 rpm x $\lambda=1$ – Cylinder TKE Distribution (3D View) .....  | 42 |
| Figure 34: 4000 rpm x $\lambda=1$ – Cylinder TKE Distribution (Slices).....  | 42 |
| Figure 35: 4000 rpm x $\lambda=1$ – MC to PC mass flow rate and PC HRR.....  | 43 |
| Figure 36: 4000 rpm x $\lambda=1$ – Flow Reversal (OH and TKE Distribution).....   | 44 |
| Figure 37: 4000 rpm x $\lambda=1.2$ - Pressure and HRR Profiles .....  | 45 |
| Figure 38: 4000 rpm x $\lambda=1.2$ – Mass Fraction Burned.....  | 46 |
| Figure 39: 4000 rpm x $\lambda=1$ VS 4000 rpm x $\lambda=1.2$ - Residuals and Intake Mass Fraction inside PC               | 47 |
| Figure 40: 4000 rpm x $\lambda=1$ VS 4000 rpm x $\lambda=1.2$ - Residuals and Intake Mass inside PC .....                  | 47 |
| Figure 41: Residuals Distribution - 4000 rpm x $\lambda=1$ (left) VS 4000 rpm x $\lambda=1.2$ (right) .....                | 48 |
| Figure 42: 4000 rpm x $\lambda=1$ VS 4000 rpm x $\lambda=1.2$ – Turbulent Kinetic Energy (PC Average and Spark Plug).....  | 49 |
| Figure 43: Turbulent Kinetic Energy Distribution - 4000 rpm x $\lambda=1$ (left) VS 4000 rpm x $\lambda=1.2$ (right) ..... | 50 |
| Figure 44: 4000 rpm x $\lambda=1.2$ – PC Flame Development.....  | 50 |
| Figure 45: 4000 rpm x $\lambda=1.0$ VS 4000 rpm x $\lambda=1.2$ – PC and MC Pressure .....                                 | 51 |
| Figure 46: 4000 rpm x $\lambda=1.0$ VS 4000 rpm x $\lambda=1.2$ – PC HRR and Mass Flow Rate.....                           | 52 |
| Figure 47: 4000 rpm x $\lambda=1.0$ – Main Chamber Pr Sweep .....  | 54 |
| Figure 48: 4000 rpm x $\lambda=1.0$ – Pre-Chamber Hole Diameter Sweep.....   | 56 |
| Figure 49: Holes Diameter Sweep – PC Residuals and Intake Concentration .....  | 57 |
| Figure 50: Holes Diameter Sweep – PC Residuals and Intake Mass.....  | 57 |
| Figure 51: Holes Diameter Sweep – Mach Number through PC Holes .....   | 58 |
| Figure 52: Holes Diameter Sweep – PC Residuals Distribution .....  | 59 |
| Figure 53: Holes Diameter Sensitivity – PC Scavenging .....  | 60 |
| Figure 54: Holes Diameter Sweep – TKE (PC Avg. and Spark Plug).....  | 60 |
| Figure 55: Holes Diameter Sweep – PC TKE Distribution .....  | 61 |
| Figure 56: Holes Diameter Sensitivity – PC TKE .....   | 62 |
| Figure 57: Holes Diameter Sweep – PC and MC Pressure.....  | 62 |
| Figure 58: Holes Diameter Sweep – MC/PC Mass Flow Rate and Mach Number .....   | 64 |
| Figure 59: Holes Diameter Sweep – Jet Injection Characterization .....   | 65 |
| Figure 60: Holes Diameter Sensitivity – Jet Injection Phases .....   | 66 |
| Figure 61: Holes Diameter Sweep – PC HRR (Shifted Profiles) .....  | 67 |

|  |    |
|--|----|
| Figure 62: Holes Diameter Sweep – MC/PC Mass Flow Rate and PC HRR.....   | 67 |
| Figure 63: Holes Diameter Sensitivity – Flow Reversal (Peak MFR and Peak HRR).....                                 | 68 |
| Figure 64: Pre-Chamber Holes Orientation - Baseline (left) VS Rotated (right) .....                                | 69 |
| Figure 65: 4000 rpm x $\lambda=1$ Holes Rotation – Pressure and HRR Profiles .....                                 | 69 |
| Figure 66: 4000 rpm x $\lambda=1$ Holes Rotation – PC Residuals and Intake Concentration .....                     | 70 |
| Figure 67: 4000 rpm x $\lambda=1$ Holes Rotation – PC Residuals and Intake Mass.....                               | 70 |
| Figure 68: PC Residuals Distribution – Baseline (left) VS Rotated Holes (right) .....                              | 71 |
| Figure 69: 4000 rpm x $\lambda=1$ Holes Rotation – PC TKE.....   | 72 |
| Figure 70: PC TKE Distribution – Baseline (left) VS Rotated Holes (right) .....                                    | 72 |
| Figure 71: 4000 rpm x $\lambda=1$ Holes Rotation – PC TKE on Holes Cross-Sections .....                            | 73 |
| Figure 72: 4000 rpm x $\lambda=1$ Holes Rotation – PC HRR and MC/PC Mass Flow Rate .....                           | 74 |
| Figure 73: Jet Exit – Baseline (left) VS Rotated Holes (right) .....   | 74 |
| Figure 74: 4000 rpm x $\lambda=1$ Holes Rotation – Residuals Distribution and Early Flame Development .....        | 75 |
| Figure 75: 4000 rpm x $\lambda=1$ Holes Rotation – Turbulent Jet Impact.....                                       | 75 |
| Figure 76: 4000 rpm x $\lambda=1$ Holes Rotation – Heat Release Rate (Zoomed).....                                 | 76 |
| Figure 77: 4000 rpm x $\lambda=1$ Holes Rotation – Heat Transfer to Exhaust Valves .....                           | 76 |
| Figure 78: 4000 rpm x $\lambda=1$ Holes Rotation – Average In-Cylinder TKE .....                                   | 77 |
| Figure 79: 2000 rpm x $\lambda=1$ Holes Rotation – Pressure and HRR Profiles .....                                 | 78 |
| Figure 80: 2000 rpm x $\lambda=1.4$ Holes Rotation – Pressure and HRR Profiles .....                               | 78 |
| Figure 81: 2000 rpm Holes Rotation – $\lambda=1.0$ (left) VS $\lambda=1.4$ (right) PC Scavenging .....             | 79 |
| Figure 82: 2000 rpm Holes Rotation – $\lambda=1.0$ (left) VS $\lambda=1.4$ (right) PC Residuals Distribution ..... | 79 |
| Figure 83: 2000 rpm Holes Rotation – $\lambda=1.0$ (left) VS $\lambda=1.4$ (right) PC TKE .....                    | 80 |
| Figure 84: 2000 rpm Holes Rotation – $\lambda=1.0$ (left) VS $\lambda=1.4$ (right) PC TKE Distribution.....        | 80 |
| Figure 85: 2000 rpm $\lambda=1.0$ Holes Rotation – Baseline TKE.....   | 81 |
| Figure 86: 2000 rpm $\lambda=1.0$ Holes Rotation – Rotated Holes TKE.....  | 81 |
| Figure 87: 2000 rpm Holes Rotation – $\lambda=1.0$ (left) VS $\lambda=1.4$ (right) PC/MC Pressure Traces .....     | 82 |
| Figure 88: 2000 rpm Holes Rotation – $\lambda=1.0$ (left) VS $\lambda=1.4$ (right) PC HRR.....                     | 82 |
| Figure 89: Flow Reversal – 2000 rpm x $\lambda=1.0$ (left) VS 4000 rpm x $\lambda=1.0$ (right) .....               | 83 |
| Figure 90: 4000 rpm x $\lambda=1.0$ Flow Reversal Characterization.....  | 84 |
| Figure 91: Fuel Flow Reversal – 2000 rpm x $\lambda=1.0$ VS 4000 rpm x $\lambda=1.0$ .....                         | 84 |
| Figure 92: Exhaust Valve Interaction 2000 rpm VS 4000 rpm – Thermal Effect .....                                   | 85 |
| Figure 93: 2000 rpm VS 4000 rpm – PC Combustion and Jet Exit Temperature .....                                     | 86 |
| Figure 94: Exhaust Valve Interaction 2000 rpm VS 4000 rpm – Turbulence Effect .....                                | 86 |

|   |    |
|---|----|
| Figure 95: Exhaust Valve Interaction 2000 rpm $\lambda=1.0$ VS $\lambda=1.4$ – Thermal Effect .....   | 87 |
| Figure 96: Exhaust Valve Interaction 4000 rpm $\lambda=1.0$ VS $\lambda=1.2$ – Thermal Effect .....   | 88 |
| Figure 97: Exhaust Valve Interaction 2000 rpm $\lambda=1.0$ VS $\lambda=1.4$ – Turbulence Effect .....  | 88 |
| Figure 98: Exhaust Valve Interaction 4000 rpm $\lambda=1.0$ VS $\lambda=1.2$ – Turbulence Effect .....  | 89 |
| Figure 99: 3000 rpm x $\lambda=1$ (left) VS 3000 rpm x $\lambda=1$ (right) .....  | 89 |
| Figure 99: Jet Ignition Model - Top: Temperature; Middle: OH Mass Fraction; Bottom: Chemical Source; Delta-time values refer to time passed after spark timing .....    | 91 |
| Figure 100: Jet Ignition Model - Top: Temperature; Middle: OH Mass Fraction; Bottom: Chemical Source; Delta-time values refer to time passed after spark timing .....   | 92 |
| Figure 101: Jet Ignition Model - Top: Temperature; Middle: OH Mass Fraction; Bottom: Chemical Source; Delta-time values refer to time passed after spark timing .....   | 93 |
| Figure 102: Flame Ignition Model - Top: Temperature; Middle: OH Mass Fraction; Bottom: Chemical Source; Delta-time values refer to time passed after spark timing ..... | 93 |
| Figure 103: Experimental results concerning flame-hole interaction in straight channels as a function of diameter and equivalence ratio ( [26]).....                    | 95 |
| Figure 104: Results of $2*LFT/d$ analysis, with Expected Outcome (color) and Phenomenological Evidence (dashed shapes) .....  | 95 |

# List of Tables

|   |    |
|---|----|
| Table 1: Engine Data.....   | 15 |
| Table 2: Pre-Chamber Data.....  | 16 |
| Table 3: List of Performed Tests.....   | 17 |
| Table 4: Valve Openings and Closures.....   | 18 |
| Table 5: Fixed Embedding Scales and Resulting Grid Size .....   | 23 |
| Table 6: AMR Settings .....   | 23 |
| Table 7: Fuel Surrogate Composition .....   | 25 |
| Table 8: Test Cases (extracted from [26]) .....   | 26 |
| Table 9: Methane Fuel Surrogate.....  | 27 |
| Table 10: General Setup for Converge Chemistry Tool (One-D Premixed Laminar Flame).....               | 27 |
| Table 11: Flame/Hole Interaction Model Fixed Embeddings.....  | 30 |
| Table 12: Flame/Hole Interaction Model AMR Settings.....  | 30 |
| Table 8: 4000 rpm x $\lambda=1$ – Burn Duration.....  | 34 |
| Table 14: 4000 rpm x $\lambda=1$ – PC Scavenging .....  | 37 |
| Table 15: 4000 rpm x $\lambda=1$ – PC Turbulent Kinetic Energy .....                                  | 37 |
| Table 16: 4000 rpm x $\lambda=1.2$ – Burn Duration.....   | 46 |
| Table 17: 4000 rpm x $\lambda=1$ VS 4000 rpm x $\lambda=1.2$ – PC Scavenging .....                    | 48 |
| Table 18: 4000 rpm x $\lambda=1$ VS 4000 rpm x $\lambda=1.2$ – PC TKE .....                           | 49 |
| Table 19: 4000 rpm x $\lambda=1.0$ VS 4000 rpm x $\lambda=1.2$ – Jet Injection .....                  | 51 |
| Table 20: 4000 rpm x $\lambda=1.0$ VS 4000 rpm x $\lambda=1.2$ – Flow Reversal.....                   | 52 |
| Table 21: Holes Diameter Sweep – PC Scavenging.....   | 58 |
| Table 22: Holes Diameter Sweep – Pre-Chamber TKE .....  | 61 |
| Table 23: Holes Diameter Sweep – Jet Injection.....   | 64 |
| Table 24: Holes Diameter Sweep – Jet Injection Phases .....   | 66 |
| Table 25: Holes Diameter Sweep – Flow Reversal .....  | 68 |
| Table 26: PC Holes Rotation – PC Scavenging.....  | 71 |
| Table 27: PC Holes Rotation – PC Turbulent Kinetic Energy .....                                       | 73 |
| Table 28: 2000 rpm PC Holes Rotation – PC Scavenging .....  | 80 |
| Table 29: 2000 rpm PC Holes Rotation – PC TKE .....   | 81 |
| Table 30: Flow Reversal Peak HRR and MFR – 2000 rpm x $\lambda=1.0$ VS 4000 rpm x $\lambda=1.0$ ..... | 83 |
| Table 31: Effect of Boundary Conditions .....   | 90 |
| Table 31: Jet Ignition and Flame Ignition Model Results.....  | 94 |
| Table 32: Mastorakos Methodology and Engine Application .....   | 96 |

# List of Acronyms

|      |   |
|------|---|
| AMR  | Adaptive Mesh Refinement                |
| ATS  | After-Treatment Systems                 |
| BTDC | Before Top Dead Center                  |
| CAD  | Crank Angle Degrees                     |
| CNG  | Compressed Natural Gas                  |
| CPOA | Cylinder Pressure Only Analysis         |
| EVC  | Exhaust Valve Closure                   |
| EVO  | Exhaust Valve Opening                   |
| FMEP | Friction Mean Effective Pressure        |
| GHG  | Green House Gases                       |
| HC   | Unburned Hydrocarbons                   |
| HCCI | Homogeneous-Charge Compression Ignition |
| HRR  | Heat Release Rate                       |
| ICE  | Internal Combustion Engine              |
| IMEP | Indicated Mean Effective Pressure       |
| IVC  | Intake Valve Closure                    |
| IVO  | Intake Valve Opening                    |
| LFT  | Laminar Flame Thickness                 |
| MC   | Main Chamber                            |
| MON  | Motor Octane Number                     |
| NEDC | New European Driving Cycle              |
| PC   | Pre-Chamber                             |
| RON  | Research Octane Number                  |
| SI   | Spark Ignition                          |
| SOI  | Start of Injection                      |
| SP   | Spark Plug                              |
| ST   | Spark Timing                            |
| TJI  | Turbulent Jet Ignition                  |
| TKE  | Turbulent Kinetic Energy                |
| TPA  | Three-Pressure Analysis                 |
| TWC  | Three-Way Catalyst                      |

# Chapter 1

## Introduction

### 1.1 Global Framework and Environmental Issues

The framework into which this work is realized is characterized by an increasing concern for the impact of the human footprint on the environment. In particular, nowadays, road transportation, whether public or private, represents a great matter of discussion and improvement when considering its wide presence and its effects on pollution and global warming.

The environmental impact of this sector, which today is heavily relying on the Internal Combustion Engine (ICE) and is expected to still rely on it in the near future ([1]), comes in the form of three main types of emissions as shown in Figure 1. Besides abrasion emissions (i.e.: emission coming from wear and corrosion of components, such as brakes and clutches) and evaporative emissions (i.e.: emissions of fuel vapors escaping the fuel tank and fuel line), exhaust emissions, described in the following, are of particular interest, as they are subject to strict regulations and play a major role in global environmental issues.

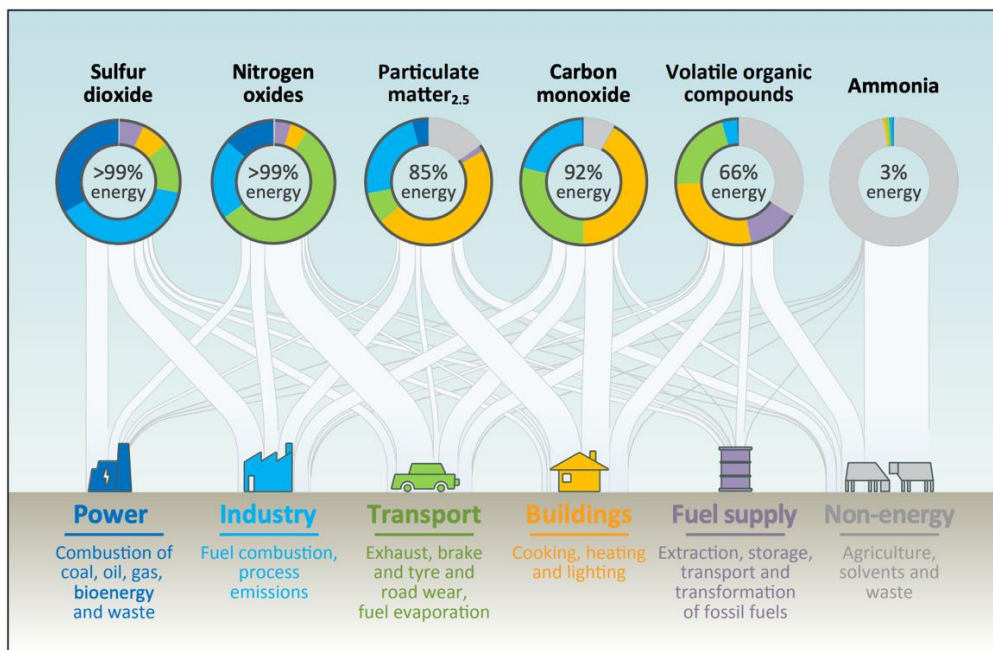


Figure 1: Share of primary pollutants emissions for different sectors [2]

A first drawback implied in the usage of ICEs is the emission of harmful substances coming from incomplete combustion or from secondary reactions taking place in the combustion chamber (Figure 2). Products such as CO, NO<sub>x</sub>, unburnt Hydrocarbons (HC), SO<sub>x</sub> are dangerous due to their health-threatening potential. Furthermore, such species are also known as primary pollutants, due to their role as root cause for other environmentally harmful phenomena (i.e. acid rains and photochemical

smog). Even though these compounds make for 1% of the total products of the combustion process, they are the subject of severe limitations imposed by the legislations.

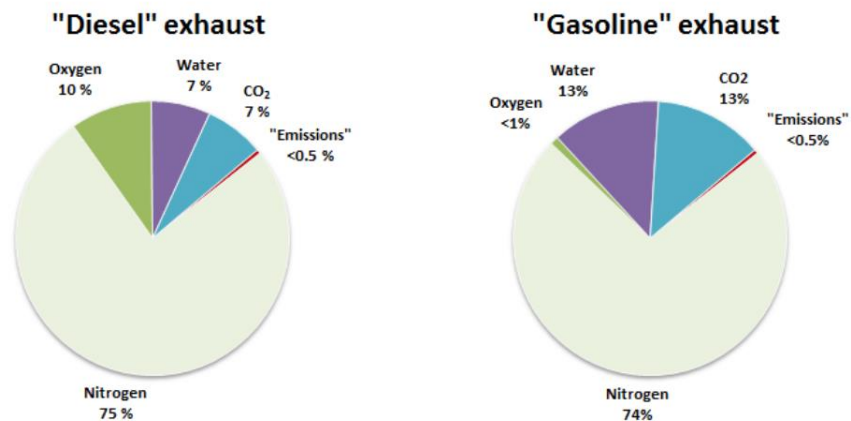


Figure 2: Examples of Diesel and Gasoline Exhaust Gases Composition [3]

As a matter of fact, through the years, the strive for lower pollutant emissions has been one of the main drivers for technological innovations in the automotive field. Generally, this issue can be faced in two ways: by working on the exhaust gases themselves, or by working on the combustion process (which can be thought as the “cause” of said exhaust gases). To quote an example for the first case, one could refer to introduction, in the last 40 years, of the After Treatment System (ATS, like the Three Way Catalyst, TWC, or the Selective Catalytic Reducer, SCR), aimed at the dissolution of pollutants exploiting either oxidation or reduction reactions.

As for an example of the second strategy, instead, Exhaust Gas Recirculation can be mentioned. In this case, burnt products are being recirculated in the combustion chamber in order to dilute reacting mixture, increase its thermal capacity, lower the temperature in the chamber and hence leading to lower formation of NO<sub>x</sub>. In this regard, another promising technology for the reduction of NO<sub>x</sub> is lean burn technology, for which Turbulent Jet Ignition (TJI) is a key enabler. More details concerning TJI technology, the main topic of this research, will be provided in the following section.

Recently, more and more concern has been expressed for CO<sub>2</sub>. Indeed, a special consideration is to be made for carbon dioxide, as while it is not categorized as a primary pollutant (and as a matter of fact, it creates no harm to human health if present in a reasonable quantity), it is still subjected to very strict regulations. In fact, carbon dioxide plays a major role in global warming, being one of the main gases contributing to the greenhouse effect. Consequently, the transportation sector is particularly affected by this evidence, as it proved to be one of the main generators of CO<sub>2</sub> emissions (for example, it accounts for one third of the European CO<sub>2</sub> emission [4], as shown in Figure 3).

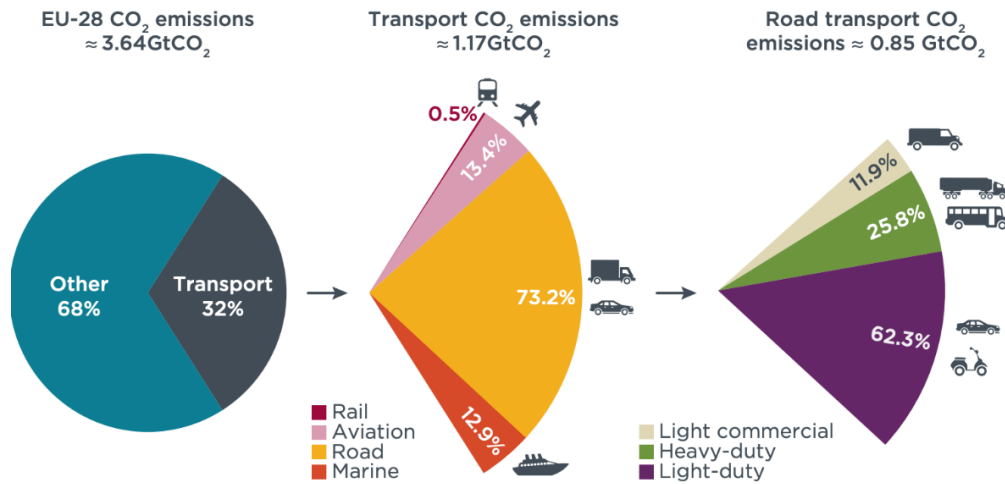


Figure 3: Share of EU CO<sub>2</sub> Emissions by Sector [4]

For this reason, a much stricter regulation has been introduced since 2020 for car manufacturers, lowering the target CO<sub>2</sub> emission limit to respect from 135 g/km to 95 g/km (based on the New European Driving Cycle, NEDC), with a penalty for each gram exceeding this limit of 95 € per vehicle sold.

However, CO<sub>2</sub> is a product of the ideal combustion process and, as such, it should be a compound gladly seen in the exhaust gas, as it is a sign of completed combustion. This fact opens an interesting consideration to be made for carbon dioxide. Since it cannot be treated by the ATS, there are only three ways to reduce its production:

- i. Adopting a solution limiting the usage of the ICE: this strategy is the cause of the recent increase in hybrid vehicles and electric vehicles proposals from car manufacturers (Figure 4). Electric vehicles and hybrid vehicles which have the ability to switch to full E-drive (like Plug-in Hybrid Electric Vehicles) are an attractive solution for car manufacturers due to their very low Tank-To-Wheel emissions;

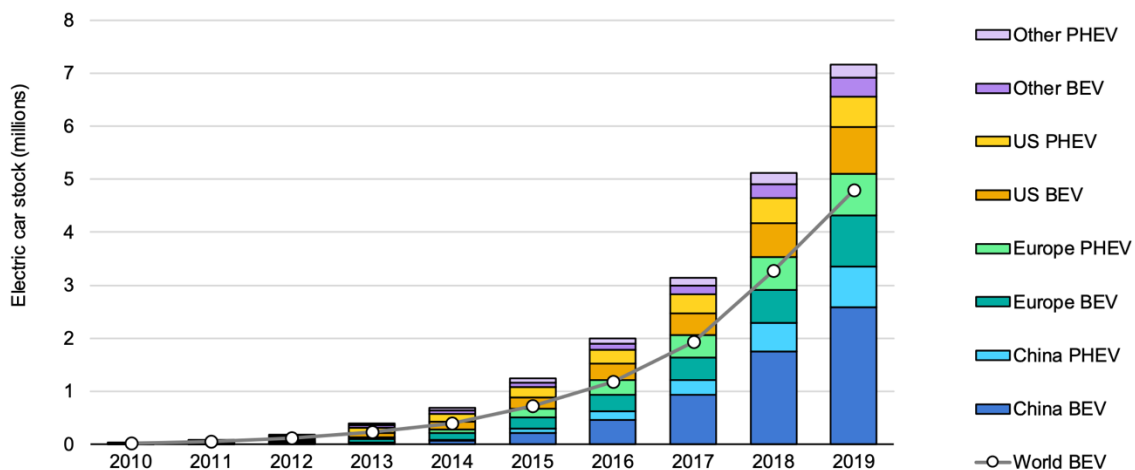


Figure 4: Global Electric Car Stock from 2010 to 2019 [5]

- ii. Using a fuel with low carbon content: alternative fuels are an interesting substitute to common fuels, due to their potential in reducing GHG emissions. The most established alternative is Natural Gas, a mixture of gases predominantly made of methane (80-99% of the total), which offers a similar performance to common fuels, but with lower carbon content, thus leading to

lower carbon dioxide production. CNG (Compressed Natural Gas) is set to have a large increase in demand thanks to an increase of application in the transportation sector.

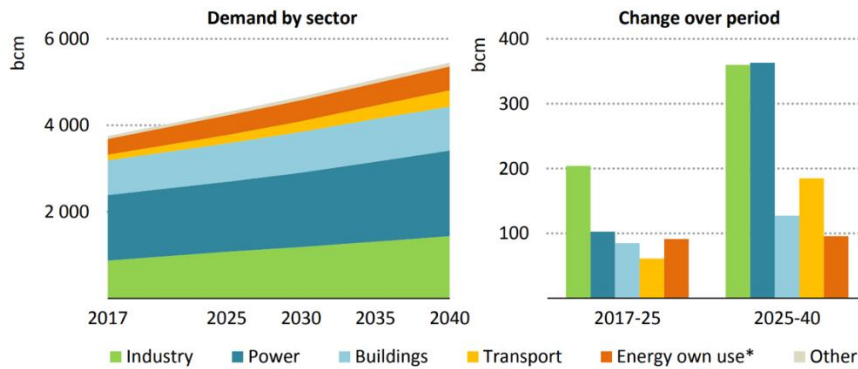


Figure 5: Prospect on Compressed Natural Gas Demand by Sector [6]

Biofuels, like bioethanol and biodiesel, have benefits in terms of their renewability, but have different corrosion characteristics with respect to common fuels that limits their application on existing engines. A zero-carbon alternative is hydrogen, which despite its huge potential is not widely used so far due to equally huge drawbacks in terms of storage, production and distribution.

- iii. Using less fuel for the same power output or, in other words, to increase the engine efficiency. Even though the Internal Combustion Engine was subjected to a lot of innovation aiming at higher efficiency throughout its long history, there is still big room for improvement in this field, especially considering that almost only one third of the total energy available in the combustion chamber is really exploited for work. New technologies and operational strategies, such as cylinder deactivation, HCCI, Lean Burn and TJI, listed in Figure 6, are aiming the strive for higher efficiency, lower fuel consumption and lower emissions, by improving the quality and performance of the combustion process. Nevertheless, while some of these technologies are already available in current production engines, such as cylinder deactivation and advanced stop-start for example, some of them require further development and optimization in order to be widely adopted. In this framework, tools such as 3D-CFD analysis are fundamental for proper design and optimization of such technologies. For said reasons, the ICE can still be considered a valid technology in an environment with the growing competition of Battery Electric Vehicles.

| Engine Technology   | CO <sub>2</sub> Reduction Potential |
|---|-------------------------------------|
| Baseline: GDI, turbo, stoichiometric                        | 0                                   |
| Atkinson cycle (+VVT)                                       | 3–5%                                |
| Advanced start-stop   | 2–5%                                |
| Dynamic cylinder deactivation + Mild hybrid or Miller cycle | 10–15%                              |
| Lean-burn GDI   | 10–20%                              |
| Variable CR   | 10%                                 |
| GCI   | 15–25%                              |
| Water Injection   | 5–10%                               |
| Homogeneous Lean  | 15–20%                              |
| Dedicated EGR   | 15–20%                              |
| RCCI  | 20–30%                              |
| Two-stroke opposed piston diesel                            | 25–35%                              |

Figure 6: CO<sub>2</sub> Reduction Potential for Different Engine Technologies [7]

In this framework, the present work focuses on Turbulent Jet Ignition, a technology exploiting the concept of lean burning combustion to improve engine efficiency.

## 1.2 Lean Burn Concept

The core of the operation of an Internal Combustion Engine is certainly the combustion process. The most simplified illustration of such process describes an exothermal chemical reaction between air and a hydrocarbon species, giving as products carbon dioxide and water. For each fuel, a stoichiometric Air-to-Fuel Ratio (A/F Ratio) can be found, defining the relative quantity of air and fuel for which the combustion process is completed (i.e.: all the reactants become products). Depending on the operating conditions, an ICE can be operated in with a lean or rich mixture, meaning that the air/fuel mix shows, respectively, an excess of air or an excess of fuel. Lean and rich operation can be also defined in terms of the dilution ratio  $\lambda$ , which is the ratio of the operational A/F Ratio and the stoichiometric A/F Ratio; thus, lean operation will be characterized by  $\lambda > 1$ , while rich operation will be characterized by  $\lambda < 1$ .

Despite the advantages and the disadvantages that both dilution levels have, the lean operation range is of particular interest, as it can, in principle, lead to an increase in efficiency, with a consequent benefit in terms of fuel consumption. This is achieved thanks to two different effects:

- 1.1 the higher presence of air in the mixture increases the specific gas constant for the reacting gases, giving an immediate increase in efficiency of the ideal Otto cycle.
- 1.2 possibility to control engine load without using a throttle valve. In a conventional SI engine, mostly operated with a stoichiometric mixture, the load is controlled by adjusting a throttle valve, reducing the flow area for the intake air. Unfortunately, this is an inefficient way of controlling the engine load, since the work required to intake air across a restriction is directly drained from the total work obtained from the complete engine cycle (this is the so called “pumping work” the work required from the engine, thus not useful, to exchange the gases involved in the engine cycle). In the hypothesis that an engine can burn lean mixtures in a wide

lean operation range, however, load control could be directly obtained by controlling the amount of injected fuel per cycle, rather than acting on both air and fuel quantities; this fact would remove the necessity of throttling the intake, effectively decreasing the pumping work required, thus leading to better engine efficiency ([8]).

The effects of lean burning extend also to engine emissions. The relationship between fuel consumption and CO<sub>2</sub> emissions was already highlighted previously: considering the benefits in lower fuel consumption, lower CO<sub>2</sub> emissions are to be expected in a scenario of lean burning strategy.

An additional consequence of higher air (and, thus, oxygen) availability is the higher likelihood of oxidation of compounds such as carbon monoxide and unburned hydrocarbons, with a consequent decrease in their emission.

Furthermore, dilution has an impact on in-cylinder temperatures, which are lowered as an outcome of the presence of species not participating in the combustion process and absorbing part of the heat released by it. In a scenario of sufficient dilution level, this effect has an impact on the heat rejected towards engine walls, which is reduced, and on the formation and emission of NO<sub>x</sub> species, which are particularly sensitive to high temperatures due to the high activation energy required to break nitrogen molecules. In particular, NO<sub>x</sub> emissions would become negligible for dilution levels able to achieve peak in-cylinder temperatures below 1800 K [9].

Although these advantages may sound very attractive, lean mixture operation shows also some major drawbacks that hindered its widespread application so far. The first reason for such a statement is that at high dilution ratios the lower presence of fuel reduces the ignitability of the mixture and increases the possibility of a misfiring cycle to occur if conventional spark-plug are used, representing a serious issue for the emission of HC. To solve this problem, a possible solution is to adopt innovative ignition systems, such as Torch Ignition or Turbulent Jet Ignition systems, which are able to significantly reduce misfiring occurrence even at very high dilution ratios.

Another drawback of lean combustion is that the velocity at which the flame propagates during the combustion process decreases for leaner and leaner mixtures. This evidence is followed by a higher probability of flame extinction before all the reactants are consumed, leading to higher HC emissions and cycle-to-cycle variation. These drawbacks can be avoided either by re-calibrating the timing of spark discharge or by adopting a technology capable of increasing the flame front surface with respect to conventional systems. Turbulent Jet Ignition, as it will be described in the next section, belongs to this last group of technologies, and has shown great potential in reducing the effects of slow flame propagation.

As a final note, the consistent operation in the  $\lambda > 1$  range represents a problem for the exploitation of a commonly used ATS such as the TWC, which requires a close-to-stoichiometric operation in order to successfully fulfill its task in reducing nitrogen oxides and oxidizing carbon monoxide and unburnt hydrocarbons ([10]). Thus, to comply with emission regulations, an always-lean operated ICE would need to either use a specifically designed After-Treatment System, or to reach sufficiently low emissions of NO<sub>x</sub> on its own ([11]).

### **1.3 Turbulent Jet Ignition**

Turbulent Jet Ignition is a technology capable of overcoming the criticalities discussed in the previous section and, thus, capable of exploiting the Lean Burn strategy in an effective way.

The main feature of this system is the implementation of a Pre-Chamber (PC), a small volume (typically 1-5% of the clearance volume) connected to the main cylinder chamber (also referred to as Main Chamber, MC) by means of small holes. The pre-chamber hosts the spark plug, used to initiate the combustion process, and can host or not a secondary injector; based on the way the PC is fueled the operation of a TJI system can be classified as “active”, if the PC is fueled by an injector located in it, or “passive”, if the PC is fueled by the charge coming from the main chamber during the compression stroke. Given the aforementioned definition, it is worth highlighting that an active PC can be operated effectively as an active PC or a passive PC depending on the engine control strategy and, for example, on the working conditions of the engine; for example, the active solution might be more suitable for low load operation (when the MC charge is lean), so to achieve a stoichiometric, ignitable mixture around the spark plug located in the pre-chamber; by contrast, the passive operation might be used at high load, where the main charge is already close to stoichiometric levels. It is worth highlighting that the previous examples are not comprehensive of all the options involved in TJI utilization.

The functioning of a TJI system, as hinted previously, is in principle similar to the one of a conventional SI engine: the combustion process in the PC is initiated by means of a spark, which leads to the development and propagation of a flame front inside the pre-chamber. The earlier part of the PC combustion shows an increase in pressure that pushes cold, unburnt gases into the main chamber ([11], [12]). Once the flame reaches the small holes, a quenching phenomenon occurs due to high flame stretch and heat loss to the walls, leading to the extinction of the flame and the emission, due to the higher pressure in the pre-chamber, of hot jets made primarily of incomplete combustion products and radicals. The injection of hot jets in the main chamber creates multiple sites at which ignition may take place, thanks to two relevant phenomena (as proved in [13]): a turbulent effect and a chemical effect. The first effect contributes to the start of combustion in the main chamber due to the mixing of high temperature products with the fresh charge; the second one contributes to the ignition of the main charge due to the chemical activation led by the presence of radicals. In the case of active pre-chamber operation, [14] also adds a third effect coming from the difference in mixture composition between main chamber and pre-chamber: the enrichment effect, by which main-chamber ignition is also affected by the injection of unburned, rich pre-chamber mix that creates a local decrease in dilution ratio. The combination of these effects leads to multiple ignition points, from which a flame develops consuming the main chamber mixture in a faster and more homogeneous way compared to conventional SI engine. This was proved to lead to an expansion of the lean burn limit of the propulsion system ([15])

Furthermore, it must also be highlighted that the adoption of an active pre-chamber operation expands even more the lean burn limit, as it allows in principle to decouple MC and PC combustion events, hence granting the possibility to start combustion in the best possible conditions in both PC and MC, with benefits in terms of ignition success, quality of the combustion process and, summarizing, operational stability ([15], [16]).

The adoption of TJI, as anticipated, allows to overcome the two drawbacks involved with Lean Burn. Indeed, the exploitation of multiple turbulent jets made of reactive species allows to obtain better ignitability of the lean mixture., significantly decreasing the probability of a misfiring event. Moreover, the turbulence levels reached due to the jet injection increases the burning speed of the flame front, countering the lower speeds characterizing the combustion events of leaner mixtures.

Ultimately, these features have been proved to effectively exploit the benefit of the Lean Burn strategy.

## **1.4 Aim Of The Work**

The aim of the present work is to investigate by means of 3D-CFD modelling the performance of a single cylinder engine exploiting the Turbulent Jet Ignition technology. In addition, an investigation was made concerning the interactions between flames and pre-chamber holes, in order to assess possible flame extinction or flame reaching the main combustion chamber.

The main aspects related to the analyzed data and exploited methodology are found in Chapter 2. Chapter 3 instead reports the results with detailed comments concerning the most interesting outcomes of the studies. The main analysis on the TJI engine was performed at a medium-high rotational speed of 4000 rpm, both in stoichiometric and lean conditions, for which a first investigation is presented in section 3.1. A calibration campaign based on the uncertainties featured in the model is performed in section 3.2, with an insight on turbulence modelling and geometry sensitivity. Moreover, Section 3.3 will underline instead the impact of boundary conditions on the numerical model. Lastly, an insight on the interaction between wall and turbulent flame will be presented in section 3.4, trying to address the outcome of such interaction in terms of flame extinction or flame passage. Investigations will range from engine conditions to the laboratory experiments, in an attempt to link the two very different conditions using a similar methodology. These analyses will consider both a 1D approach and a 3D-CFD approach, for which results are presented in section 3.4.

# Chapter 2

## Methodology

The current section contains the description of the experimental tests and numerical setup, with a focus on the steps followed during the whole study. At first, the experimental setup is described, with data coming from laboratories in which the tests were performed. A discussion regarding the 1D engine model is also presented, as it is a key component in the workflow allowing the definition of boundary conditions used in the 3D-CFD model. At last, the developed 3D-CFD model is described, starting from the models used up to the numerical and computational aspects.

### 2.1 In-Cylinder Analysis

#### 2.1.1 Engine Parameters and Experimental Data

The engine under study is a single cylinder engine equipped with a pre-chamber. The main engine data are reported in Table 1.

The main chamber is fed with a Port Fuel Injection (PFI) system, with a gasoline injector positioned between intake manifold and intake ports. A second injector (providing an injection of Compressed Natural Gas) is located in the pre-chamber, thus allowing in principle the operation of the TJI system in active mode. However, for the analyzed cases, only the passive mode operation was exploited.

| Engine Data       |                  |
|-------------------|------------------|
| Stroke            | 60 mm            |
| Bore              | 72 mm            |
| Compression Ratio | 10.5             |
| Displacement      | 244 cc           |
| Max Power         | 16 kW @ 8000 rpm |
| Max Torque        | 20 Nm @ 5500 rpm |

Table 1: Engine Data

The pre-chamber was specially designed to be mounted in place of a spark plug used on an older version of the engine, without any change in the cylinder head design. The result, as pictured in Figure 7, is a tilted pre-chamber with the holes region centered along the cylinder axis. Table 2 contains the main pre-chamber data, while Figure 7 completes the dimensional description of the pre-chamber, as well as indicating the orientation of the four PC holes.

| Pre-Chamber Data                            |               |
|---|---------------|
| Volume                                      | 1845.9 $mm^3$ |
| Holes Diameter                              | 1 mm          |
| Holes Length                                | 1 mm          |
| Number of Holes                             | 4             |
| Vol <sub>PC</sub> /Vol <sub>Clearance</sub> | 7.20%         |

*Table 2: Pre-Chamber Data*

It should also be highlighted that the volume of the pre-chamber leads to a ratio Vol<sub>PC</sub>/Vol<sub>Clearance</sub> equal to 7.2%, a value that can be considered quite high compared to literature data, where usually values around 4-5% are adopted ([17], [9]).

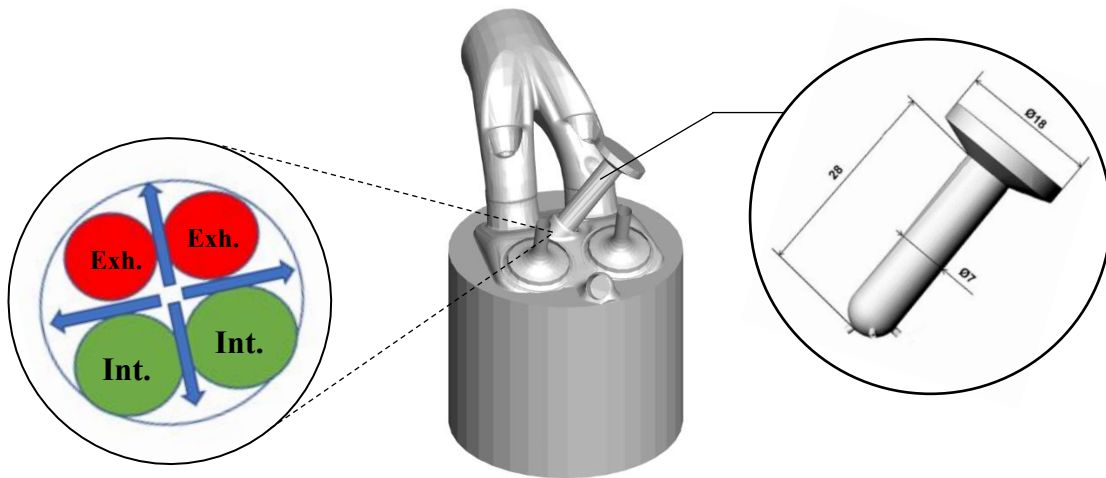


*Figure 7: Single-cylinder Engine Representation (without Intake Line), Detail of Pre-Chamber Dimensions (Right), Detail of Holes Orientation (Left)*

The experimental data, which were gathered at CNR – STEMS and provided alongside the engine CAD geometry, are coming from a total of 14 test cases, each consisting of a run of 400 cycles; test results coming from said experiments were processed and corrected in previous works ([18], [19]). The list of performed experiments is reported in Table 3, which also provides details on employed calibration parameters such as Spark Timing (ST) and Start of Injection (SOI), and engine performance parameters such as Brake Torque and Indicated Mean Effective Pressure (IMEP). Furthermore, the temperature data reported in Table 3 refer to coolant temperature at cylinder head exit ( $T_{Eng}$ ) and exhaust port temperature measured 10 cm and 45 cm from the exhaust valves ( $T_{Exh1}$  and  $T_{Exh2}$ ).

It is interesting to notice the choice in spark timing variation as a function of the dilution ratio for the engine rotational speed: the leaner mixture operations correspond to earlier spark timings. This strategy is adopted in an attempt to compensate the decrease in burning speed caused by the increase in mixture dilution. This fact highlights a potential advantage of an active TJI system: by decoupling main chamber and pre-chamber conditions in terms of mixture preparation (for example, by running the pre-chamber in stoichiometric conditions), it is possible to choose the spark timing without considering the main chamber  $\lambda$ .

| Test Nr. | Rot. Speed [rpm] | $\lambda$ [-] | ST [deg] | SOI [deg] | Torque [Nm] | IMEP [bar] | T <sub>Eng</sub> [K] | T <sub>Exh1</sub> [K] | T <sub>Exh2</sub> [K] |
|----------|------------------|---------------|----------|-----------|-------------|------------|----------------------|-----------------------|-----------------------|
| 1        | 2000             | 1             | -12      | -230      | 83          | 8.35       | 48                   | 490                   | 170                   |
| 2        | 2000             | 1             | -10      | -230      | 81          | 8.01       | 89                   | 501                   | 290                   |
| 3        | 2000             | 1.4           | -20      | -230      | 63          | 6.5        | 88                   | 440                   | 255                   |
| 4        | 3000             | 1             | -20      | -230      | 101         | 9.28       | 77                   | 612                   | 401                   |
| 5        | 3000             | 1             | -20      | -230      | 99          | 9.18       | 90                   | 630                   | 388                   |
| 6        | 3000             | 1.4           | -36      | -230      | 78          | 7.65       | 66                   | 558                   | 245                   |
| 7        | 3000             | 1.4           | -36      | -230      | 78          | 7.65       | 74                   | 560                   | 290                   |
| 8        | 3000             | 1.4           | -36      | -230      | 78          | 7.65       | 80                   | 570                   | 312                   |
| 9        | 4000             | 1             | -24      | -230      | 114         | 10.11      | 70                   | 684                   | 412                   |
| 10       | 4000             | 1             | -25      | -230      | 111         | 9.75       | 95                   | 689                   | 475                   |
| 11       | 4000             | 1             | -25      | -230      | 111         | 9.71       | 90                   | 687                   | 438                   |
| 12       | 4000             | 1.2           | -69      | -230      | 99          | 8.8        | 85                   | 644                   | 412                   |
| 13       | 4000             | 1.2           | -69      | -230      | 98          | 8.73       | 93                   | 646                   | 420                   |
| 14       | 5000             | 1             | -36      | -230      | 115         | 10.12      | 90                   | 750                   | 495                   |

Table 3: List of Performed Tests

The valve lift profile is reported in Figure 8, as well as valve opening and closure timings in Table 4. The valve lift profile shown include the effects of calibration parameters such as, for example, valve lash.

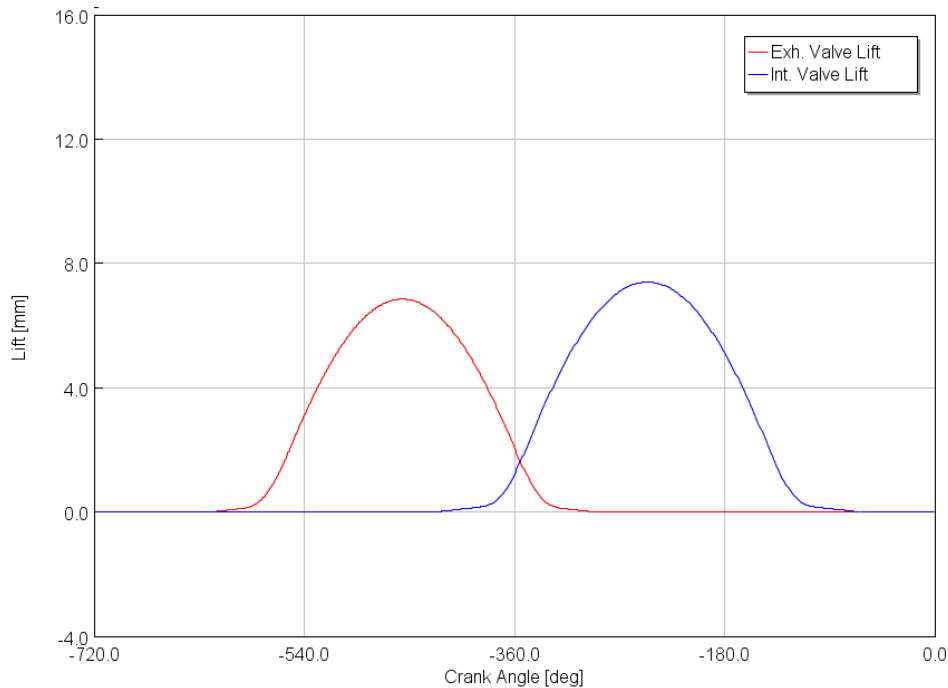


Figure 8: Valve Lift Profiles

| Valve Opening/Closure |                |
|-----------------------|----------------|
| EVO                   | -620 CAD aTDCf |
| EVC                   | -293 CAD aTDCf |
| IVO                   | -418 CAD aTDCf |
| IVC                   | -64 CAD aTDCf  |

Table 4: Valve Openings and Closures

## 2.1.2 Workflow

Before analyzing the tools and models used, it is useful to describe the methodology which was adopted during the study. In particular, throughout this work, a synergy between 1D and 3D instruments was exploited, in order to supply the required boundary conditions as inputs to 3D-CFD models and properly elaborate the 3D-CFD outputs using the same underlying assumptions adopted for experimental data.

First of all, the experimental data needed validation and, eventually, adjustment to obtain the necessary boundary conditions for the 3D-CFD model. To do so, a 1D-TPA model, previously built ([18], [19]), was employed. The Three-Pressure Analysis (TPA) approach uses experimental pressure traces for intake, exhaust and cylinder as input in order to obtain the corresponding Heat Release Rate. Moreover, due to descriptive nature of the model, the verified pressure and temperature profiles for intake and exhaust ports can be obtained and used as boundary conditions for the -CFD model. The employed 3D-CFD model, instead, can resolve the chemical reactions and released energy during the combustion process with a predictive approach. The pressure trace resulting from 3D-CFD is then fed to another 1D model in order to perform a so-called Cylinder Pressure Only Analysis, CPOA. Similarly to the TPA, the CPOA approach obtains the cycle Heat Release Rate from the pressure trace, in this case obtained from the 3D-CFD model, using the same underlying assumption adopted for the analysis of experimental data. The HRR from the 3D-CFD model can thus be compared with the experimental one since it is obtained from the same procedure

A scheme summarizing the workflow adopted in this work is represented in Figure 9.

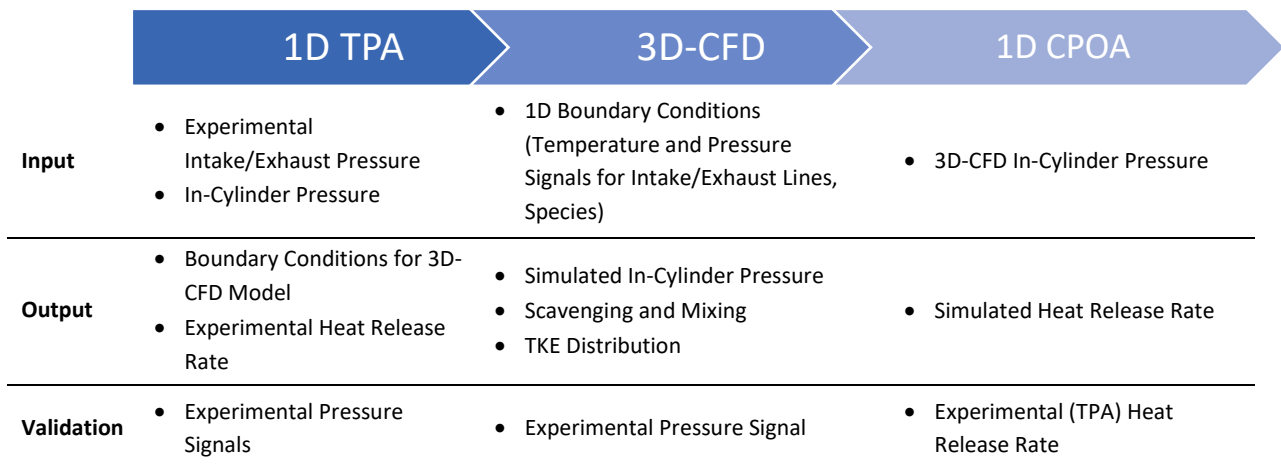


Figure 9: 1D-3D Synergy and Workflow

## 2.1.3 1-D Models

### 2.1.3.1 TPA

The software used to build and run both the TPA and CPOA models is GT-SUITE. The GT-SUITE model employed in the analysis is represented in the Appendix.

The TPA approach, as hinted earlier, uses a physically based model to simulate the engine cycle and Heat Release Rate. In particular, experimental data for intake, exhaust and in-cylinder pressure, in addition to geometrical data for the intake and exhaust lines are required. Proper calibration of this model on the geometrical parameters of the engine was performed in previous works ([18], [19]). A brief description of the model will follow.

#### 2.1.3.1.1 Intake Line

The intake line models air admission in the runner but also fuel injection, air-fuel mixing and mixture admission in the cylinder. The first element is the “intake”, which represents the intake environment and upon which the experimental intake pressure trace is applied. The “IntRunner” element models the intake runner, the portion of the intake line from the intake pressure sensor to the intake ports. This part is also connected to model of the fuel injector, “InjAFSeqConn”, which specifies the injection flow rate, the used fuel and the dilution ratio. The intake ports were obtained from the CAD file describing the engine geometry with the GEM3D tool. The outcome of this tool results in a flowsplit element, “yplit”, followed by two piperound elements, “Int\_port”. The final elements of the intake line are the valves. The valve element, “Int\_valve”, contains all the parameters necessary to the description of the gas exchange process: the nominal valve profile (used as an input); the valve lash, the gap between cam and valve stem (it is worth highlighting that these parameters combined will give the real valve lift profile used in the engine and 3D-CFD model); the reference valve diameter and discharge coefficients (forward and reverse), used to characterize the flow losses across the valves from intake to cylinder (forward discharge coefficient) and viceversa (reverse discharge coefficient).

As a final note, the intake “return signal” (in the upper part of the intake line) is described: this an artificial method to avoid pressure waves (for example, due to valve closure) to alter the intake pressure trace. This alteration would, in turns, be incorrect, as the signal used is experimental and thus already considers such effects.

#### 2.1.3.1.2 Cylinder

The core of the TPA model is the cylinder part, made up of the pre-chamber, main chamber and crank mechanism. It is important to highlight that the pre-chamber part, “Prechamber”, is not really modelling the combustion event inside the pre-chamber, but only the geometrical features of it. This is a consequence of the lack of experimental data in terms of pre-chamber pressure trace, the absence of which makes the simulation of a combustion event (with a calculated HRR) impossible. Pre-chamber and cylinder are connected by the “Pre\_con” object, which specifies the connecting holes geometry (length and diameter) and discharge coefficients.

The cylinder part, “Main-chamber”, is set to a TPA Pressure Analysis Mode and requires as input the in-cylinder experimental pressure trace, with the specification of the spark timing. This pressure analysis mode will calculate, starting from the experimental pressure and overall engine description,

the required fuel burning and HRR to obtain such experimental result. The cylinder model also requires the initial conditions description, as well as heat transfer properties (such as the heat transfer model and parameters used in heat transfer calculations like head/bore area ratio and piston/bore area ratio). Moreover, wall temperatures must be defined; in particular, due to the lack of experimental data, typical SI engine values were assumed from previous experiences:

- Cylinder Head Temperature: 550 K
- Piston Temperature: 500 K
- Cylinder Temperature: 400 K

Lastly, the engine cranktrain object, “Engine”, is used to describe the geometrical features of the engine (stroke, bore, con-rod length, compression ratio) as well as operational parameters such as engine rotational speed and Friction Mean Effective Pressure FMEP.

#### 2.1.3.1.3 Exhaust Line

The exhaust line description is analogous to the one of the intake. Exhaust valves, ports and runner represent the same feature of their intake counterparts. A model to account for the presence of a TWC in the exhaust line is introduced between a first and a second Exhaust Runner part. The TWC length was the only measurement known for such component, thus the remaining features were the outcome of an intense calibration action performed in previous studies.

The last element of the intake line is the end environment, “Exhaust”. This element, just like the intake environment for the intake line, uses the experimental exhaust pressure as input. In this case, the exhaust pressure was unknown, and thus was set equal to a constant value of 1 bar.

#### 2.1.4.2 CPOA

Differently from TPA, the CPOA approach doesn’t require intake and exhaust pressure signals; thus, the resulting 1D model is much easier, as it doesn’t need to describe intake and exhaust lines. The only elements of this model are the cylinder, “Main-chamber”, and engine cranktrain, “Engine” (Figure 10). The only needed input is the in-cylinder pressure and initial in-cylinder fluid characteristics at Start of Combustion. The initial conditions are needed to describe cylinder state at ST in terms of residual percentage in the main chamber, intake air mass (via the value of volumetric efficiency), intake fuel mass and fuel amount.

As in the TPA, the engine cranktrain object is used to describe the geometrical and operational parameters of the engine (stroke, bore, engine speed, FMEP etc.).

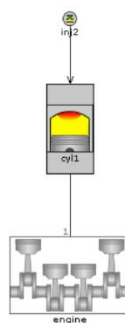


Figure 10: CPOA Model

## 2.1.4 3D-CFD MODEL

The software used for the 3D-CFD model is CONVERGE CFD. It allows solving the fluid flow governing equations and, additionally, account for chemical reactions and hence combustion development using dedicated models. In addition, it includes algorithms for mesh refinements and motion of boundaries.

In principle, the aim of a 3D-CFD code is to find a numerical solution to a set of equations describing the fluid motion. These governing equations come from the conservation principles applied to a control volume of fluid. The logic used in the subsequent description follows the one used in ([20]), which is the reference for any further detail.

Generally, for a conserved intensive quantity  $\phi$ , the following expression can be written:

$$\frac{d}{dt} \int_{V_{CM}} \rho \phi \, dV = \frac{d}{dt} \int_{V_{CV}} \rho \phi \, dV + \int_{S_{CV}} \rho \phi (\mathbf{v} - \mathbf{v}_s) \cdot \mathbf{n} \, dS$$

which states that the rate of change of the property in the system (also called Control Mass, CM) is given by the rate of change of the property in the Control Volume (CV) and the net flux of it through the CV boundary  $S_{CV}$ , which is defined as *convective* contribution. All of the conservation equations can be derived by the previous equation by considering the proper  $\phi$ .

The list of said equations will follow (note: bold variables represent a vectorial quantity):

- Mass Conservation: also known as “Continuity Equation”, follows from the control volume equation by setting  $\phi = 1$ .

$$\frac{\partial}{\partial t} \int_V \rho \, dV + \int_S \rho \mathbf{v} \cdot \mathbf{n} \, dS = 0$$

- Momentum Conservation: there are several ways to derive the momentum conservation equation. For the sake of brevity, the general expression of momentum conservation can be obtained considering the control volume equation and set  $\phi = \mathbf{v}$ .

$$\frac{\partial}{\partial t} \int_V \rho \mathbf{v} \, dV + \int_S \rho \mathbf{v} \mathbf{v} \cdot \mathbf{n} \, dS = \sum \mathbf{f}$$

where the term on the right hand side consider all the forces acting on the CV. In particular, surface forces (e.g.: pressure, normal and shear stresses) and body forces (e.g.: gravity, centrifugal forces) must be considered. It is important to notice that the previous expression is general; for Newtonian fluids, the momentum conservation equation can be written expressing the surface forces with the stress tensor  $\mathbf{T}$ :

$$\frac{\partial}{\partial t} \int_V \rho \mathbf{v} \, dV + \int_S \rho \mathbf{v} \mathbf{v} \cdot \mathbf{n} \, dS = \int_S \mathbf{T} \cdot \mathbf{n} \, dS + \int_V \rho \mathbf{b} \, dV$$

- Conservation of Scalar Quantities: similarly to the momentum conservation, the conservation of the scalar  $\phi$  be expressed as

$$\frac{\partial}{\partial t} \int_V \rho \phi \, dV + \int_S \rho \phi \mathbf{v} \cdot \mathbf{n} \, dS = \int_S \Gamma \nabla \phi \cdot \mathbf{n} \, dS + \int_V q_\phi \, dV$$

where the terms on the right represent the scalar transport mechanism that are not convection (such as diffusion, defined by Fick's law for mass diffusion, with  $\Gamma$  indicating the diffusivity) and any sources/sinks.

The geometry used in the 3D-CFD model comes from a CAD file supplied together with the experimental data from CNR – STEMS. After a geometry manipulation in which surface defects were repaired and components were correctly displaced, accounting for relative positions during the engine cycle, boundaries are assigned to each component, in order to define the computational domain. As far as geometry and mesh definition are concerned, the main aspects involved in the case setup will be summarized in the following section.

#### 2.1.4.1 Mesh

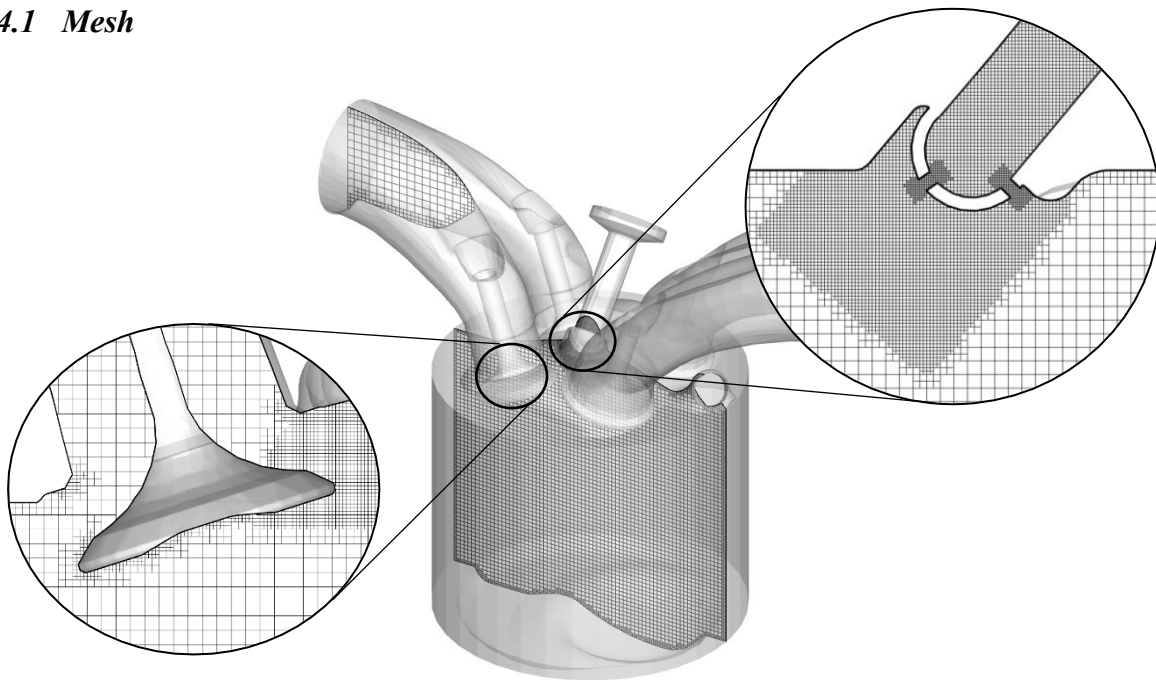


*Figure 11: Embedded Grid, Detail on PC Refinement (Right), Detail on Exhaust Valve and Valve Seat Refinement (Left)*

One of the most important aspects involved in numerical modelling and mesh definition is, most likely, to find the right balance between model accuracy, which is strictly connected to mesh resolution, and computational time. In this case, the utilized software allows to create a base mesh and further refinements based on user definition in presumed sensitive areas and flow conditions.

The “base grid size” is shared by the whole computational grid, which is defined by a “cartesian cut-cell” approach. In this model, a base grid size of 2 mm was chosen.

The “fixed embedding” control allows to define mesh refinements based on location and time. This is an especially useful feature when the geometry allows the prediction of the most critical locations defining the phenomenological outcome of the simulation. A clarifying example is the refinement placed at the pre-chamber holes, which are a fundamental aspect of TJI combustion, as well as being a relatively small component of the whole system. Table 5 lists the main fixed embedding refinements employed in the presented model, while Figure 11 shows the computational grid obtained at simulation start.

| Boundary                     | Embedding Scale<br>[-] | Grid Size<br>[mm] |
|------------------------------|------------------------|-------------------|
| Cylinder                     | 1                      | 1                 |
| Pre-Chamber Holes            | 4                      | 0.125             |
| Spark Plug                   | 4                      | 0.125             |
| Intake Valve and Valve Seat  | 3                      | 0.25              |
| Exhaust Valve and Valve Seat | 3                      | 0.25              |
| Intake Port                  | 1                      | 1                 |
| Exhaust Port                 | 1                      | 1                 |
| Cylinder Head                | 2                      | 0.5               |
| Liner                        | 2                      | 0.5               |
| Piston                       | 2                      | 0.5               |
| Pre-Chamber                  | 3                      | 0.25              |

*Table 5: Fixed Embedding Scales and Resulting Grid Size*

In addition to user-defined “fixed embedding” refinements, the “Adaptive Mesh Refinement”, AMR, algorithm allows to automatically increase and decrease the grid resolution based on curvatures (second derivatives) in field variables ( [21]). AMR can be permanent or time-dependent, and it can be used on a region-by-region basis. The field variables used to activate the AMR in this model are fluid velocity and fluid temperature. Figure 12 shows an example of mesh adaptation as a consequence of AMR during the combustion process,

| Region       | Temperature Sub-Grid<br>Criterion<br>[K] | Velocity Sub-Grid<br>Criterion<br>[m/s] | Max Embedding<br>Scale<br>[-] |
|--------------|--|---|-------------------------------|
| Cylinder     | 2.5                                      | 1                                       | 3                             |
| Intake Sys.  | -  | 1                                       | 2                             |
| Pre-Chamber  | 2.5                                      | 1                                       | 4                             |
| Exhaust Sys. | -  | 1                                       | 2                             |

*Table 6: AMR Settings*

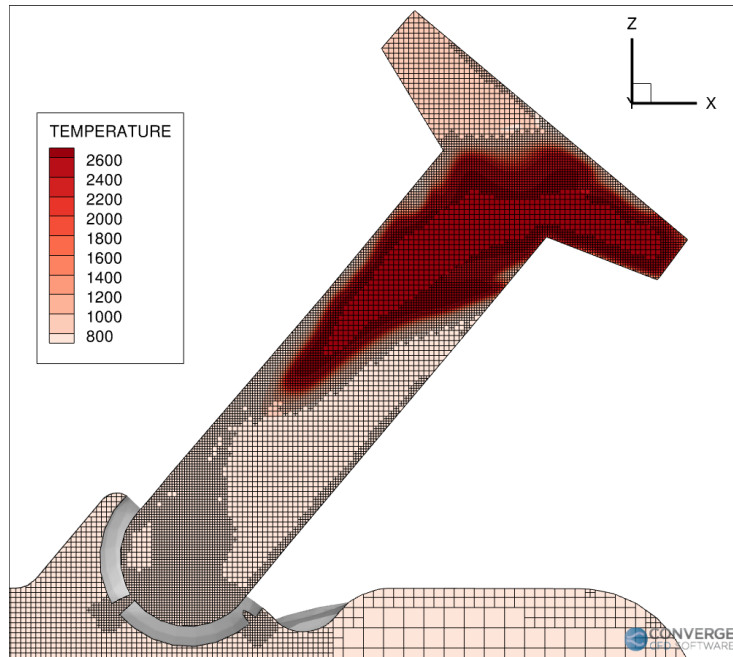


Figure 12: Example of AMR during Pre-Chamber Combustion

Finally, Table 6 lists the utilized AMR criteria on a region-by- region base. It is worth reminding that the embedding level defines the grid dimension as described by equation (1) [21]:

$$embed \ cell \ size = dx\_base / 2^{embedding \ scale} \quad (1)$$

#### 2.1.4.2 Combustion modelling

Combustion modelling in TJI systems is particularly complex, due to the many aspects involved in it. The SAGE chemical solver was chosen to overcome this issue, as it can reliably simulate combustion phenomena, both in premixed and non-premixed processes.

SAGE uses a data file for elementary reactions, which are expressed in the format of Arrhenius Law, in order to account for chemistry chain-reaction evolution on a cell-by-cell basis within the 3D-CFD computational domain. The reaction mechanism proposed by the Argonne National Laboratory ([22]) was adopted. By solving the chemical kinetics in each cell at each time step, the SAGE solver is able to return the change in species mass fraction, so it provides inputs concerning sink/sources for the species mass conservation equation. Moreover, yielding an output in terms of energy released by the chemical reaction it enables the solution of the energy conservation equation and provides useful information concerning where reactions are happening within the simulation domain, what is the local energy release and how combustion is developing.

The need of a chemical mechanism requires, in principle, the definition of the species involved in such reaction, which means, in other words, that it is necessary to define in the virtual environment the chemical species representing the fuel employed in the real engine. To do so, a surrogate proposed by Morgan ([23]), obtained starting from the real values of RON and MON, was chosen, following the widely adopted approximation of representing conventional gasoline by means of a mixture of

Toluene, N-Heptane, and Isooctane. The fuel composition, expressed on a mass fraction base, of the surrogate is reported in Table 7.

| $C_7H_8$ [%] | $C_7H_{16}$ [%] | $C_8H_{18}$ [%] |
|--------------|-----------------|-----------------|
| 68.95        | 23.15           | 7.90            |

Table 7: Fuel Surrogate Composition

### 2.1.4.3 Turbulence Modelling

Turbulence modelling is a key aspect of most 3D-CFD simulations, especially in internal combustion engines equipped with TJI systems given the influence of turbulence development on combustion evolution. In general, the Navier-Stokes equation can be addressed by following two different approaches: direct simulation and turbulence modelling.

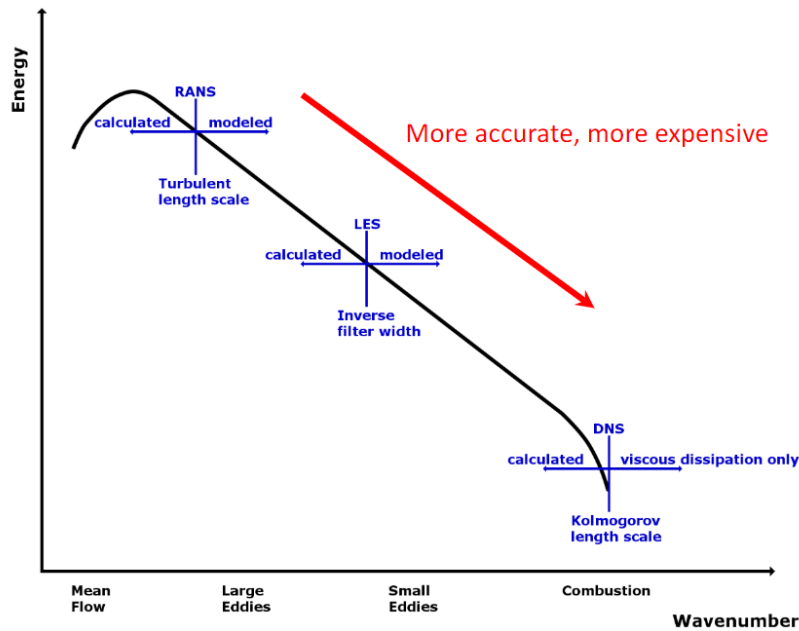


Figure 13: CFD Turbulence Solution Approaches ([21])

In a Direct Numerical Simulation approach, no turbulence is modelled; instead, all of the turbulent scales are resolved. In this case, the price for high results accuracy is the practically unacceptable computational time for engineering relevant phenomena happening, for example, in internal combustion engines.

The alternative to this approach is turbulence modelling, in which a turbulence model is used to close the computational problem ([21]). In particular, in this work a RANS approach is adopted, in which all of the turbulent scales are modelled. The RANS approach aims at solving a time-averaged version of the Navier-Stokes equations, thus giving a representation of mean flow conditions. At the same, the presence of an unsteady term, coming from fluctuations in the flow conditions, makes it necessary for this approach to introduce a further model to reach a closure to problem. This is realized by introducing the turbulent viscosity, a quantity modelled based on two parameters: turbulent kinetic

energy and turbulence dissipation rate. In this work, the k- $\epsilon$  model was used among the RANS models. In this work, the k- $\epsilon$  model was used among the RANS models.

In order to reduce the computational effort related to turbulence description, the flow behavior near the wall was treated by means of the “law of the wall” approach, in which there is no resolution of the viscous sub-layer but only an estimate of the wall shear stress based on empirical relations.

Wall heat transfer was modelled with the Han & Reitz model ([24])

## 2.2 Flame/Hole Interaction Model

### 2.2.1 Literature Research

The applied methodology revolves around the work carried out in [25], where simplified experiments were performed to better characterize the jet ignition phenomenon. Experimental and modelling results allowed to advance a proposal defining the outcome of flame/wall interaction inside a pre-chamber hole based on two parameters: a combustion related parameter, the Laminar Flame Thickness (LFT), and a geometrical parameter, the pre-chamber hole diameter (d). Said proposal can be summarized as follows:

$$\frac{2 * LFT}{d} < 1 \quad \text{Flame Passing}$$

$$\frac{2 * LFT}{d} > 1 \quad \text{Flame Extinction}$$

The correlation between LFT and hole diameter will be the core of the investigation carried out on the flame/hole interaction.

Similar studies, although with different initial gas thermodynamic conditions, are extensively carried out in [26]. Moreover, the availability of experimental evidence and experimental setup data made it possible to build a numerical model to try and replicate the results in a 3D-CFD environment. In particular, two different test cases representing two different outcomes, jet ignition and flame ignition, were performed. The main features of said cases are summarized in Table 8.

| Test No. | Orifice Diameter | T   | P     | Spark Location | $\Phi_{pre}$ | $\Phi_{main}$ | Ignition Mechanism | Ignition Delay |
|----------|------------------|-----|-------|----------------|--------------|---------------|--------------------|----------------|
| [-]      | [mm]             | [K] | [MPa] | [-]            | [-]          | [-]           | [-]                | [ms]           |
| 5        | 2.5              | 500 | 0.1   | Top            | 1.0          | 1.0           | Jet Ignition       | 18.32          |
| 10       | 4.5              | 500 | 0.4   | Top            | 1.0          | 1.0           | Flame Ignition     | 2.27           |

Table 8: Test Cases (extracted from [26])

The following sections will describe the main features of 1D and 3D-CFD tools used.

## 2.2.2 Converge Chemistry Tool

The tool used to extract values of Laminar Flame Thickness in given conditions was the Converge Chemistry Tool, used to simulate a freely propagating laminar flame speed. As methane was simulated, a fuel surrogate was necessary to be defined, alongside its reaction mechanism and transport data. The surrogate fuel was the same as the one used in [27], with mass fraction composition found in Table 9; the chosen reaction mechanism for methane was the GRI3.0 ([28]).

| CH <sub>4</sub> [%] | C <sub>2</sub> H <sub>6</sub> [%] | C <sub>3</sub> H <sub>8</sub> [%] |
|---------------------|-----------------------------------|-----------------------------------|
| 93.0                | 5.2                               | 1.8                               |

Table 9: Methane Fuel Surrogate

A general description of the setup used in the CONVERGE Chemistry Tool can be found in Table 10.

|                          |       |                             |
|--------------------------|-------|-----------------------------|
| Comb. Temperature Cutoff | [K]   | 10% of Unburned Temperature |
| Unburned Temperature     | [K]   | 500                         |
| Unburned Pressure        | [MPa] | 0.1 – 0.4                   |
| Initial Velocity         | [m/s] | 0.3 (Default)               |
| Equivalence Ratio        | [-]   | 1.0                         |
| EGR Ratio                | [.]   | 0.0                         |

Table 10: General Setup for Converge Chemistry Tool (One-D Premixed Laminar Flame)

## 2.2.3 3D-CFD Model

### 2.2.3.1 Geometry

The real experimental setup is represented in Figure 14 alongside a graphical representation of it. [26] provides data for the experimental setup, although some dimensions were missing and had to be assumed or extrapolated from the provided evidence (for example, only the pre-chamber volume was given).

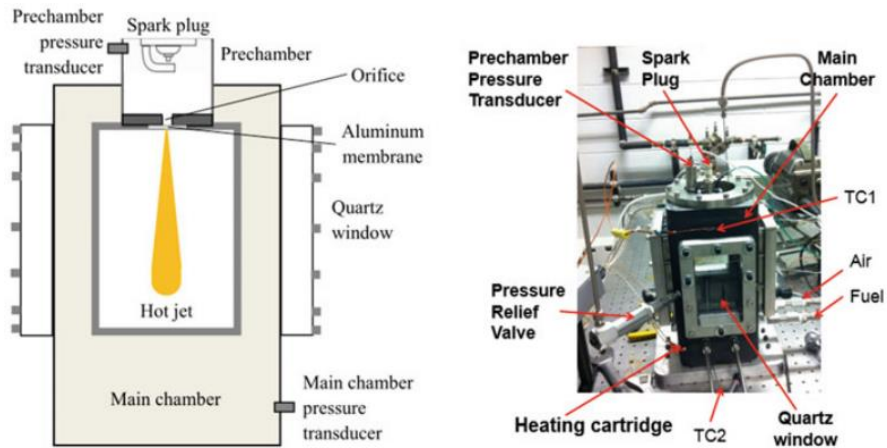


Figure 14: Experimental Setup used in [26]

The numerical model geometry was built having in mind a compromise between real representation and computational cost. First and foremost, being the goal to capture the phenomena happening inside the pre-chamber hole, this last feature was kept with the same geometry as its real-life counterpart. The dimension of the hole was varied between 2.5 mm and 4.5 mm, depending on the simulated test case.

The pre-chamber was modelled as having a box shape with real life dimensions. Instead, the main chamber, again box-shaped, was designed to have a height decreased of two thirds. The reason for this was to save computational time by cutting the peripheral part of the main chamber, where only established flame propagation occurs. Moreover, the base of the main chamber has a side with a dimension equal to four times the hole dimension. All of the boundaries limiting the computational domain are of the “Wall” type. The geometry used is finally represented in Figure 15.

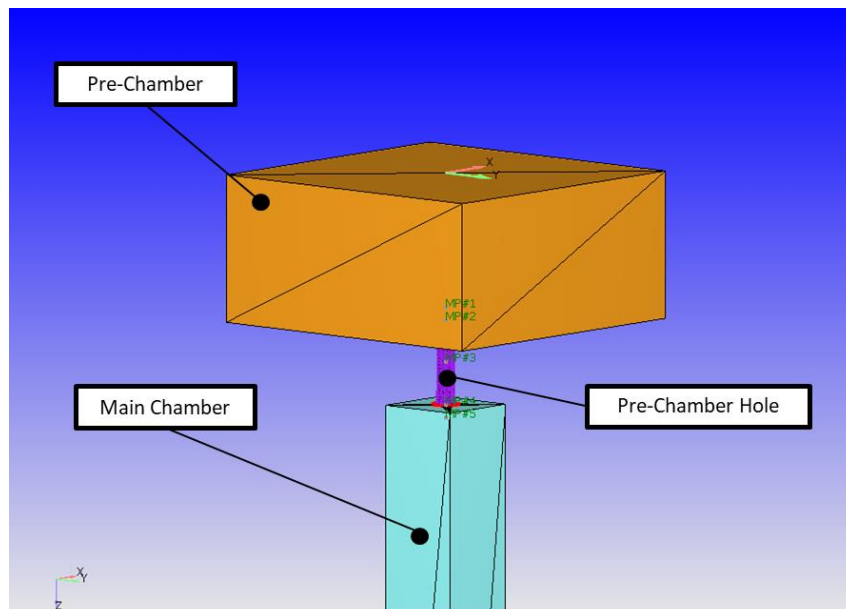


Figure 15: Flame/Hole Interaction Model

As a last note, it is underlined how the geometry triangles forming the model were designed and carefully refined to allow a regular extrusion of near-wall mesh.

### 2.2.3.2 Mesh

In this framework, mesh definition was especially important for the correct representation of the experiments. With the goal of investigating the flame-hole interaction, where relevant phenomena are characterized by spatial scales with dimensions of the same order of magnitude of the thermal boundary layer, near-wall treatment requirements switch from law of the wall modelling to direct solution of near wall turbulence using a refined mesh. With this last approach, the flow up to the viscous sublayer is resolved, at the expense of a very small  $y^+$  (i.e.: a parameter "relating the cell size adjacent to the wall to the physical location in the boundary layer based on the local velocity" [21]) and higher computational cost.

To do so, a customized mesh was set near the wall of the pre-chamber hole by means of the “Inlaid Meshing” tool of Converge Studio. With such tool, geometry triangles are extruded to form box-shaped flow-through boundaries, which will ultimately define portions of mesh in the final computational grid. In particular, fifteen layers with an expansion ratio of 1.01 were defined inside the hole and in the portion of pre-chamber near the hole entrance. A specific check of simulation results confirmed the achievement of requirements concerning  $y^+$  for the correct solution of near wall velocity profile, with  $y^+$  values ranging from 0.9 to 1.5.

One of the most critical aspects associated with inlaid meshing is the proper matching between inlaid mesh and the base, cartesian grid, which could create numerical problems in terms of stability and truthfulness of the solution. To do so, a preliminary mesh quality check was performed, based on the quality metrics expressed in the Converge Studio Manual ([21]) until a satisfactory mesh quality was obtained. Figure 16 shows a picture of the final computational grid alongside a contour plot showing cell values for non-orthogonality. As noticeable, non-orthogonality was proved to be the most critical aspect in defining the mesh. Nevertheless, despite the values obtained with further and further refinements, this mesh was accepted to be satisfactory, as the high non-orthogonality was considered an “unavoidable” error coming from the matching of a radially directed grid and a cartesian one.

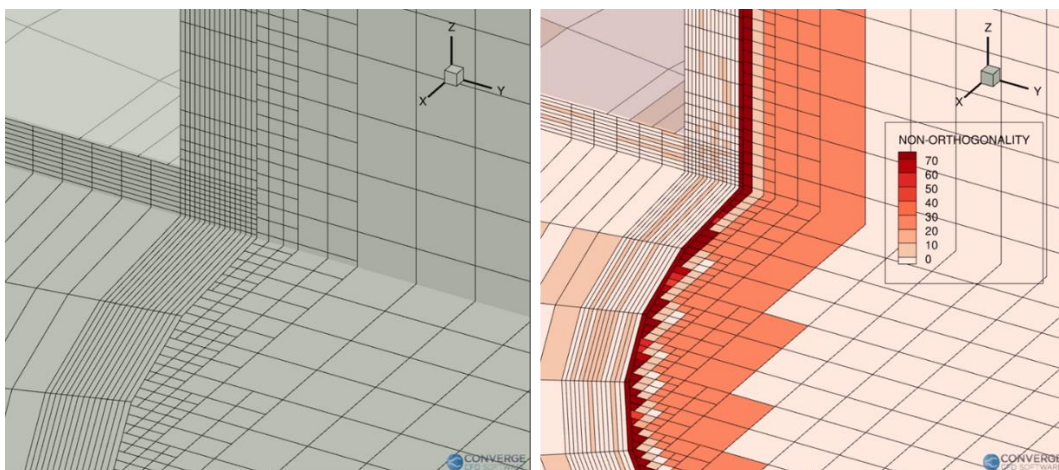


Figure 16: Starting Mesh (left) and Non-Orthogonality (right)

To conclude, the settings associated to the cartesian grid, which has a base size of 2 mm, are listed: Table 11 shows the details of the employed fixed embeddings and Table 12 shows the AMR settings used in hole and pre-chamber regions.

| Boundary                           | Embedding Scale<br>[-] | Grid Size<br>[mm] |
|------------------------------------|------------------------|-------------------|
| Spark Location                     | 3                      | 0.25              |
| Inlaid Mesh Exterior (Hole)        | 6                      | 0.03125           |
| Inlaid Mesh Exterior (Pre-Chamber) | 4                      | 0.125             |

*Table 11: Flame/Hole Interaction Model Fixed Embeddings*

| Region            | Temperature<br>Sub-Grid<br>Criterion<br>[K] | Velocity Sub-<br>Grid Criterion<br>[m/s] | Inlaid Neighbor<br>Criterion<br>[-] | Max<br>Embedding<br>Scale<br>[-] |
|-------------------|---|--|-------------------------------------|----------------------------------|
| Hole, Pre-Chamber | 2.5   | 1  | 1                                   | 3                                |

*Table 12: Flame/Hole Interaction Model AMR Settings*

### 2.2.3.3 Other Settings

The settings for combustion and turbulence modelling were kept equal to those adopted in in-cylinder modelling.

Combustion modelling settings were kept the same, changing only the fuel surrogate and reaction mechanism by adopting the same setup described in the CONVERGE Chemistry tool description.

The same can be said for turbulence modelling, with the only exception to the near-wall treatment setting changed to “enhanced”, to allow viscous sublayer solution.

Source/Sink modelling for start of combustion was taken from the engine model and adapted to time domain.

# Chapter 3

## Results

### 3.1 4000 rpm

#### 3.1.1 4000 rpm x $\lambda=1$

The first case analyzed, and as such will be considered as the “baseline case”, is at stoichiometric conditions ( $\lambda=1$ ) and 4000 rpm. First, an overview of the pre-chamber scavenging process will be presented, as it sets the blueprint for the entire pre-chamber combustion evolution. Subsequently, the afore-mentioned pre-chamber combustion will be investigated, and it will be followed by the main chamber combustion event. This first analysis will provide a glimpse on the general aspects of TJI combustion.

##### 3.1.1.1 Cold Flow Analysis

First and foremost, a consistency check must be carried out to verify that the 3D-CFD simulation cold flow results are in agreement with 1D results derived from experimental data. To do so, exhaust and intake mass flow rates for the 3D-CFD simulation and the 1D-TPA model are plotted in Figure 17 and compared. For a more comprehensive illustration, the intake and exhaust valves lifts are also plotted.

The 3D-CFD simulation seems to sufficiently represent the gas exchange process in the cylinder, with imperfections only around local peaks of mass flow rate. To address how important these deviations might be, the intake mass quantity present in the cylinder at IVC is analyzed (Figure 18). It can be concluded that the deviations are balancing each other off, giving a negligible difference in the amount of intake charge trapped in the cylinder as predicted by 1D and 3D-CFD codes (deviation  $\approx -1.6\%$ ). This is an important check, that confirm the truthfulness of the 3D-CFD simulation.

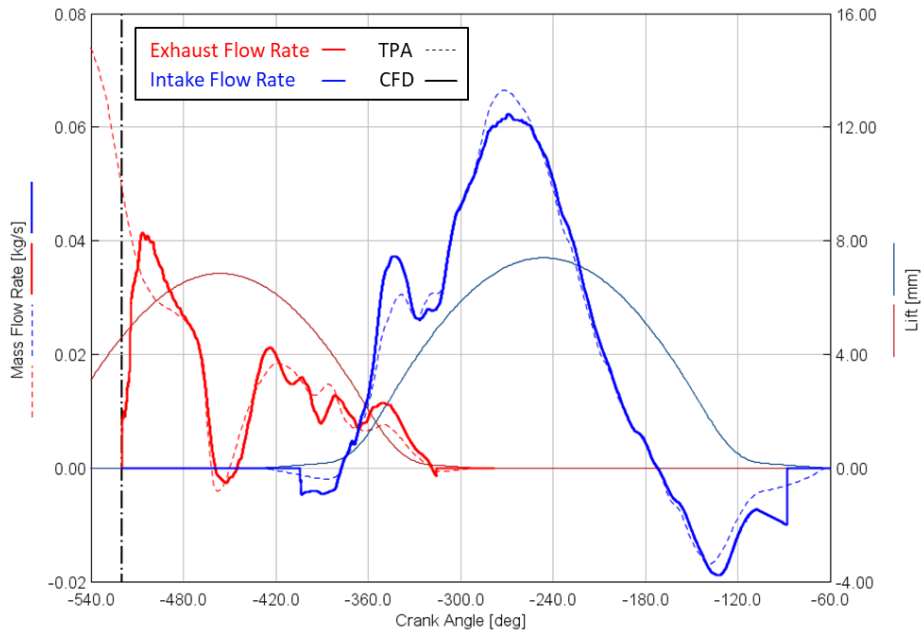


Figure 17: 4000 rpm  $\times \lambda=1$  – Gas Exchange Process

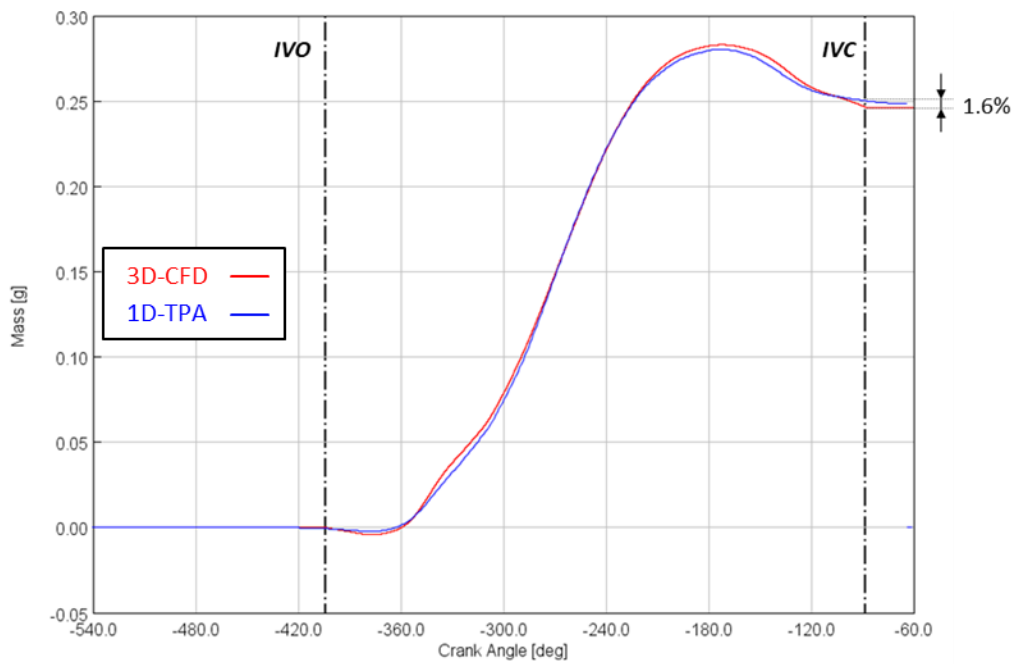


Figure 18: 4000 rpm  $\times \lambda=1$  – Intake Mass Comparison (TPA vs 3D-CFD)

The analysis of cold flow results coming from 3D-CFD and 1D-TPA models was carried out for all engine operating points, and provided results similar to those reported in this section, therefore they are not reported in the rest of the text for the sake of brevity.

### 3.1.1.2 Pressure & HRR Results

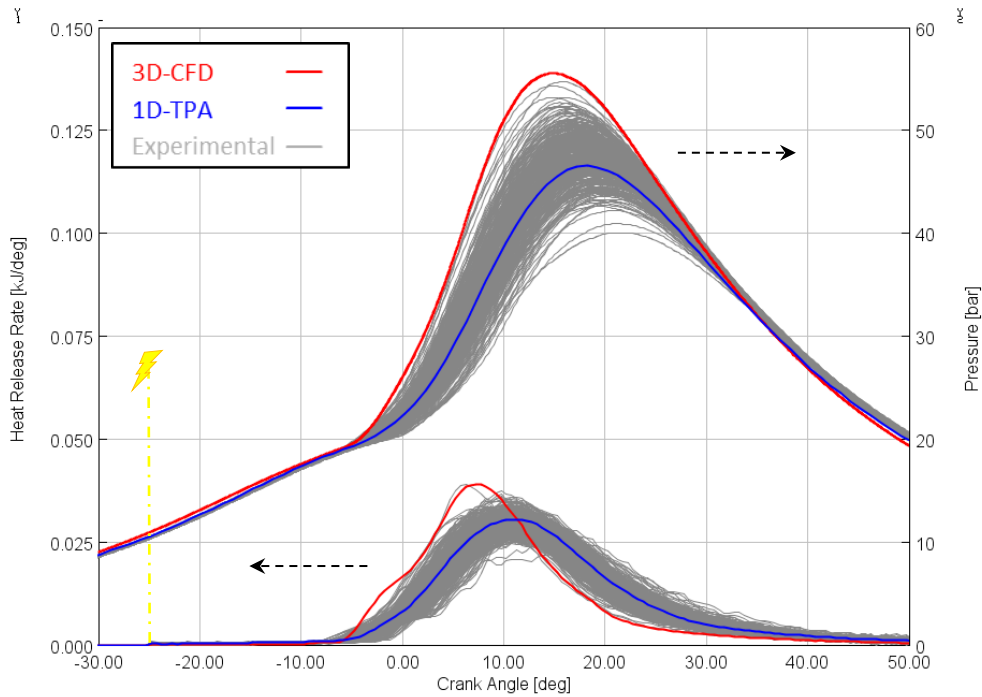


Figure 19: 4000 rpm  $\times \lambda=1$  - Pressure and HRR Profiles

Figure 19 shows the pressure and Heat Release Rate results of the 3D-CFD simulation (in red) alongside the experimental in-cylinder pressure data (in grey), representing the 400 cycles performed during the experiments, and TPA results coming from the average experimental cycle (in blue).

Compared with experimental results, the 3D-CFD model appears to be representative of a fast-burning cycle, falling just outside the experimental interval. Coherently, the Heat Release Rate trace shows signs of an intense combustion process inside the main chamber, with a higher peak with respect to the experimental average. Only MC combustion timing seems to be correctly maintained, as both HRR profiles seem to change slope around the same Crank Angle (roughly at -5 Crank Angle Degrees, CAD).

The faster combustion process described by the 3D-CFD solution is confirmed by the traces of Mass Fraction Burned (MFB) of fuel inside the cylinder, as per Figure 20 and Table 13, highlighting a difference in burn duration of about 4 CAD.

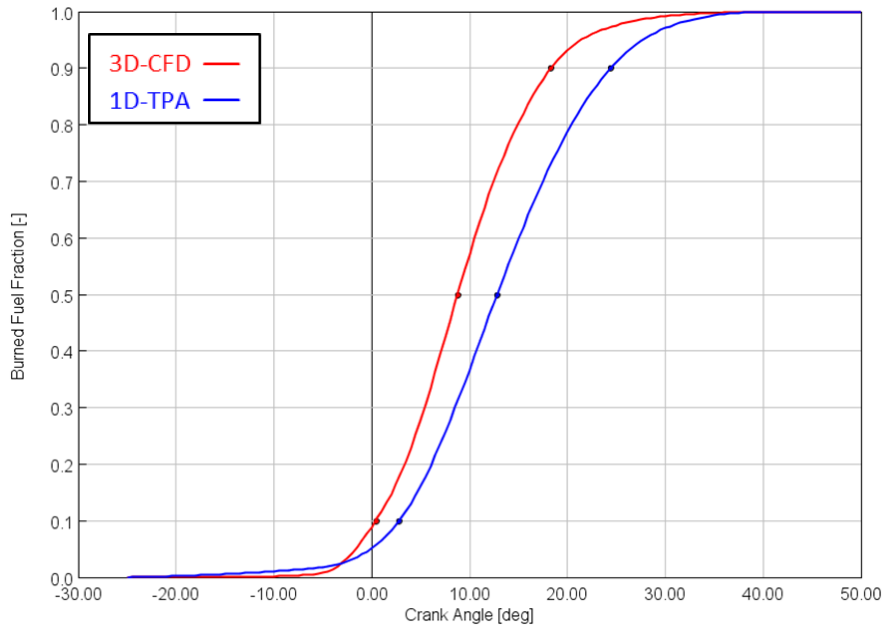


Figure 20: 4000 rpm x  $\lambda=1$  – Mass Fraction Burned

| Model  | MFB10<br>[CAD] | MFB50<br>[CAD] | MFB90<br>[CAD] | Burn Duration10-90<br>[CAD] |
|--------|----------------|----------------|----------------|-----------------------------|
| 1D-TPA | 2.8            | 12.8           | 24.4           | 21.6                        |
| 3D-CFD | 0.4            | 8.7            | 18.3           | 17.9                        |

Table 13: 4000 rpm x  $\lambda=1$  – Burn Duration

The following analysis will explain the main features involved in the engine operation, starting from pre-chamber conditions at Spark Timing (ST) up to the characteristics of the main combustion event.

### 3.1.1.1 Pre-Chamber Scavenging

As hinted in previous sections, pre-chamber scavenging is a key aspect of TJI systems, as it dictates the quantity and distribution of fresh charge to be burned inside the PC. This fact is even more critical in passive operation systems, as the present one. Scavenging analysis was performed both by means of the “pre-chamber” passive, a chemically-inert tracer representing the amount of residuals fraction left in the pre-chamber coming from the previous cycle, and the masses of residuals and fresh charge inside the PC.

It can be anticipated that the pre-chamber scavenging process is heavily affected by the pre-chamber geometry itself; for such reason, many similarities will be found between all the different cases investigated in this work.

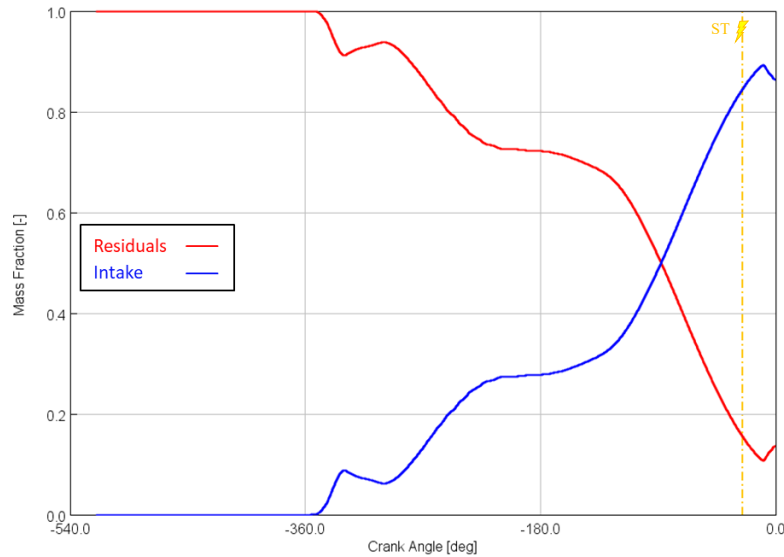


Figure 21: 4000 rpm x  $\lambda=1$  - Residuals and Intake Charge Mass Fractions inside PC

First, Figure 21 illustrates the levels of residual and intake charge mass fractions within the PC. The scavenging process begins at Intake Valve Opening with a portion of the intake charge ending in the pre-chamber as it is dragged into the cylinder. Nevertheless, the biggest contribution to pre-chamber “washing” is achieved during the compression stroke by the fresh mass pushed inside the pre-chamber. This is highlighted even more by Figure 22, which shows the masses of residuals and intake charge inside the pre-chamber.

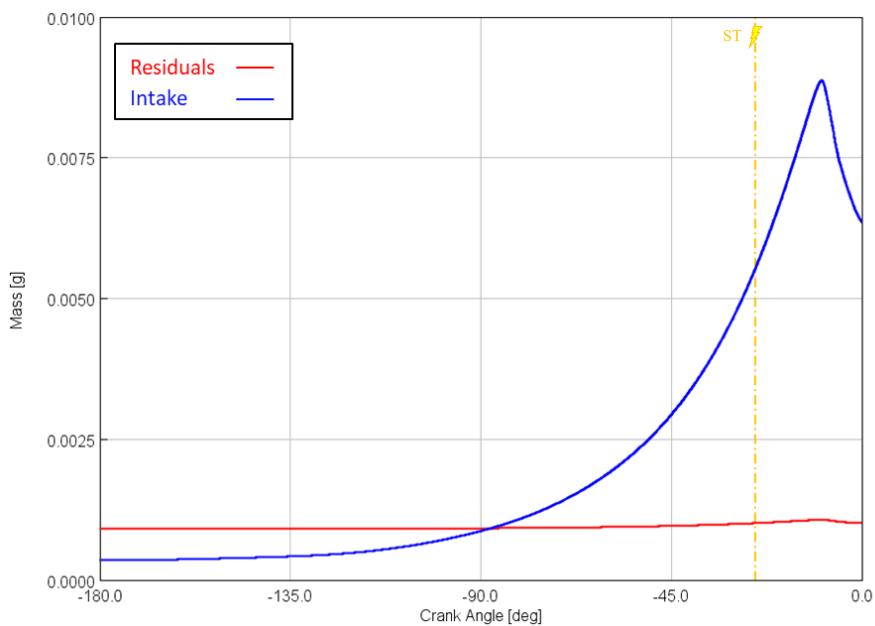


Figure 22: 4000 rpm x  $\lambda=1$  - Residuals and Intake Mass inside PC

The two trends lead to the conclusion that, while residuals mass remains more or less constant after IVC, the mass of fresh species grows larger and larger during compression, which, in turns, leads to a decreasing value of residuals percentage. This phenomenon is in agreement with the observations found in [29].

Figure 23 shows the residuals distribution inside the pre-chamber at spark timing (25 CAD Before Top Dead Center, BTDC), with a very distinctive profile. In particular, it can be seen how the bottom

and central region of the pre-chamber is easily scavenged before the spark, showing little to no sign of residuals presence. By contrast, the most critical area in terms of scavenging is the upper part of the pre-chamber, where high levels of residuals percentage are evidenced.

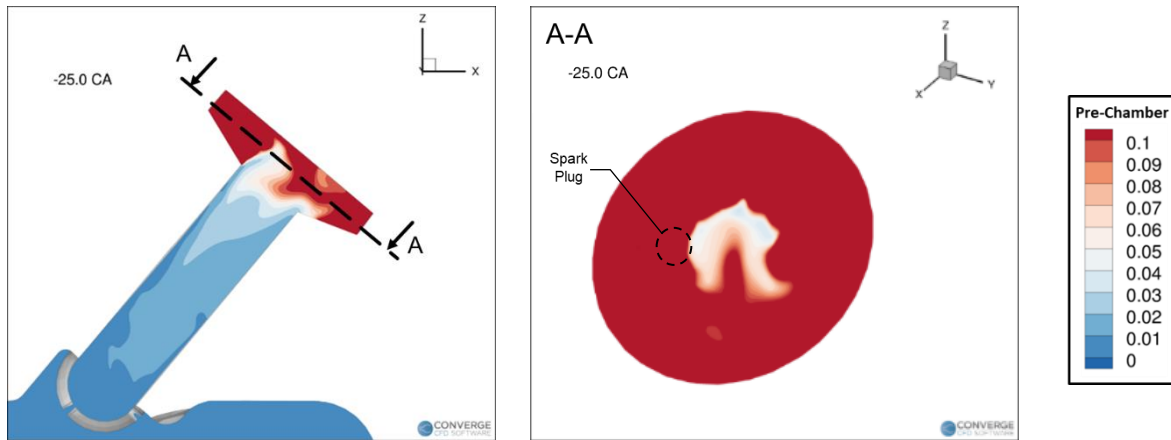


Figure 23: 4000 rpm x  $\lambda=1$  - Residuals Distribution inside PC at 25 CAD BTDC

Figure 24 offers once more the distribution of residuals at spark plug level; however, the different scale used for the spark plug area allows to appreciate a further detail: the residuals are mainly concentrated in the top part of the upper pre-chamber “crown”. Table 14 summarizes the values of residuals percentage on PC average and around spark plug. It is important to address the meaning of “value around spark” as used in this work. Although output data at spark location, as said, via monitor point were available, they were not considered as fully representative of operating conditions, as they were indicating a punctual value. Instead, in an attempt to provide a more reliable parameter, the average value coming from a small sphere around SP was calculated and is here presented

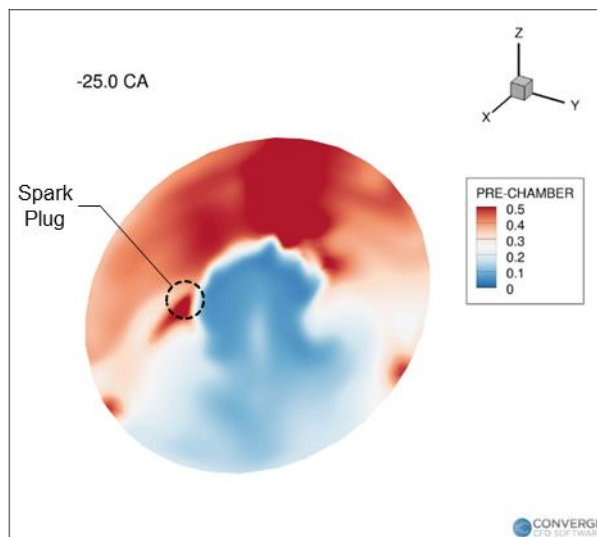


Figure 24: 4000 rpm x  $\lambda=1$  - SP Residuals Distribution

Ultimately, it can be concluded that, due to the particular shape of the pre-chamber, which leads the incoming flow to impact on the PC wall, residuals are prone to be concentrated in the top part of the pre-chamber, with slightly more fresh charge concentrated around the spark plug.

| Case               | PC Residuals Mass<br>@ ST<br>[kg] | PC Intake Charge<br>@ ST<br>[kg] | Residuals %<br>@ ST<br>[%] | Residuals % around<br>SP @ ST<br>[%] |
|--------------------|-----------------------------------|----------------------------------|----------------------------|--------------------------------------|
| 4000 x $\lambda=1$ | 1.01e-06                          | 5.56e-06                         | 15.4%                      | 34.3%                                |

Table 14: 4000 rpm x  $\lambda=1$  – PC Scavenging

### 3.1.1.2 Pre- Chamber Turbulent Kinetic Energy

Another aspect involved in the scavenging process are the conditions set in terms of Turbulent Kinetic Energy TKE. In the same way as fresh charge distribution, TKE plays a key role in PC flame development.

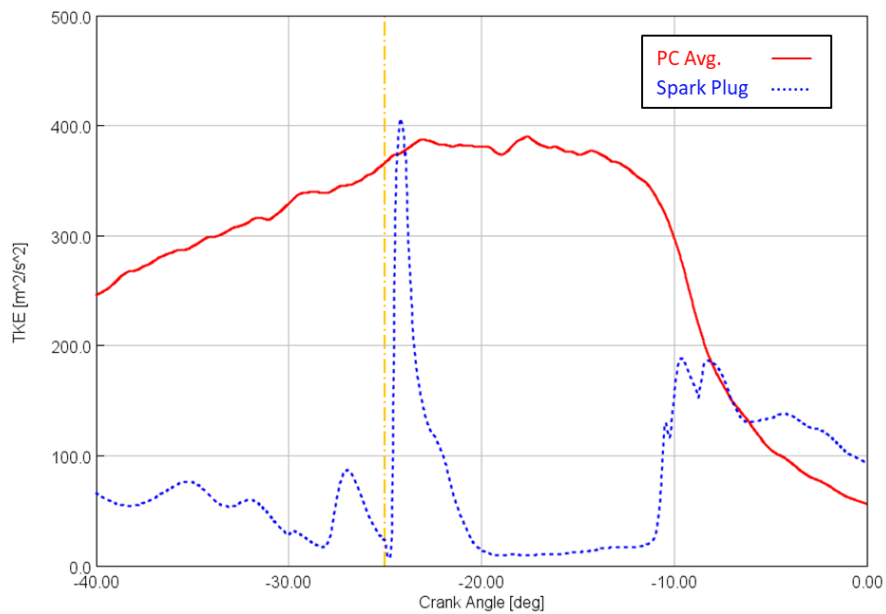


Figure 25: 4000 rpm x  $\lambda=1$  – Turbulent Kinetic Energy (PC Average and Spark Plug)

Figure 25 displays both the average value of TKE inside the PC and the TKE level at the spark plug location, through a monitor point. It can be seen how the level of Turbulent Kinetic Energy inside the PC grows throughout the compression phase, when more and more mass is forced through the PC holes, which are seen by the flow as a restriction. The values at spark plug are the combination of internal flow patterns and are thus not so intuitive or predictable. The sudden peak rising around spark timing is the consequence of the start of a flame development. Average TKE is listed in its numerical values in Table 15, along with the value of TKE around spark plug.

| Case               | TKE (PC avg.) @ ST<br>[m <sup>2</sup> /s <sup>2</sup> ] | TKE around SP @ ST<br>[m <sup>2</sup> /s <sup>2</sup> ] |
|--------------------|---|---|
| 4000 x $\lambda=1$ | 366.5   | 66.6  |

Table 15: 4000 rpm x  $\lambda=1$  – PC Turbulent Kinetic Energy

Figure 26 shows the distribution of TKE at spark timing both on PC average and on a plane passing at SP location.

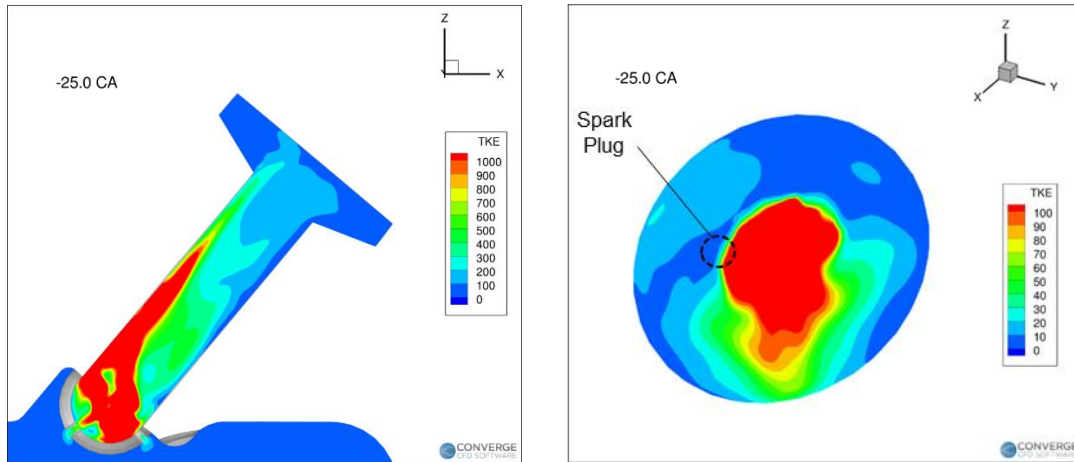


Figure 26: 4000 rpm x  $\lambda=1$  - Turbulent Kinetic Energy Distribution in PC at 25 CAD BTDC

The distribution of TKE along the pre-chamber is quite interesting and dictated by PC shape and tilted position. In particular, it can be noted how the upper part of the pre-chamber body is the most turbulent one. In this regard, the tilted position of the pre-chamber is fundamental for the distribution of TKE, as most of the incoming flow will meet the pre-chamber upper wall and will be guided by it through the entire pre-chamber. To further highlight this aspect, Figure 27 illustrates the TKE distribution in slices of PC progressively reaching the top. In such figure, it can be seen how the upper part of the pre-chamber always remains the most turbulent.

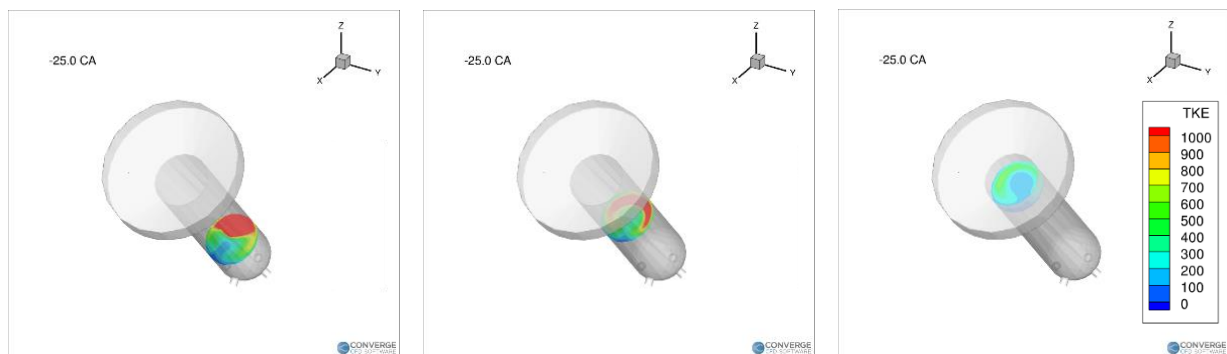


Figure 27: 4000 rpm x  $\lambda=1$  - Turbulent Kinetic Energy Distribution along PC at 25 CAD BTDC

Being heavily dictated by geometry, it was found that TKE development was almost equal in every other analyzed operating point.

While the distribution along PC axis is quite characteristic, the distribution at Spark is very similar to the residuals one, with a highly turbulent region around the center of the PC cylinder and a mildly turbulent one below SP.

### 3.1.1.3 Pre-Chamber Combustion

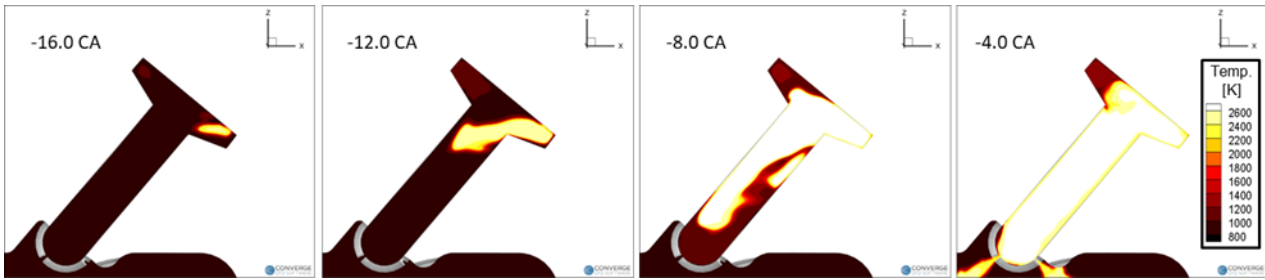


Figure 28: 4000 rpm  $\lambda=1$  – PC Flame Propagation

The development of a flame inside the pre-chamber is predominantly affected by the levels of residuals concentration and Turbulent Kinetic Energy. The former is an aspect complementary to fresh charge distribution and, thus, determines the path along which the flame front will burn it. The latter promotes combustion by corrugating the flame front, widening the effective flame surface and speeding up the burning rate.

Figure 28 illustrates the flame evolution in the pre-chamber at regular crank angle intervals. It can be observed how the flame front follows a preferred path throughout its evolution. Such preferred path, as hinted above, is set by fresh charge distribution and TKE at ST.

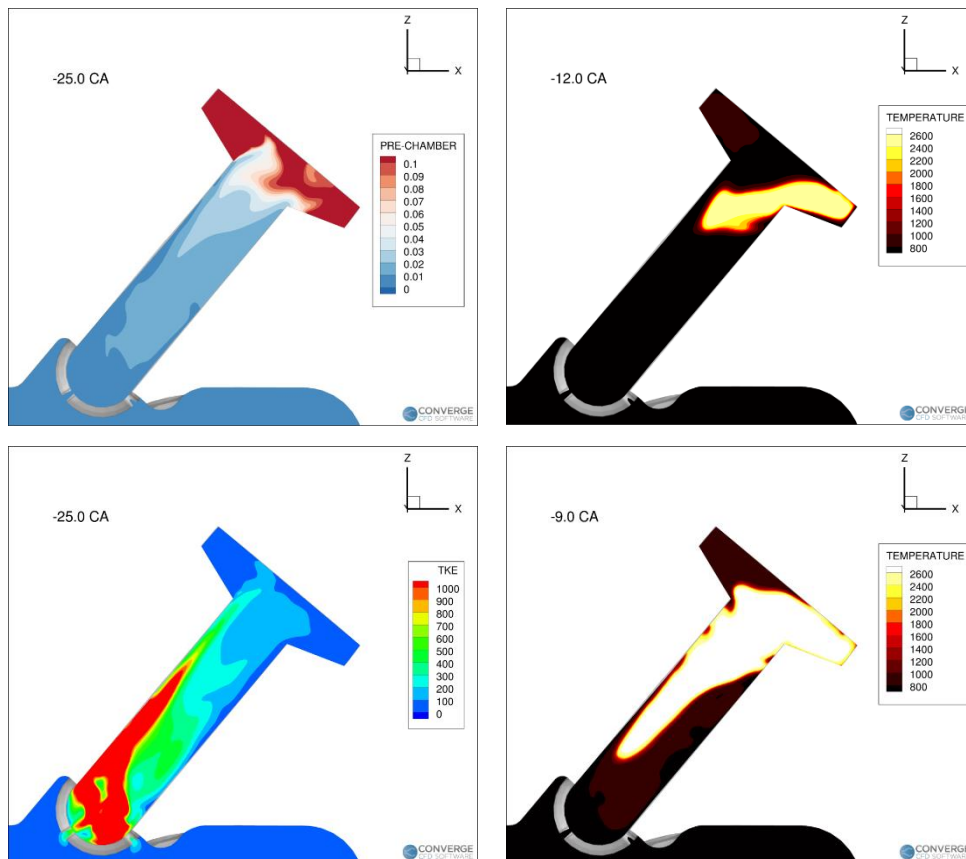


Figure 29: 4000 rpm  $\lambda=1$  – PC Flame Propagation Features

To further highlight this point, Figure 29 is presented, showing flame development at two different crank angles compared to the aforementioned parameters. In particular, in the earliest combustion phase, the flame development is heavily affected by residuals distribution, as no high temperature

zone can be observed in the upper section of the PC “crown” (i.e.: the area with high residuals percentage).

By contrast, the flame is developing in the upper part while travelling through the central part of the pre-chamber. This phenomenon is linked to the burn rate promotion given by higher TKE levels in said area.

Even though this evidence is not analyzed in the context of main chamber combustion, it is still linked to the events taking place in the cylinder. As a matter of fact, it is reasonable to assume that an unevenness in the PC flame front will translate into non-uniform jet distribution and MC ignition sites, with a likely impact on main combustion event in terms of performance and emissions.

After spark timing, the combustion process creates a pressure rise inside the pre-chamber. Once such pressure overcomes the pressure level in the cylinder, a flow rate of hot jets from PC to MC arises, which, by mixing with the fresh mixture in the cylinder, causes ignition and the start of the main combustion event.

Finally, Figure 30 illustrates the PC combustion event and jet injection phase with the start of MC combustion, by tracing the flame front via temperature profiles.

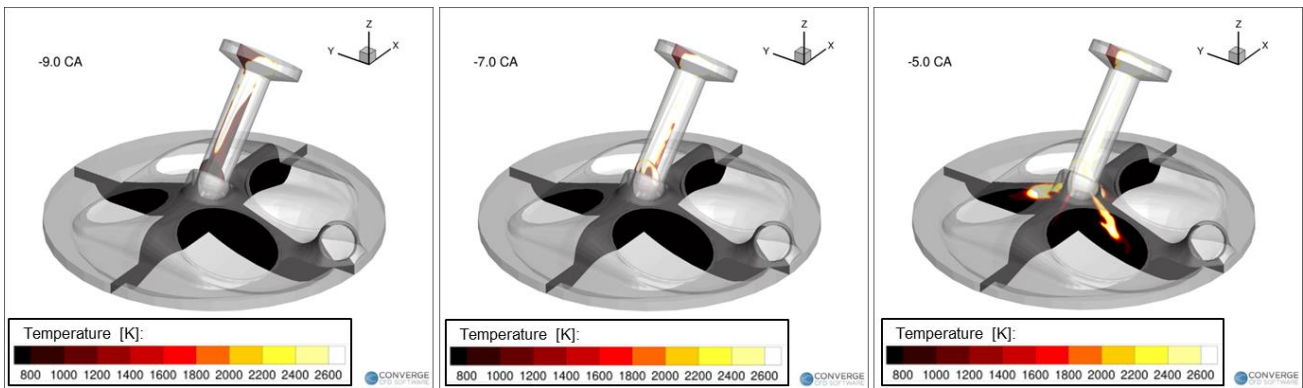


*Figure 30: 4000 rpm  $\times \lambda=1$  – PC Combustion and Jet Injection*

### 3.1.1.4 Main Chamber Combustion

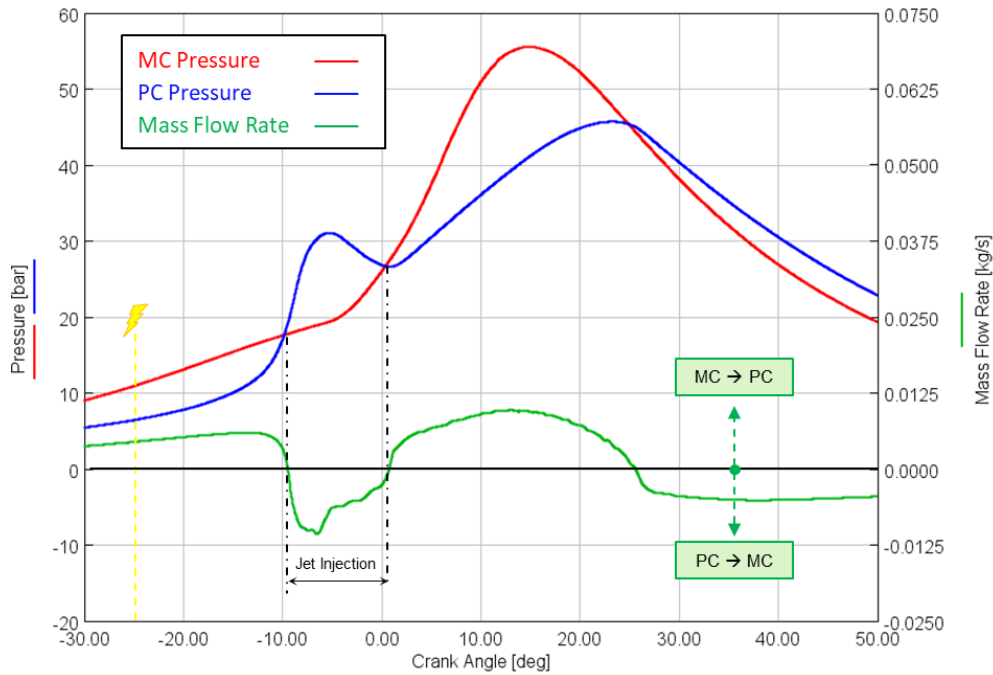


Figure 31: 4000 rpm  $\times \lambda=1$  – PC/MC Pressure Profiles and Mass Flow Rate

The pressure traces for MC and PC, as well as PC-MC mass flow rate, are reported in Figure 31. It is interesting to notice how the pressure rise in the main chamber is coincident, except for a minor delay, to the exiting of the jets from the pre-chamber: this confirms the interaction between turbulent jets exit and start of the main combustion event.

Moreover, Figure 32 helps in showing the two different phases of MC combustion ([30], [31]). The initial phase is jet propagation, the phase in which the main contribution to the burn rate is given by the propagation of the hot jets along their axes. In the second, phase, a conventional flame front is able to develop from said jets in a peripheral direction, hence allowing to consume the fresh charge inside the cylinder.

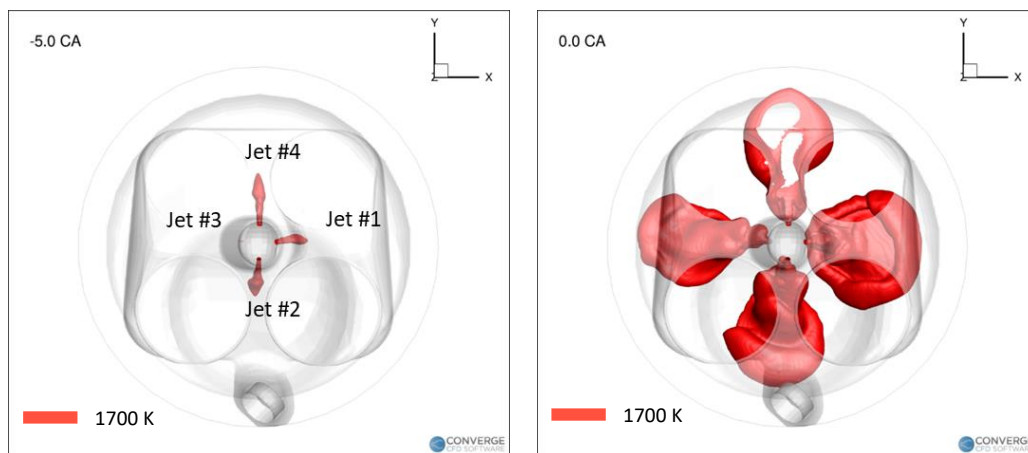


Figure 32: 4000 rpm  $\times \lambda=1$  – Jet and Flame Propagation in MC represented by gas iso-surface at  $T=1700$  K

Always from Figure 32 it is possible to notice a certain degree of variability among the behavior of the different jets, an outcome of the non-symmetric shape of the pre-chamber. In particular, jet #3 appears as significantly delayed with respect to the other jets.

Although the turbulent jets are exiting with different timings, after 5 crank angle degrees they appear as more homogeneously distributed. The reason for such phenomenon is to be found in the conditions in the main chamber at jet exit. In this framework, Figure 33 shows the distribution of TKE across two planes of the main chamber, cutting along the X and Y axes.

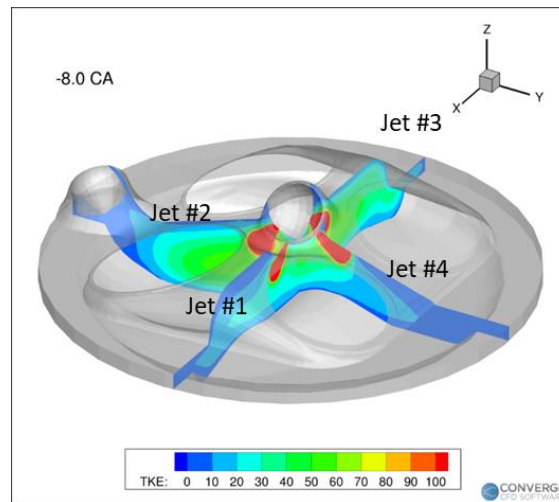


Figure 33: 4000 rpm  $\times \lambda=1$  – Cylinder TKE Distribution (3D View)

A degree of disparity in TKE distribution appears as evident inside the cylinder around jet exit timing: specifically, the areas projected to be hit by jets #2 and #3 show signs of higher TKE. For what concerns jet #3, this fact is beneficial for the propagation of the flame and recover the initial delay. The reason behind the inhomogeneity in TKE along the X-axis plane was related to the particular shape of the cylinder head (in Figure 34), which is slightly asymmetrical. This fact could cause a particular pattern in the flow field inside the cylinder, leading to an asymmetric TKE distribution.

In a much simpler way, the difference in TKE level along the Y-axis slice was assumed to be due to the particular shape of the piston, which has a lowered crown on the intake valves side.

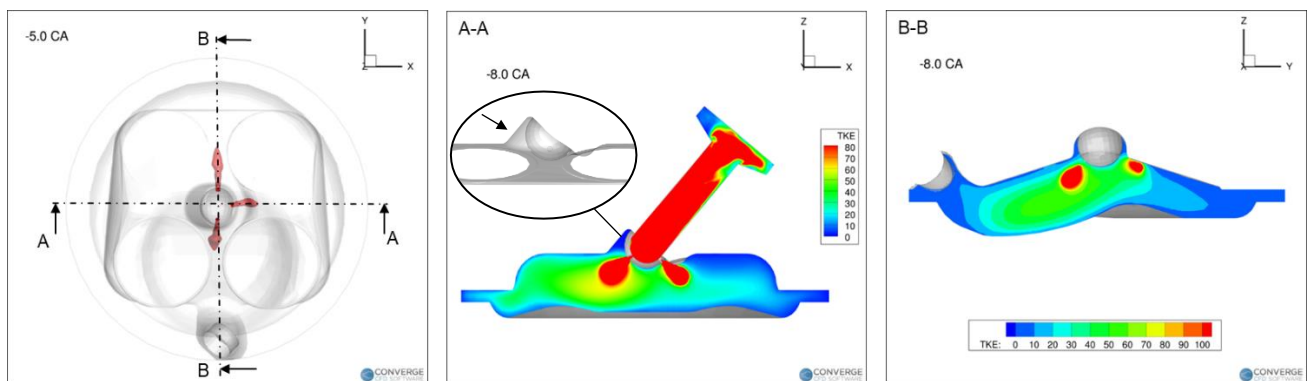


Figure 34: 4000 rpm  $\times \lambda=1$  – Cylinder TKE Distribution (Slices)

### 3.1.1.5 Flow Reversal

Once the combustion in the main chamber starts, pressure rises up to the point where it overcomes once again the level of PC pressure. It is at that point that a flow reversal event occurs: due to said pressure difference, the jet injection phase ends and the flow rate exchange between the chambers changes direction, leading to a flow reversal. This second stage brings reactive species from the main-chamber back to the pre-chamber, where they will ultimately be consumed, as exhibited by the second peak in the Heat Release Rate trace inside the pre-chamber, as illustrated in Figure 35. It is worth noting that the second peak occurs in a region with positive mass flow rate, indicating a flow from main chamber to pre-chamber.

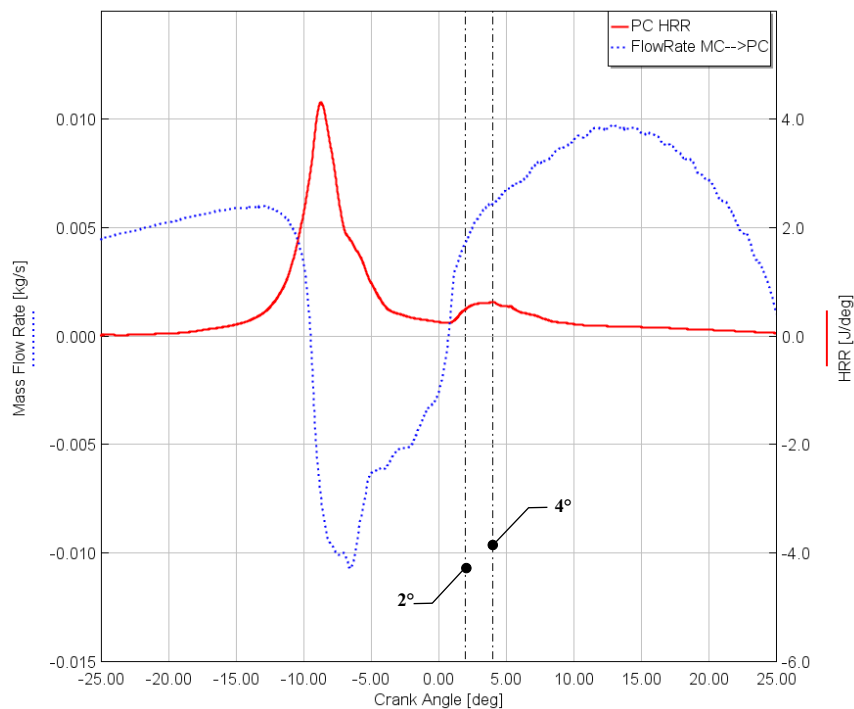


Figure 35: 4000 rpm x  $\lambda=1$  – MC to PC mass flow rate and PC HRR

Furthermore, Figure 36 illustrates the trends of Turbulent Kinetic Energy and OH mass fraction during the flow reversal event at the two time instants reported in Figure 35. The behavior of TKE demonstrates the change in direction of the flow, going from main-chamber, through the holes and into the PC, merging in the bottom part of it. The same distribution is followed by OH mass fraction, a parameter used to track the flame position. This evidence also proves how during the flow reversal phase fresh species are brought from cylinder to pre-chamber and burned, leading to the second peak in HRR inside PC.

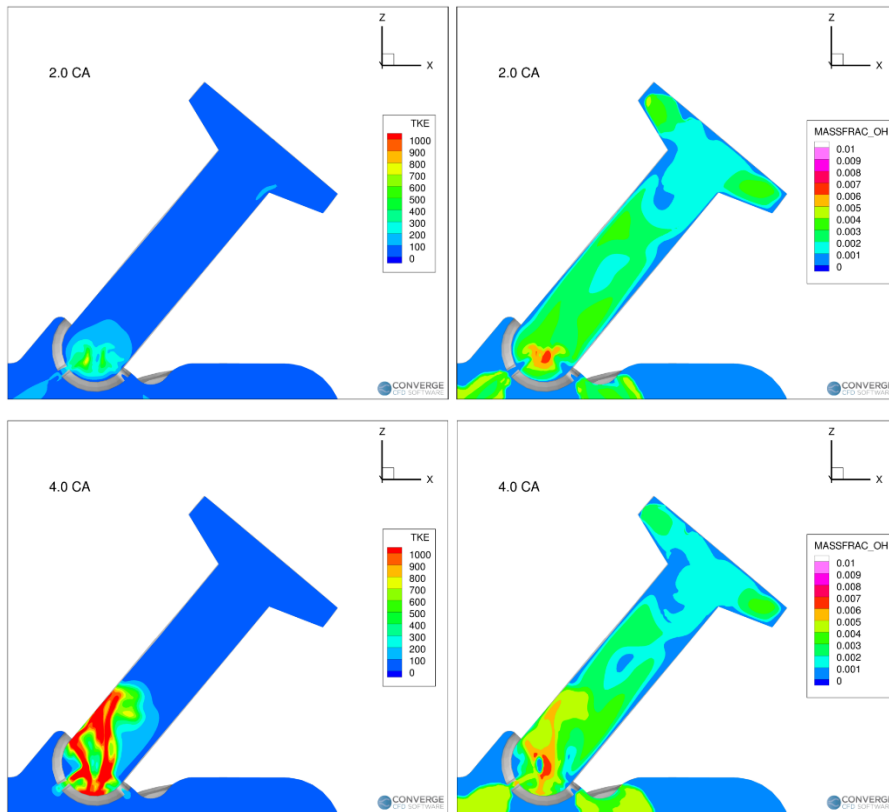


Figure 36: 4000 rpm x  $\lambda=1$  – Flow Reversal (OH and TKE Distribution)

### 3.1.2 4000 rpm x $\lambda=1.2$

The second investigated case is 4000 rpm and lean operation ( $\lambda=1.2$ ). Although the blueprint of the following study is the same as the one previously presented, this operating point will be investigated in the context of a comparison with the stoichiometric case.

It can be already anticipated that a fundamental aspect between the two cases will be the different spark timing, which will dictate most of the disparity

#### 3.1.2.1 Pressure & HRR Results

Differently from the stoichiometric conditions, the lean operated case falls inside the experimental interval (Figure 37), both in terms of cylinder pressure and HRR. Nevertheless, the simulated results are still representative of a fast-burning engine cycle with respect to the experimental average.

It is interesting to notice the start timing of the main combustion event in lean operation, which appears as extremely delayed with respect to spark discharge in the pre-chamber, at 69 CAD BTDC, as noticeable by the MFB10 values in Table 16.

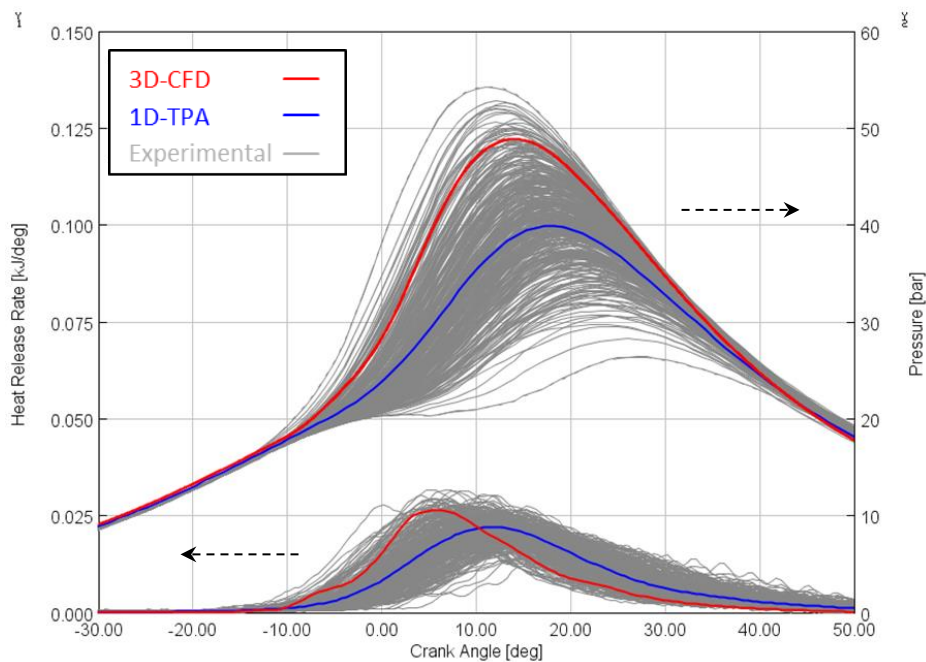


Figure 37: 4000 rpm x  $\lambda=1.2$  - Pressure and HRR Profiles

Table 16 and Figure 38 show numerically and graphically the Mass Fraction Burned angles as well as the burn duration. It can be rightfully observed how the lean mixture burn duration increases with respect to the stoichiometric case; vice versa, the difference in burn duration between experimental and simulated results appears to remain similar, around 3 CAD.

| Model  | MFB10<br>[CAD] | MFB50<br>[CAD] | MFB90<br>[CAD] | Burn Duration10-90<br>[CAD] |
|--------|----------------|----------------|----------------|-----------------------------|
| 1D-TPA | 1.2            | 13.6           | 29.0           | 27.8                        |
| 3D-CFD | -1.7           | 8.3            | 22.9           | 24.7                        |

Table 16: 4000 rpm x  $\lambda=1.2$  – Burn Duration

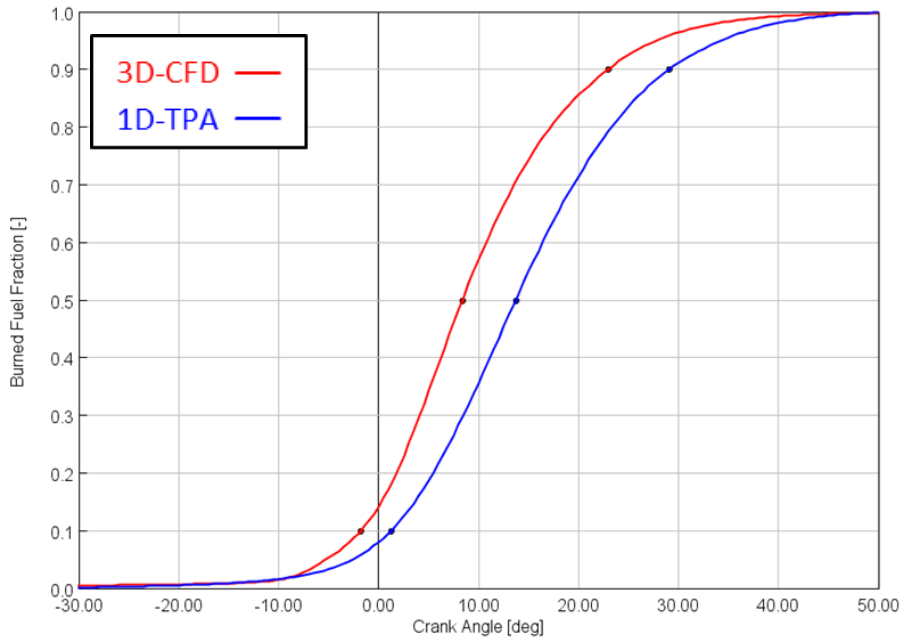


Figure 38: 4000 rpm x  $\lambda=1.2$  – Mass Fraction Burned

### 3.1.2.2 Pre-Chamber Scavenging

Previous results show that an earlier spark timing corresponds to less time available for the piston to push fresh charge inside the pre-chamber during the compression stroke.

Figure 39 seems to confirm such results, showing that the ST anticipation of around  $45^\circ$  is critical for the definition of residuals percentage. Moreover, Figure 40 is provided, showing that the cause of hindered scavenging is the significantly lower mass of fresh charge pushed in PC, since the residuals mass present at spark timing is pretty much the same.

Besides the effects on residuals quantity, it is also important to underline the impact of the different operating conditions on residuals distribution across the pre-chamber.

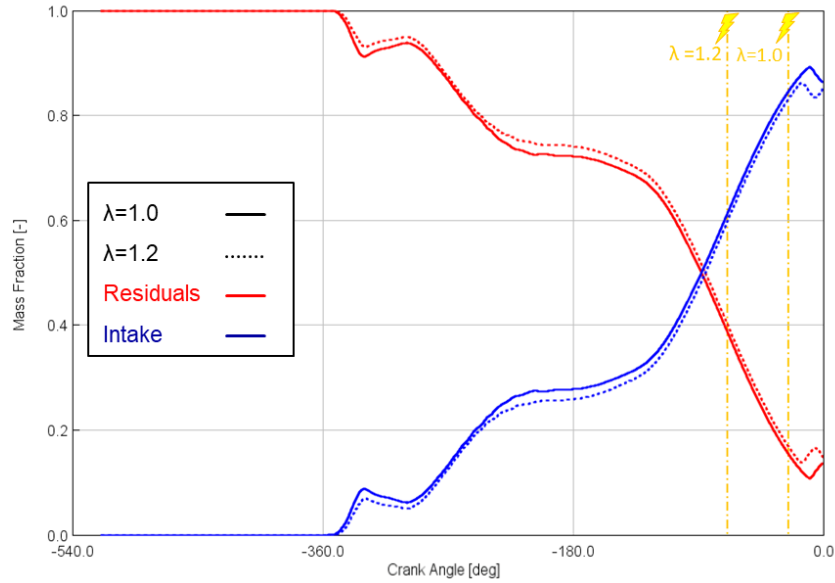


Figure 39: 4000 rpm x  $\lambda=1$  VS 4000 rpm x  $\lambda=1.2$  - Residuals and Intake Mass Fraction inside PC

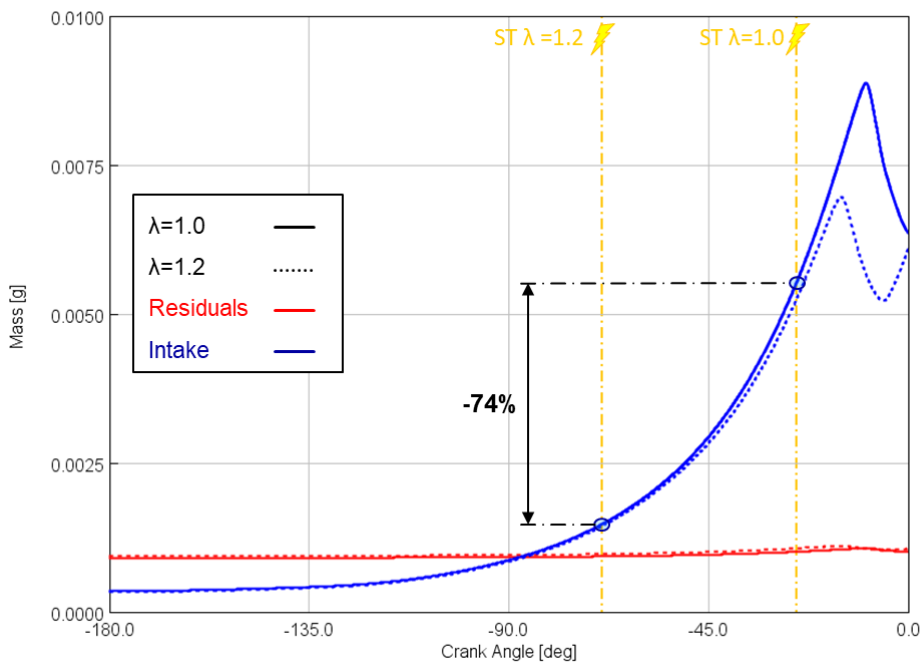


Figure 40: 4000 rpm x  $\lambda=1$  VS 4000 rpm x  $\lambda=1.2$  - Residuals and Intake Mass inside PC

Figure 41 expresses said impact pretty clearly, showing that for the lean mixture case the residuals distribution is much worse than in the baseline case, having almost the entire pre-chamber filled with residuals at spark timing.

To conclude, the stoichiometric case has a better scavenging performance thanks to its later ST. More time to push fresh charge inside the pre-chamber translates, in turns, to less residuals percentage while allowing to compress them in the upper part of the pre-chamber instead of populating most of it.

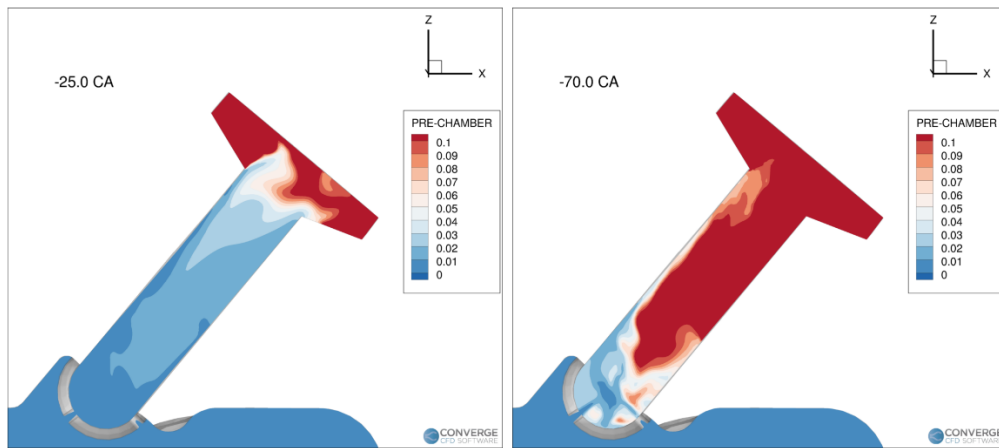


Figure 41: Residuals Distribution - 4000 rpm x  $\lambda=1$  (left) VS 4000 rpm x  $\lambda=1.2$  (right)

Finally, Table 17 summarizes all the numerical values describing the analysis of the scavenging process. The outcome of the previous considerations leads to a difference in residuals percentage at spark timing of more than 25%. Moreover, also the oxygen concentration around spark plug is reported: it can be seen how the worsened scavenging leads to an almost halved value of oxygen concentration.

| Case                 | ST<br>[CA aTDCf] | Residuals<br>Mass @ ST<br>[kg] | Intake Mass<br>@ ST<br>[kg] | Residuals %<br>(PC avg.)<br>@ST<br>[%] | O2 % around<br>SP @ ST<br>[%] |
|----------------------|------------------|--------------------------------|-----------------------------|--|-------------------------------|
| 4000 x $\lambda=1$   | -25              | 1.01e-06                       | 5.56e-06                    | 15.4%                                  | 19.8%                         |
| 4000 x $\lambda=1.2$ | -69              | 9.70e-07                       | 1.44e-06                    | 40.8%                                  | 10.0%                         |

Table 17: 4000 rpm x  $\lambda=1$  VS 4000 rpm x  $\lambda=1.2$  – PC Scavenging

### 3.1.2.3 Pre-Chamber Turbulent Kinetic Energy

The trend of average Turbulent Kinetic Energy inside the pre-chamber is represented in Figure 42. The difference between the two cases appears as quite evident, with the  $\lambda=1.2$  case having much less turbulent conditions inside the pre-chamber.

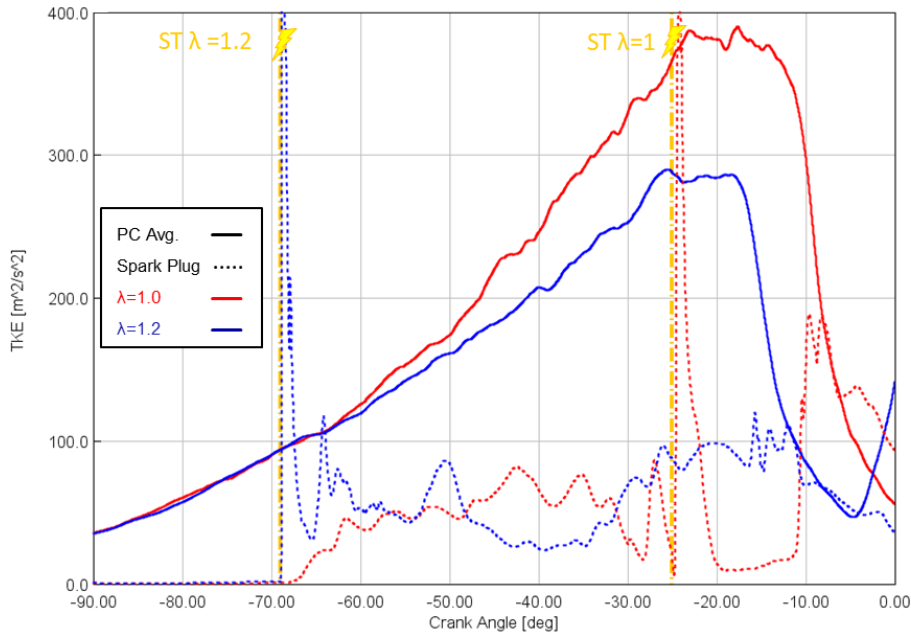


Figure 42: 4000 rpm x  $\lambda=1$  VS 4000 rpm x  $\lambda=1.2$  – Turbulent Kinetic Energy (PC Average and Spark Plug)

Table 18 reports the numerical values of TKE levels inside the pre-chamber (average) and around the spark plug. The extremely early ST for the lean operation case leads to a stationary condition inside the pre-chamber, as there is not enough time for a turbulent flow to be established and develop throughout the pre-chamber. As a matter of fact, the TKE appears to decrease by roughly 75% Compared to the value reached at ST for the stoichiometric case. Moreover, TKE around the spark plug is basically non-existent, so much so that the PC combustion event can be assumed to be starting in a quiescent condition.

| Case                 | ST<br>[CA aTDCf] | TKE (PC<br>avg.) @ ST<br>[m <sup>2</sup> /s <sup>2</sup> ] | TKE around<br>SP @ ST<br>[m <sup>2</sup> /s <sup>2</sup> ] |
|----------------------|------------------|--|--|
| 4000 x $\lambda=1$   | -25              | 366.5  | 66.6   |
| 4000 x $\lambda=1.2$ | -69              | 90.7   | 3.09   |

Table 18: 4000 rpm x  $\lambda=1$  VS 4000 rpm x  $\lambda=1.2$  – PC TKE

The difference between the two operating points is very well pictured by Figure 43, showing the trends of turbulent kinetic energy in a pre-chamber cross section and at spark plug. The cross-section view demonstrates the inability of a turbulent flow to be developed throughout the pre-chamber due to the early ST.

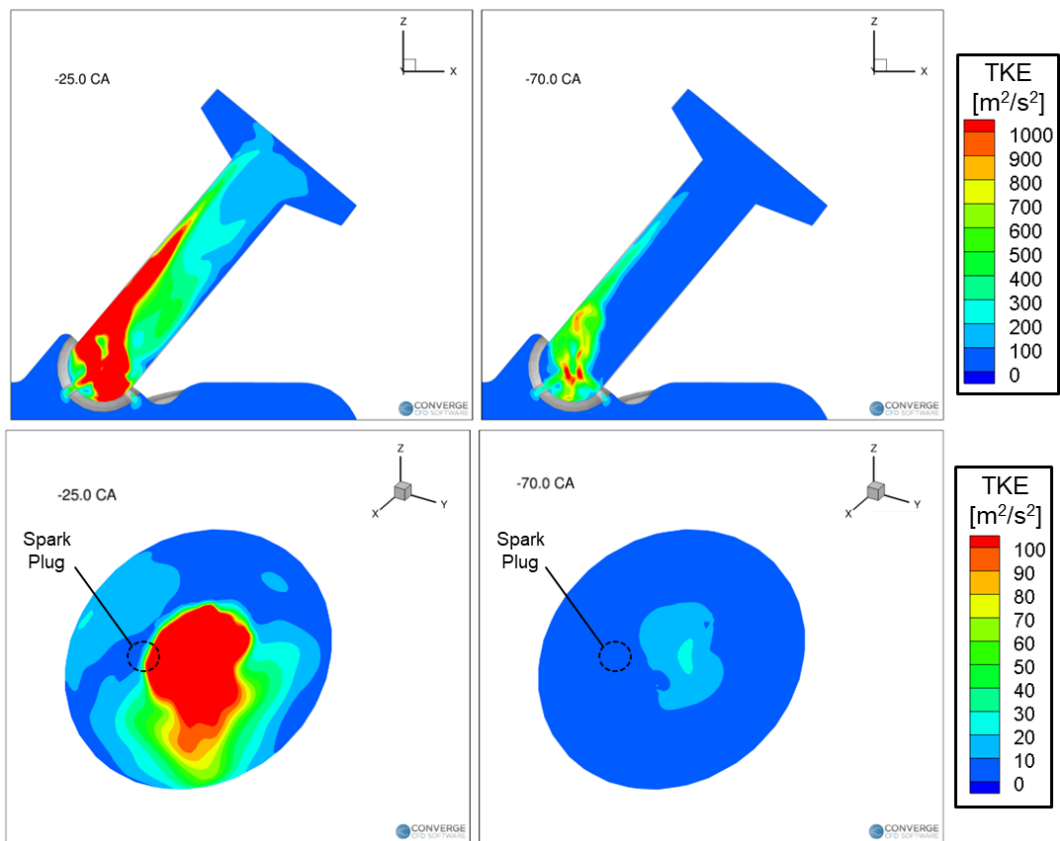


Figure 43: Turbulent Kinetic Energy Distribution - 4000 rpm  $\lambda=1$ (left) VS 4000 rpm  $\lambda=1.2$  (right)

### 3.1.2.4 Combustion and MC/PC Flow Analysis

Pre-chamber combustion for the lean case is heavily affected by its very early ST, which sets the start of combustion in unfavorable conditions.

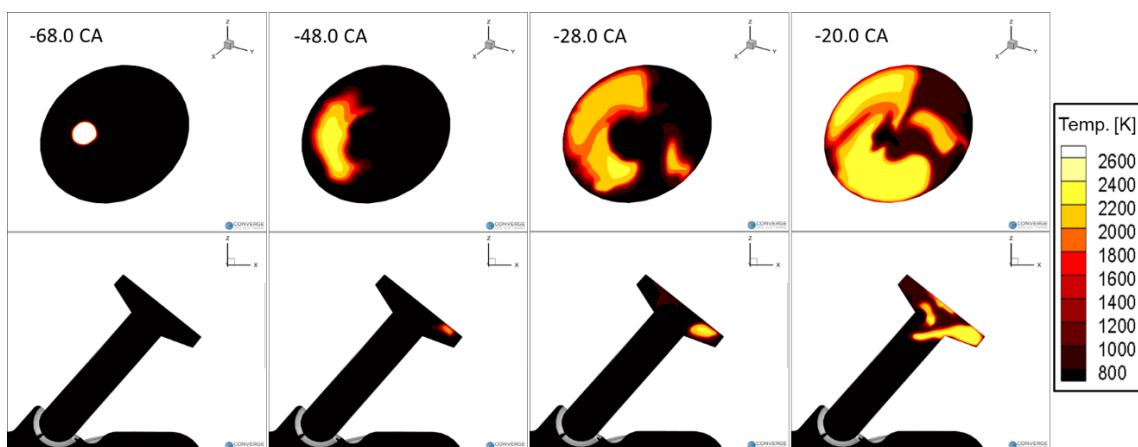


Figure 44: 4000 rpm  $\lambda=1.2$  – PC Flame Development

After ST, although the flame keeps being on the edge of extinction for a quite large period of time, it is finally able to ignite the whole pre-chamber. As a matter of fact, almost 50 crank-angle degrees are needed for the flame to propagate inside the central part of the pre-chamber, as shown in Figure 44. The results in terms of pressure traces in MC and PC, and consequent mass flow rate, for both the stoichiometric and lean operated case are illustrated in Figure 45. It is interesting to notice that, despite the big difference in spark timing, the combustion events (PC and MC) characterizing the two operating points are not very far one from the other.

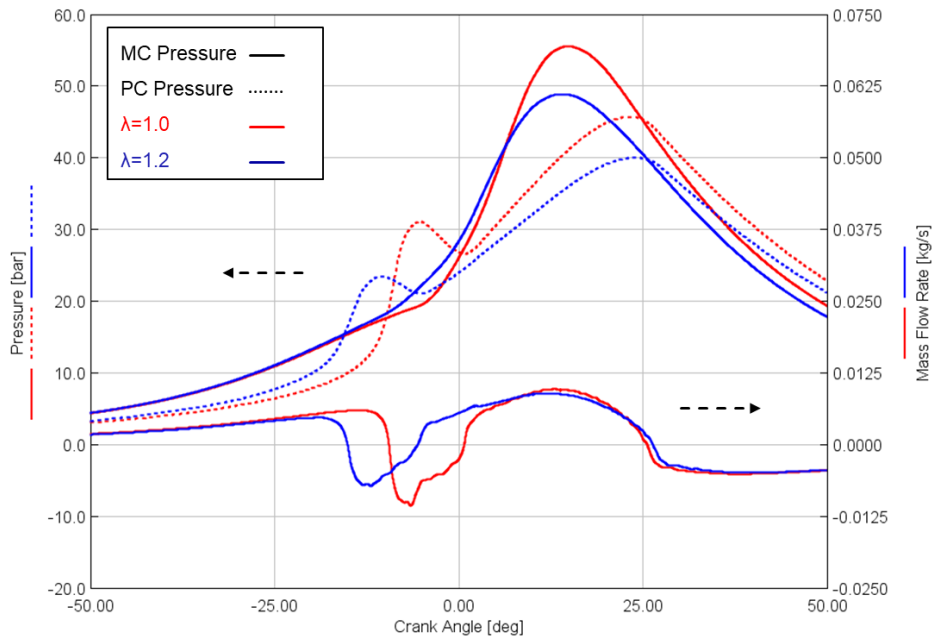


Figure 45: 4000 rpm x  $\lambda=1.0$  VS 4000 rpm x  $\lambda=1.2$  – PC and MC Pressure

The leaner case shows lower peak pressures, which in turns leads to a lower pressure difference with the main chamber; the resulting jet injection phase, thus, is less intense than the baseline case, as noticeable by the lower peak in mass flow rate. However, despite the lower intensity, the jet injection phase duration seems to remain unaltered. Figure 46 seems to confirm this trend, correlating to a lower HRR inside the PC (leaner case) a lower peak mass flow rate during the jet injection phase.

| Case                 | Jet Injection Duration [CAD] | Jet Injection Peak Mass Flow Rate [m/s] |
|----------------------|------------------------------|---|
| 4000 x $\lambda=1$   | 10.2                         | 1.1e-02                                 |
| 4000 x $\lambda=1.2$ | 9.6                          | 7.2e-03                                 |

Table 19: 4000 rpm x  $\lambda=1.0$  VS 4000 rpm x  $\lambda=1.2$  – Jet Injection

| Case                 | Flow Reversal Duration [CAD] | Flow Reversal Peak Mass Flow Rate [m/s] | Flow Reversal HRR Peak [J/deg] |
|----------------------|------------------------------|---|--------------------------------|
| 4000 x $\lambda=1$   | 24.8                         | 9.7e-03                                 | 6.2e-01                        |
| 4000 x $\lambda=1.2$ | 31.9                         | 9.0e-03                                 | 4.8e-01                        |

Table 20: 4000 rpm x  $\lambda=1.0$  VS 4000 rpm x  $\lambda=1.2$  – Flow Reversal

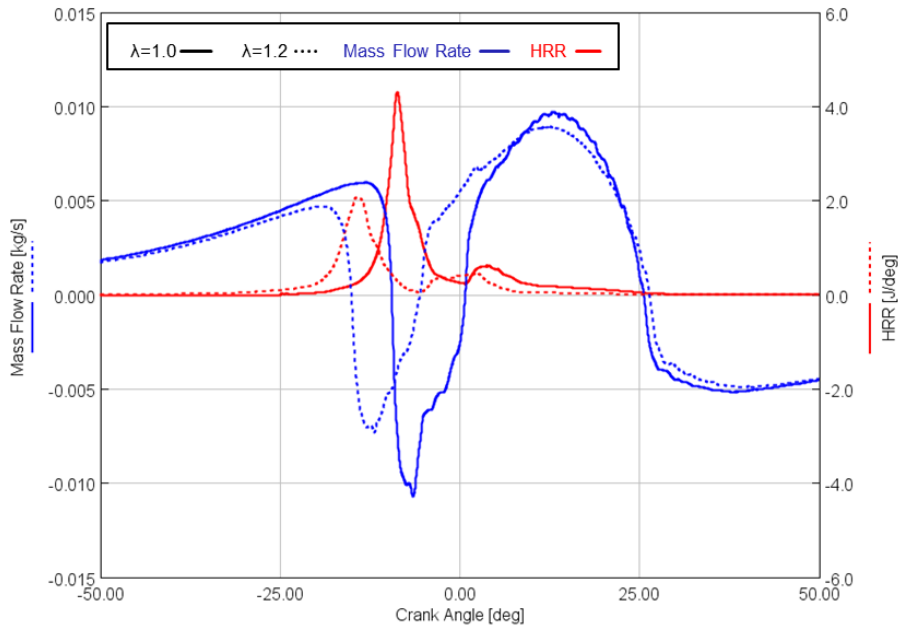


Figure 46: 4000 rpm x  $\lambda=1.0$  VS 4000 rpm x  $\lambda=1.2$  – PC HRR and Mass Flow Rate

The pressure trace in the leaner case shows rightfully a lower peak, due to the lower amount of fuel stored in the cylinder with respect to the stoichiometric case. Furthermore, the rate of pressure rise in the main chamber appears as smoother, likely as a combination of lower energy content in the cylinder (leaner mixture) and lower jet velocity, which are in turns the promoters of the main combustion event. This smoother rise translates in a longer time needed for the main chamber pressure to equal the pre-chamber pressure and stopping jet injection from the pre-chamber, likely justifying the constancy of the jet injection duration.

As a final note, it is quite interesting to notice that although the flow reversal phase increases by roughly 7 crank-angle degrees in the leaner case (Table 20), the peak flow rate seems to remain unchanged, hinting, in a subsonic flow regime, that also the maximum pressure difference between main chamber and pre-chamber remains unchanged when operating in stoichiometric or lean operation at 4000 rpm.

## 3.2 Model Calibration

The results obtained in baseline configuration open up the opportunity for a refinement of the model, in order to match more closely the experimental results. In particular, the sensitivity of the model on turbulent Prandtl number and pre-chamber geometry was investigated.

It was already addressed how TJI is a combustion strategy heavily relying on turbulence effects between hot jets and in-cylinder fresh charge. However, the relative contribution between thermal effects and turbulent mixing defining the interaction between turbulent jets and fresh charge is far from being rigorously defined.

Having no tomographic evidence of the pre-chamber geometry, the influence of its design on the model results was addressed by altering two features: holes diameter and holes rotation

Pre-chamber holes diameter is one of the most important design parameters affecting TJI operation. Its influence has been studied extensively through the years . To analyze the sensitivity of the present engine on such parameter, simulations with different hole diameters were performed. As no tomography of the PC was available, this feature was suspected to be a possible cause of the discrepancy between experimental and numerical results. The following sections will discuss the main outcomes of said simulations while trying to compare them to the experiences coming from the literature. In particular, the pre-chamber holes for the present engine were varied according to the following values: 0.8 mm, 0.9 mm, 1.0 mm (baseline) and 1.1 mm.

The analysis was carried out for the 4000 rpm test cases, for both stoichiometric and lean operation. Moreover, results at 2000 rpm will be reported, as they introduce interesting considerations in the analysis. A more detailed description for the 4000 x lambda=1 case will be provided to understand the effects of such change in geometry, while only a short description for the 2000 rpm cases will be given as the qualitative outcome was practically the same. The lean case at 4000 rpm will not be described in depth, as the very early ST did not allow to observe significant differences in pre-chamber conditions at time of spark discharge

### 3.2.1 Change in Prandtl Number – 4000 rpm x lambda=1

In this framework, the relative contribution of turbulence and thermal effects is referred by Prandtl number ( $Pr_t$ ), which in turbulent terms are expressed as:

$$Pr_t = \frac{\textit{Turbulent Momentum Diffusivity}}{\textit{Turbulent Thermal Diffusivity}}$$

As discussed, when adopting a RANS approach, all turbulent scales are not resolved, but modelled. As a consequence, the turbulent viscosity will depend on the turbulence model used, while the turbulent thermal diffusivity is assumed to be linked to the momentum diffusivity by a simple scalar value: the turbulent Prandtl number.

Hence, the turbulent Pr number can be considered as a “calibration” parameter for the 3D-CFD model, being able to adjust the relative contribution of thermal and momentum diffusivity, characterizing also the jet-fresh charge interaction outlining the combustion process. Using the standard value of

$Pr=0.9$ , increasing the turbulent Prandtl number would translate into considering the momentum diffusivity to be more important than the thermal diffusivity.

In order to do optimize the combustion event captured by the 3D-CFD model, a calibration of turbulent Prandtl number was attempted.

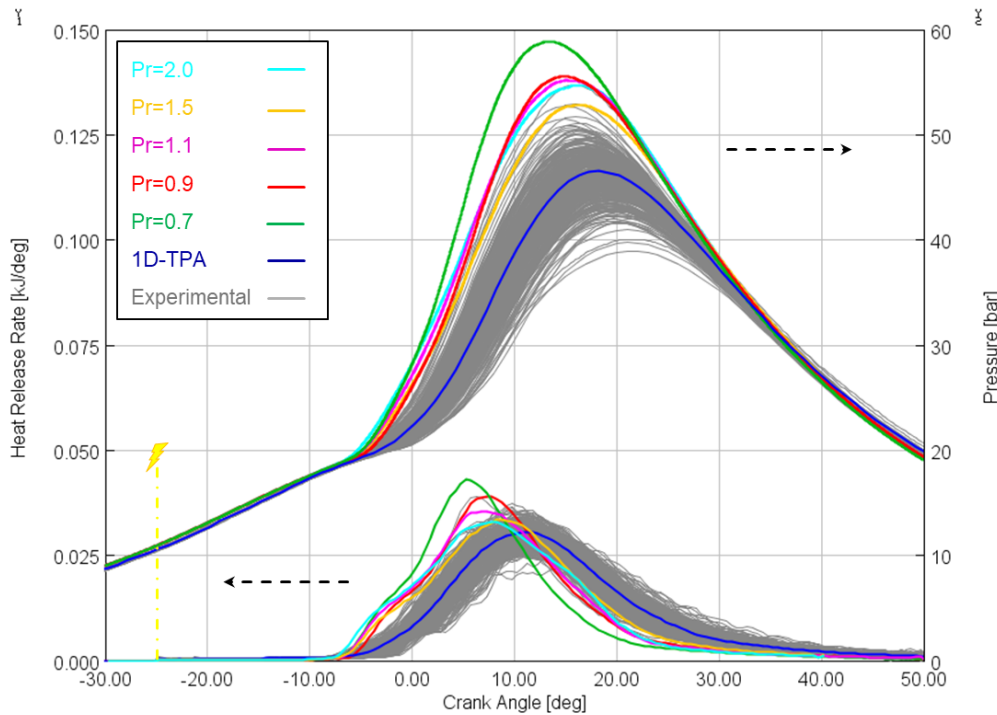


Figure 47: 4000 rpm x  $\lambda=1.0$  – Main Chamber Pr Sweep

At first, values of  $Pr$  equal to 0.7, 0.9 and 1.1 were attempted and imposed and all the regions of the computational domain. The results, omitted for brevity, were not satisfactory: changing  $Pr$  in all the regions also affected the combustion in the pre-chamber, affecting combustion timing with no improvement whatsoever in terms of in-cylinder pressure trace.

Instead, new trials with a change in Prandtl number only inside the main chamber were carried out. This was thought to be a better practice, due to the fact that while combustion timing, mainly dictated by PC combustion, was already quite accurate, only the initial stages of MC combustion were drifting away from experimental results. This observation is also consistent with the fact that a turbulent cascade is expected to happen in the MC just after the development of PC jets, and this phenomenon is likely the most difficult to be represented by a RANS model using a single Prandtl number. Turbulent Prandtl number was thus varied only in the main chamber with the following values: 0.7, 0.9, 1.1, 1.5 and 2.0.

Figure 47 reports the trends of in-cylinder pressure and HRR for the new test cases. Increasing the Prandtl number inside the main chamber has been proved to be beneficial for the results. In fact, lower pressure peaks and lower Heat Release Rate peaks are observed as  $Pr$  increases. Moreover, such peaks are shifted more and more towards the expansion stroke, as a sign of a combustion event with lower intensity. In particular, the case with  $Pr=1.5$  seems to fall inside the experimental interval more effectively than all the other cases.

Unluckily, these considerations hold true only on a small interval of Pr sweep, whereas a crossover value is found for  $Pr=2.0$ : after this point, the results appear once again to be close to the baseline ones.

Finally, it can be concluded that the change in turbulent Prandtl number was proved to be an effective calibration parameter in the modelling of TJI combustion. However, this modification seems to be unable on its own to represent the average experimental cycle for this engine and in this operating conditions. The examined sensitivity, ultimately, indicates that a change in turbulent Prandtl number should be followed by a change in other setup parameters, in order to push the numerical results closer to the experimental ones.

### 3.2.2 Pre-Chamber Holes Diameter Sweep – 4000 rpm x $\lambda=1$

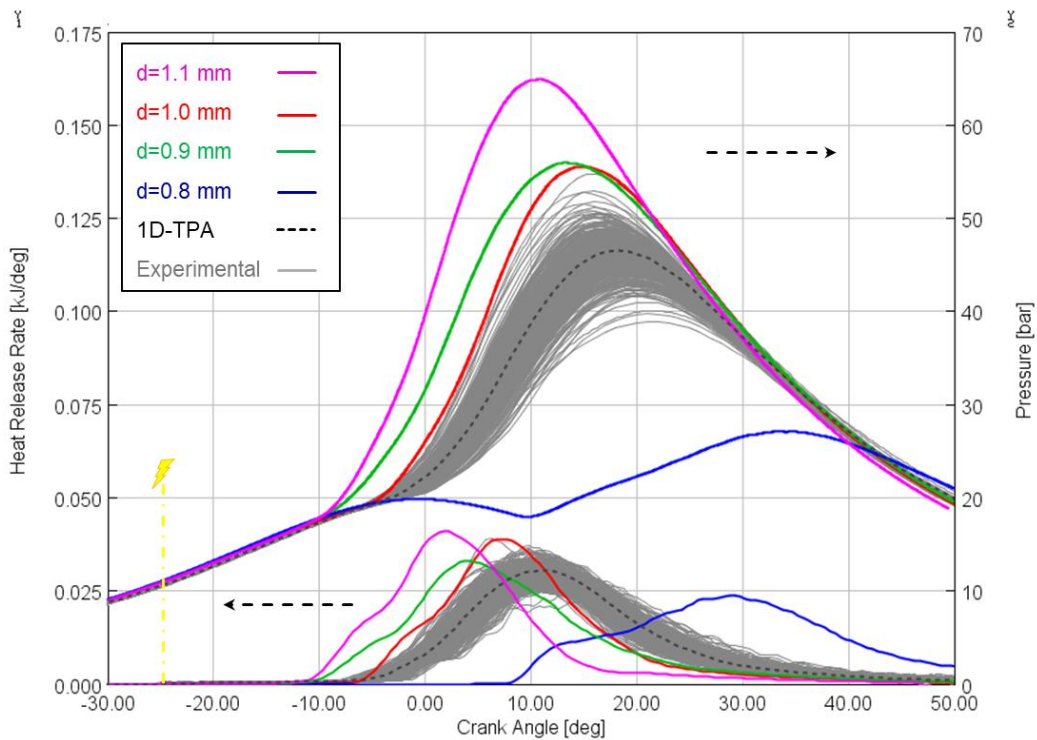


Figure 48: 4000 rpm x  $\lambda=1.0$  – Pre-Chamber Hole Diameter Sweep

To start, Figure 48 represents the pressure and HRR results for each case along with the TPA and experimental ones. The following sections will investigate in detail the effects of diameter change for each case.

#### 3.2.1 Pre-Chamber Scavenging

This section summarizes the investigation on the impact of pre-chamber holes diameter on pre-chamber scavenging. The trace of residuals and intake charge mass fractions is represented in Figure 49. The gas exchange performance in the pre-chamber is better (i.e.: with lower residuals and more fresh charge presence) when increasing the hole diameter. The evidence from the previous sections suggests that the main reason for such behavior is the higher ability of a larger hole to bring inside the pre-chamber a larger quantity of fresh charge from the cylinder; Figure 50 confirms this fact, showing that at spark timing the mass of air/fuel mix stored in the pre-chamber is higher in the case of larger holes. Reported percentage errors show the deviation with respect to the baseline case (d=1.0 mm)

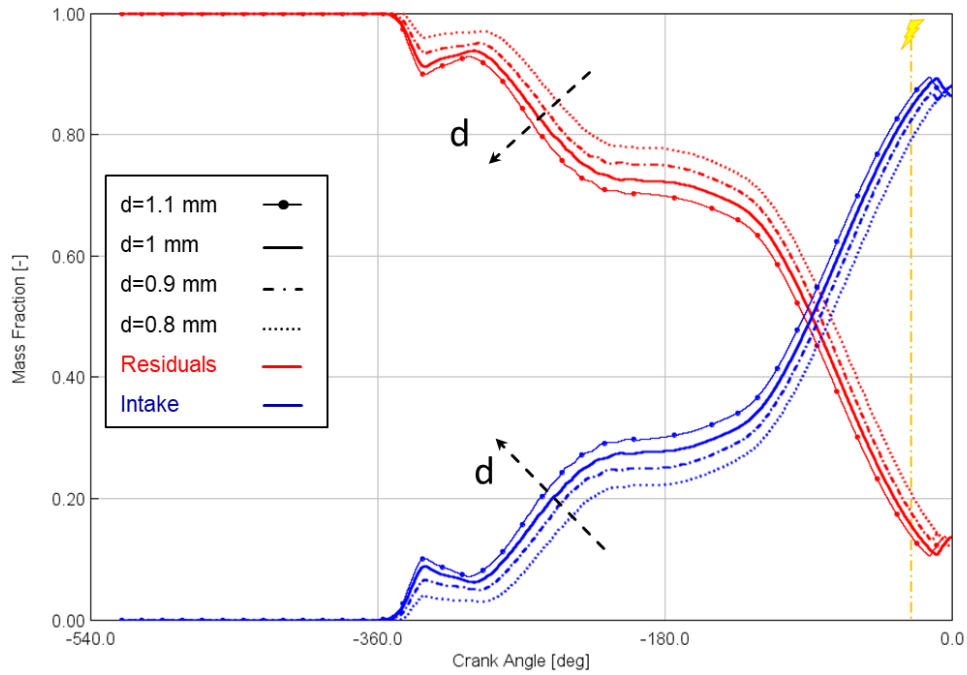


Figure 49: Holes Diameter Sweep – PC Residuals and Intake Concentration

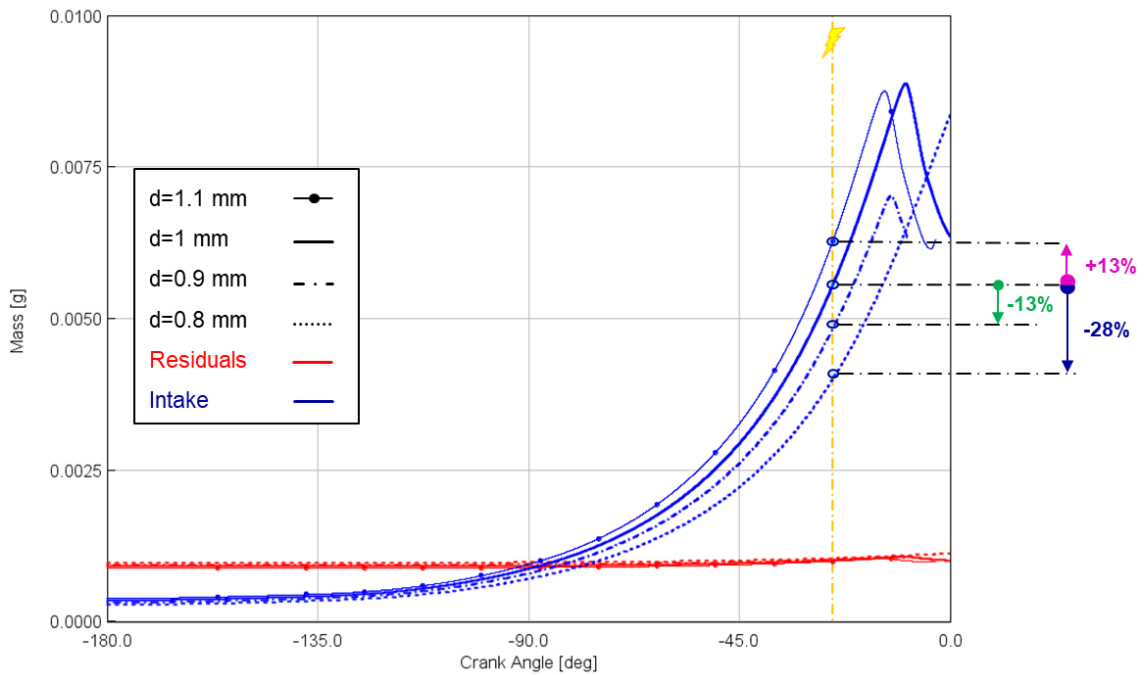


Figure 50: Holes Diameter Sweep – PC Residuals and Intake Mass

Indeed, the mass flow rate from main chamber to pre-chamber during the compression stroke, which is mainly made of unburnt species, increases for larger diameters, as the area across which the fluid is flowing becomes larger and larger. Table 21 shows the numerical values describing the performance in terms of scavenging for the four analyzed designs

| Case     | Residuals Mass @ ST<br>[kg] | Intake Mass @ ST<br>[kg] | Residuals % (PC avg.) @ST<br>[%] | Residuals % around SP @ ST<br>[%] |
|----------|-----------------------------|--------------------------|----------------------------------|-----------------------------------|
| d=1.1 mm | 0.99e-06                    | 6.28e-06                 | 13.7%                            | 28.8%                             |
| d=1 mm   | 1.01e-06                    | 5.56e-06                 | 15.4%                            | 34.3%                             |
| d=0.9 mm | 1.02e-06                    | 4.84e-06                 | 17.5%                            | 28.8%                             |
| d=0.8 mm | 1.04e-06                    | 4.01e-06                 | 20.7%                            | 42.8%                             |

Table 21: Holes Diameter Sweep – PC Scavenging

It is also interesting to mention that smaller holes lead to faster velocities of the incoming fresh flow in the pre-chamber, up to the point of reaching a choked flow condition during the scavenging process for the smaller holes cases (d=0.8 mm and d=0.9 mm); larger holes (d=1 mm and d=1.1 mm) show no flow choking, while having the highest mass flow rates. Figure 51 illustrates such observation reporting the Mach number averaged for the four holes along the mass flow rate from cylinder to pre-chamber.

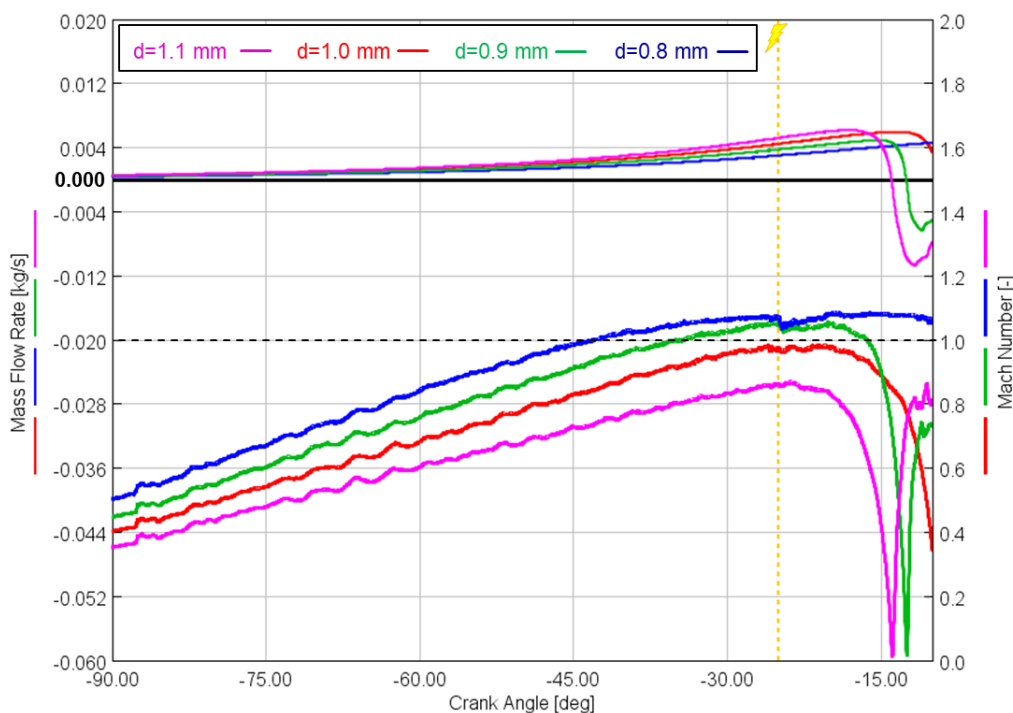


Figure 51: Holes Diameter Sweep – Mach Number through PC Holes

The analysis of Table 21 confirmed the expected trend of lower residuals presence in the pre-chamber for larger diameter holes. However, looking at the column describing the residuals concentration around spark plug a small anomaly arises, having the case with a diameter equal to 0.9 mm with the same value as the case with the largest hole (d=1.1 mm). This offers the opportunity to discuss the residuals distribution in the PC and explore possible secondary effects coming from the change in diameter size.

Figure 52 illustrates the distribution of residuals at ST both across the pre-chamber and across the spark plug with two different scale levels, in order to better highlight the differences around SP. The top part of the pre-chamber is the area the largest amount of residuals. The two views are effective in capturing the better scavenging behavior for the larger holes, especially at spark plug, where the more refined scale allows to highlight that a larger hole is more effective in cleaning even the upper crown of the pre-chamber, which was the area with the highest residuals concentration.

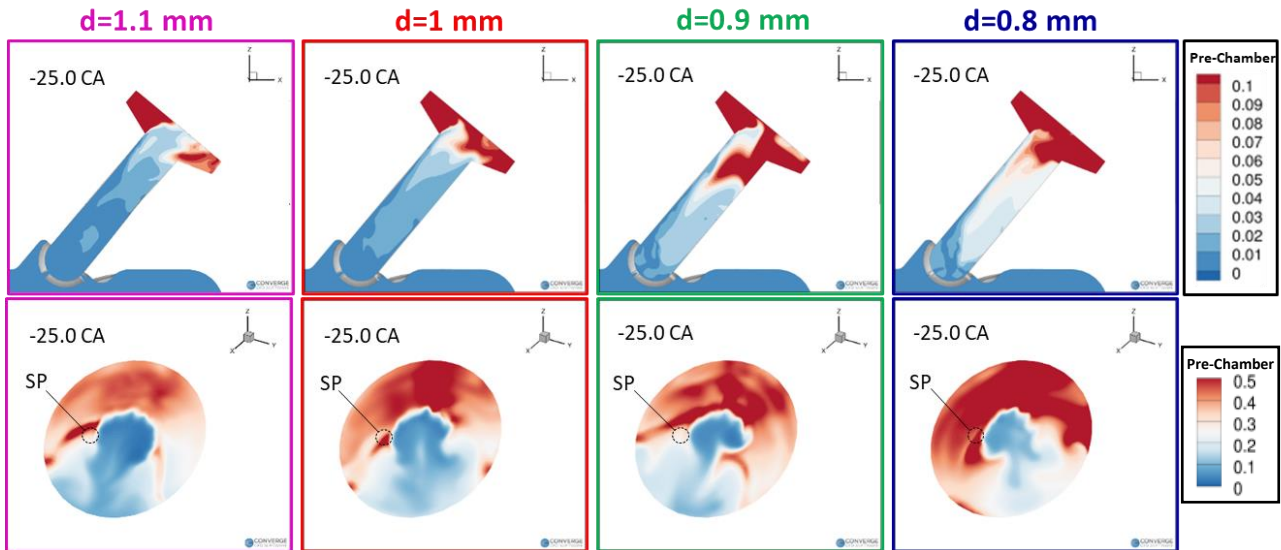


Figure 52: Holes Diameter Sweep – PC Residuals Distribution

Although a general trend previously experienced in the literature was observed, the case with  $d=0.9$  mm yields particular results in terms of residuals presence around spark plug. The lower row of Figure 52 helps in understanding such behavior. In fact, the fresh charge area below the spark plug, which for smaller holes seems to become smaller and smaller, in this particular case is relatively large, or at least comparable with the one of the case at largest hole design. Most likely, the higher intake flow velocity of this case makes the incoming air/fuel mix arrives at spark plug more vigorously, thus being able to “free” the lower part of the PC crown more effectively. The same cannot be said about the smallest hole design, where there is not enough intake mass transport to lower the residuals concentration.

Finally, Figure 53 is presented showing a sensitivity to hole diameter of PC residuals concentration; at the same time, to underline the root cause of different concentrations, also intake and residuals mass sensitivity is reported. It can be seen how the dependence of residuals concentration on hole diameter is non-linear and with a decreasing trend for increasing diameter. This evidence is in agreement with observations made on other simulations performed at 3000 rpm, both in lean and stoichiometric conditions.

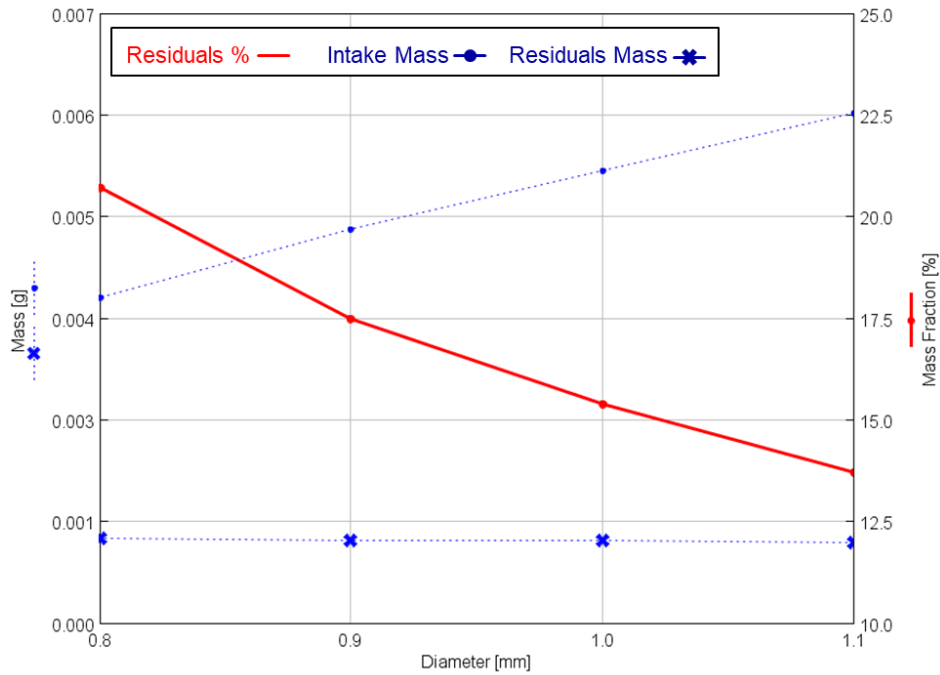


Figure 53: Holes Diameter Sensitivity – PC Scavenging

### 3.2.2 Pre-Chamber Turbulent Kinetic Energy

Just like for residuals analysis, hole diameter is expected to be a major parameter in the definition of Turbulent Kinetic Energy levels in the pre-chamber, as it defines the restriction that the fluid will have to flow through.

Figure 54 represents the profile PC average TKE and TKE at spark plug monitor point.

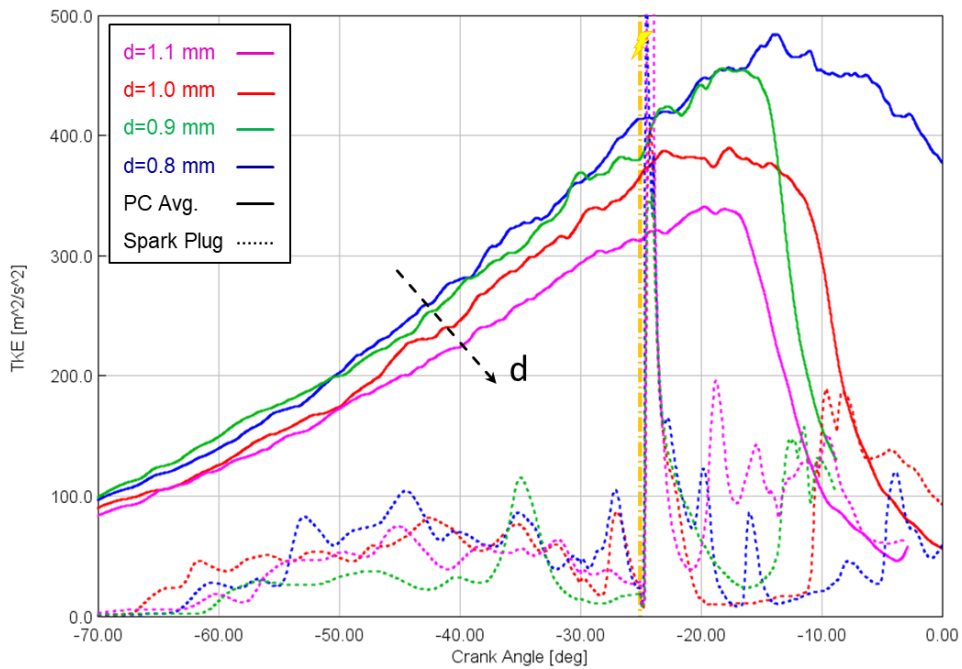


Figure 54: Holes Diameter Sweep – TKE (PC Avg. and Spark Plug)

The ability of the holes to disrupt the flow field in the pre-chamber increases as the diameter decreases due to the greater restriction seen by the flow. Thus, smaller holes allow to obtain a higher level of Turbulent Kinetic Energy inside the pre-chamber. Table 22 summarizes the numerical values of the TKE levels obtained throughout the diameter sweep.

| Case     | TKE (PC avg.) @ ST<br>[m <sup>2</sup> /s <sup>2</sup> ] | TKE around SP @ ST<br>[m <sup>2</sup> /s <sup>2</sup> ] |
|----------|---|---|
| d=1.1 mm | 312.1   | 75.3  |
| d=1 mm   | 366.5   | 66.6  |
| d=0.9 mm | 381.0   | 66.8  |
| d=0.8 mm | 413.7   | 81.8  |

Table 22: Holes Diameter Sweep – Pre-Chamber TKE

The values of TKE around spark plug is in accordance with the trend observed for the pre-chamber average, except for the case of a diameter size of 1.1 mm, which shows a relatively high value. The root cause for such behavior was assumed to be the ability of such hole size to create a turbulent flow and being able to transport with its higher mass flow rate such turbulence to the spark plug in an effective way.

The sequence of illustrations in Figure 55 underlines that the qualitative distribution of TKE across the pre-chamber is not changing, differently from its intensity. The upper part of the central region of the pre-chamber, is once again the most turbulent one; at the same time, the area below the spark plug appears as more turbulent than the rest of the PC crown.

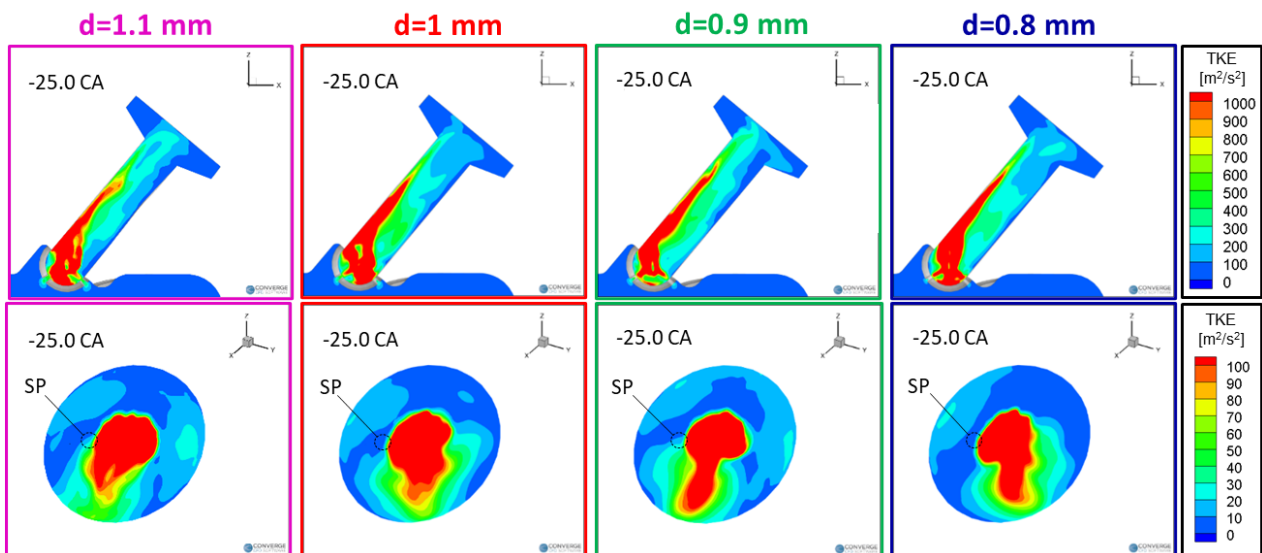


Figure 55: Holes Diameter Sweep – PC TKE Distribution

A graph summarizing the sensitivity analysis of TKE, as PC average, to hole diameter size is presented in Figure 56. The relationship between these two parameters appears as non-linear: decreasing the hole diameter has been proven to increase the TKE by increasing the flow restriction

while increasing the flow speed entering the PC, as seen in the previous section from the Mach Number analysis. The TKE levels at spark plug are coming from the combination of two contrasting effects: the flow resistance imposed by a lower diameter and the ease with which the turbulent flow is able to reach the spark plug, which is higher for larger holes.

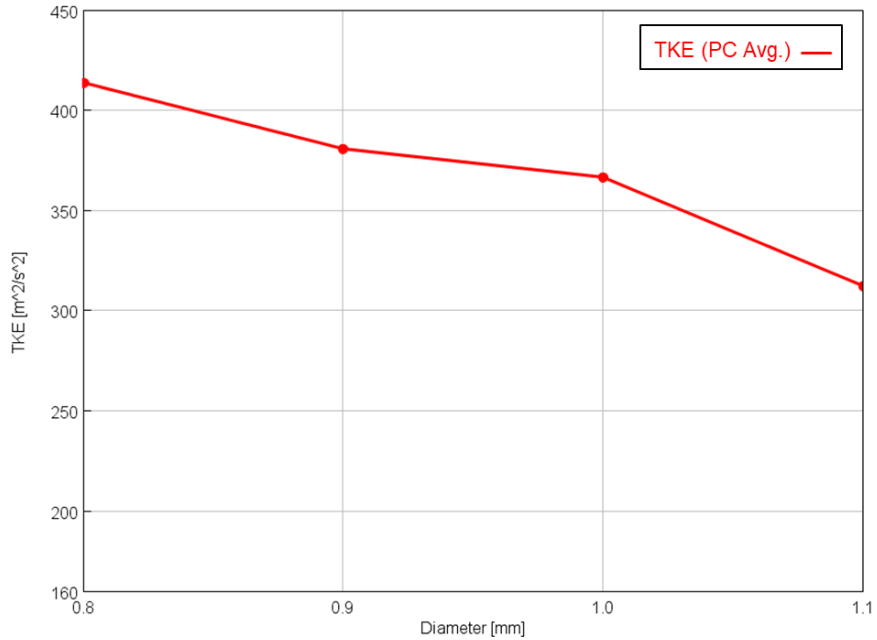


Figure 56: Holes Diameter Sensitivity – PC TKE

### 3.2.3 Pre-Chamber Combustion

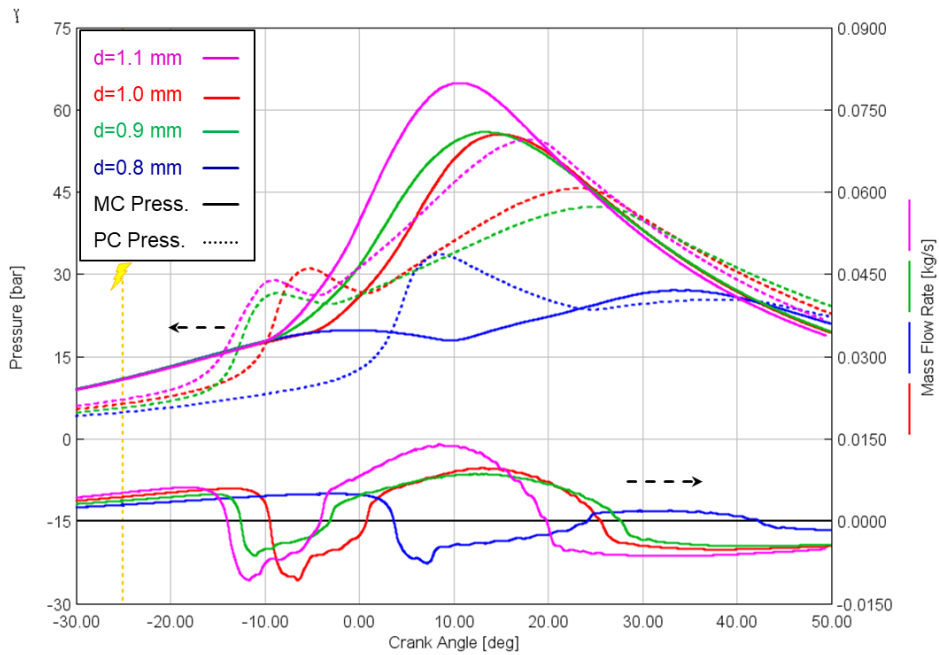


Figure 57: Holes Diameter Sweep – PC and MC Pressure

Figure 57 illustrates the results in terms of pressure rise in main chamber and pre-chamber, as well as the resulting mass flow rate from MC to PC.

As it appears, the case at hole diameter 1.1 mm yields the earliest pressure rise in the pre-chamber, as an outcome of its favorable conditions in terms of low residuals concentration and sufficiently high Turbulent Kinetic Energy. The 0.9 mm design also shows a combustion process faster than the baseline case; as seen, this hole size combines optimal conditions at spark to optimal conditions in the rest of the PC.

The most peculiar case, by far, is the one with the smallest diameter ( $d=0.8$  mm): as a matter of fact, this layout almost led to a misfiring cycle and it is only able to establish a real combustion development in the pre-chamber with a delay of 10-15 crank-angle degrees with respect to the remaining cases. This fact is certainly linked to the higher residuals concentration, although the main cause is most likely the very high TKE level around spark plug, which keeps the initial kernel from developing in a regular way.

The discussed trends are translated also in terms of initial pressure difference between main chamber and pre-chamber and, thus, in terms of jet injection mass flow rate. It is interesting to notice that the layout at 0.9 mm, despite starting its pressure rise relatively early, does not show a very large mass flow rate during the jet injection phase; this is probably due to the combination of lower pressure conditions in the pre-chamber and start of combustion in the main chamber, which appears as slightly anticipated with respect to the other cases. These two facts diminish the MC-PC pressure differential, hence limiting the maximum mass flow rate.

Finally, the pressure traces in the main chamber seem to be in accordance with the start of pressure rises in the pre-chamber and, thus, start of jet injection, proving how MC combustion timing is still a fundamental factor in the context of engine cycle performance.

### 3.2.4 Jet Injection

A comparison on the impact of hole diameter on the jet injection phase is now carried out, following the blueprint set by [27], in which it is stated that smaller holes should lead to faster, more penetrative jets, while larger holes should give a faster delivery of energy content via larger jets.

Figure 58 illustrates the jet injection phase by the trace of mass flow rate from cylinder to pre-chamber. Furthermore, the Mach number (as average value of the four layouts) is presented.

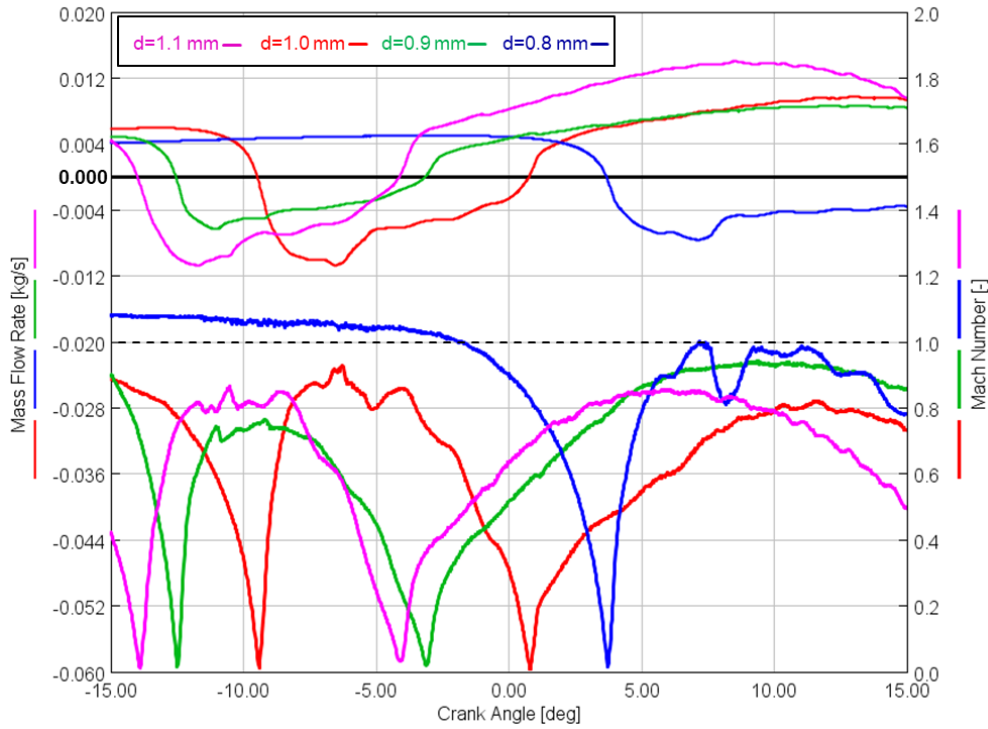


Figure 58: Holes Diameter Sweep – MC/PC Mass Flow Rate and Mach Number

Along with Figure 58, Table 23 is also presented, analyzing the jet injection phase by means of peak mass flow rate and injection duration.

| Case     | Injection Duration<br>[deg] | Peak Mass Flow Rate<br>[kg/s] |
|----------|-----------------------------|-------------------------------|
| d=1.1 mm | ~10°                        | 10.7e-03                      |
| d=1 mm   | ~10.3°                      | 10.7e-03                      |
| d=0.9 mm | ~9°                         | 6.3e-03                       |
| d=0.8 mm | ~23.5°                      | 7.4e-03                       |

Table 23: Holes Diameter Sweep – Jet Injection

As it appears, the effects of having a smaller hole diameter are in fact to obtain a longer injection phase with faster exiting jets, as observable from Mach number and confirmed by velocity trends (not presented here for brevity). This trend is not respected only by the layout with diameter equal to 0.9 mm, which represents a sort of anomaly in this context. It is possible that this fact is the outcome of two causes. First, it must be highlighted that the initial pressure in the pre-chamber becomes lower

and lower as the diameter decreases: this is due to the increased pressure drop between MC and PC caused by the higher flow restriction. This fact, in turns, will lead to a lower pressure difference when the pre-chamber combustion process reaches its peak, leading ultimately to a lower flow rate. Secondly, the combustion process in the cylinder seems to start slightly earlier for this case, as it can be noticed by the fact that, despite having a different PC combustion timing, case  $d=0.9$  mm and  $d=1.1$  mm have more or less the same start of pressure rise in MC; this fact, in turns, leads to a lower injection duration.

A further investigation was carried out on the base of [32], where the jet injection phase is described as made up of three different steps: a first one characterized by the ejection of cold unburnt mixture; a second step, after the combustion process in the pre-chamber has successfully developed, characterized by the discharge of hot jets full of intermediate products. Finally, the rich part of the mixture, which was confined in the top part of the pre-chamber, is ejected. To perform such analysis, the trends of average temperature at hole outlet, intermediate products mass fraction and mass flow rate, both total and for fuel, were extrapolated. Intermediate products were calculated as unity minus the mass fraction sum of air,  $\text{CO}_2$ ,  $\text{H}_2\text{O}$ , fuel species in cylinder. It is important to highlight that this definition is different from the one given in [32], purely due to lack of output data from the simulation. Furthermore, it is underlined that, since the concentration of intermediate products is taken inside the cylinder, it is only meaningful during the first part of the injection phase, as later on the start of MC combustion would alter said parameter, adding a source not related to the jets themselves. Nevertheless, such quantity is quite useful in the description of jet discharge.

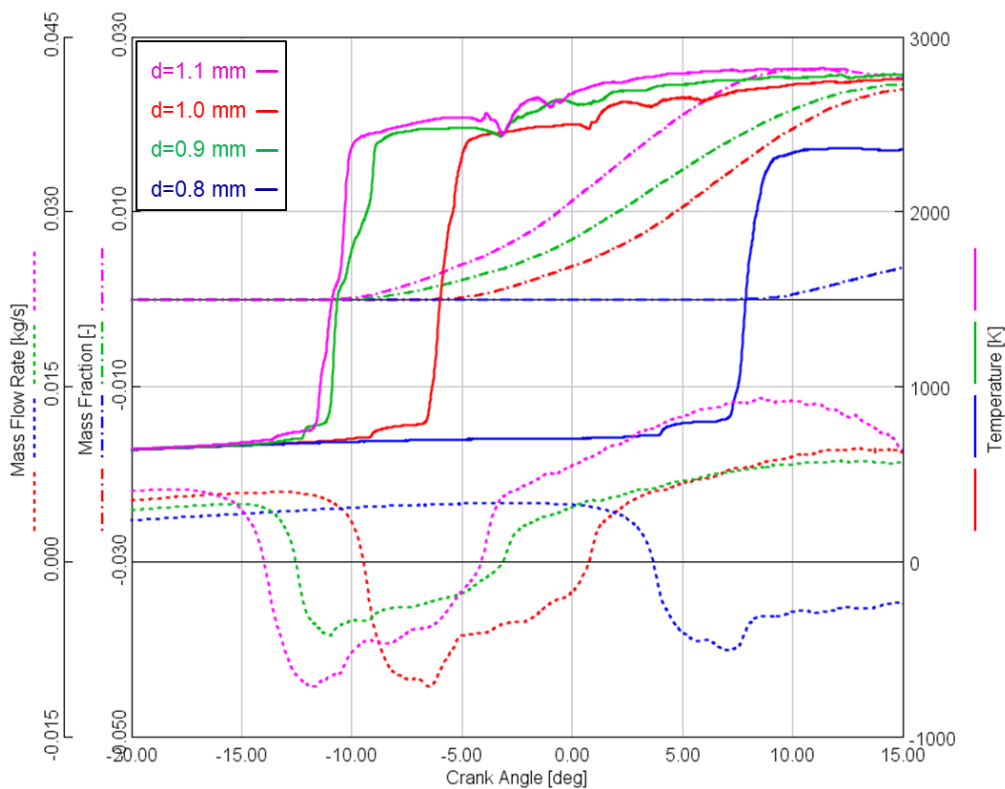


Figure 59: Holes Diameter Sweep – Jet Injection Characterization

Figure 59 represents the trends of the aforementioned quantities. The first fact to be noted is the absence of the third phase (discharge of fuel rich mixture); this is likely a consequence of the pre-

chamber operation mode. As a matter of fact, unlike in the present study, the pre-chamber employed in [32] is used in active mode, thus allowing the enrichment of the PC mixture at will. Nevertheless, the durations of the first two phases are reported in Table 24, from which a sensitivity graph was also obtained (Figure 60).

| Case     | Phase 1 Duration [deg] | Phase 2 Duration [deg] |
|----------|------------------------|------------------------|
| d=1.1 mm | ~3.0°                  | ~5.0°                  |
| d=1 mm   | ~2.7°                  | ~6.2°                  |
| d=0.9 mm | ~2.2°                  | ~7.5°                  |
| d=0.8 mm | ~3.4°                  | ~18.0°                 |

Table 24: Holes Diameter Sweep – Jet Injection Phases

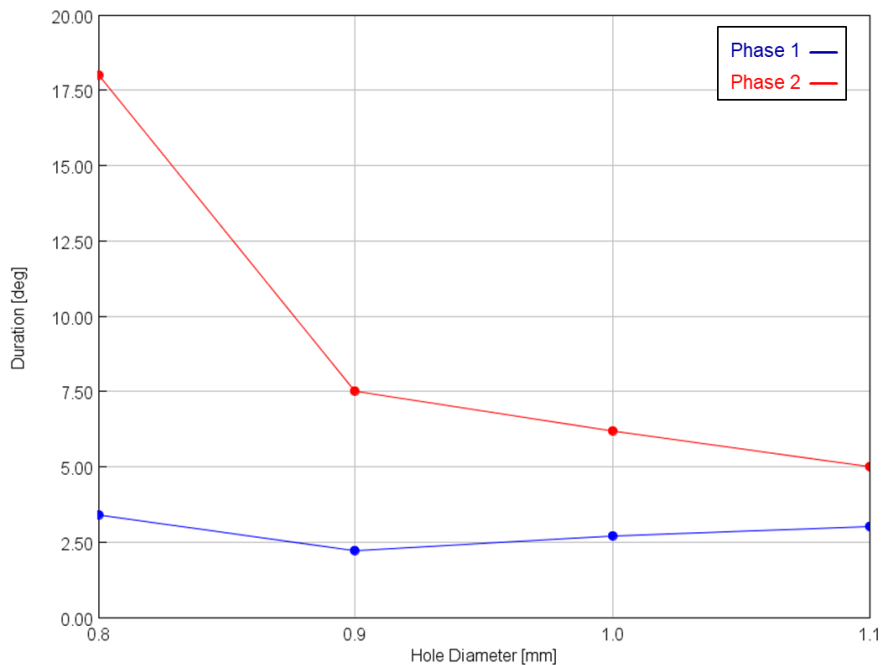


Figure 60: Holes Diameter Sensitivity – Jet Injection Phases

It is interesting to notice that the first phase seems to be basically insensitive to hole diameter variation, while the second phase shows a linear trend.

The reason for such behaviors was hypothesized as being the Heat Release Rate trend in the pre-chamber, which dictates the pressure difference between MC and PC and, thus, the flow exchange process in all its phases. In this framework, by overlapping the traces of HRR for the different layouts without considering PC combustion timing, as in Figure 61, it can be seen that the earliest behavior looks quite similar. Afterwards, the traces begin to differ. This could explain the similarities found in the first phase and differences in the second phase of the jet discharge process.

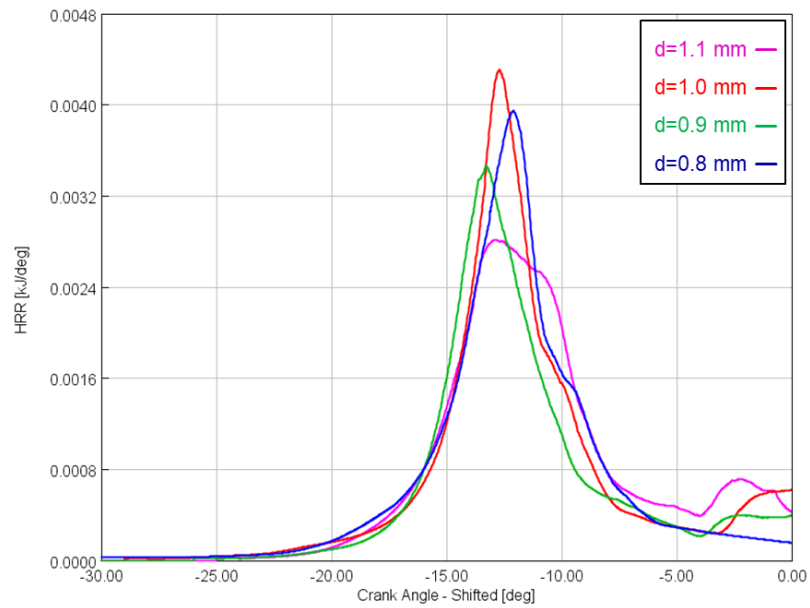


Figure 61: Holes Diameter Sweep – PC HRR (Shifted Profiles)

### 3.2.5 Flow Reversal

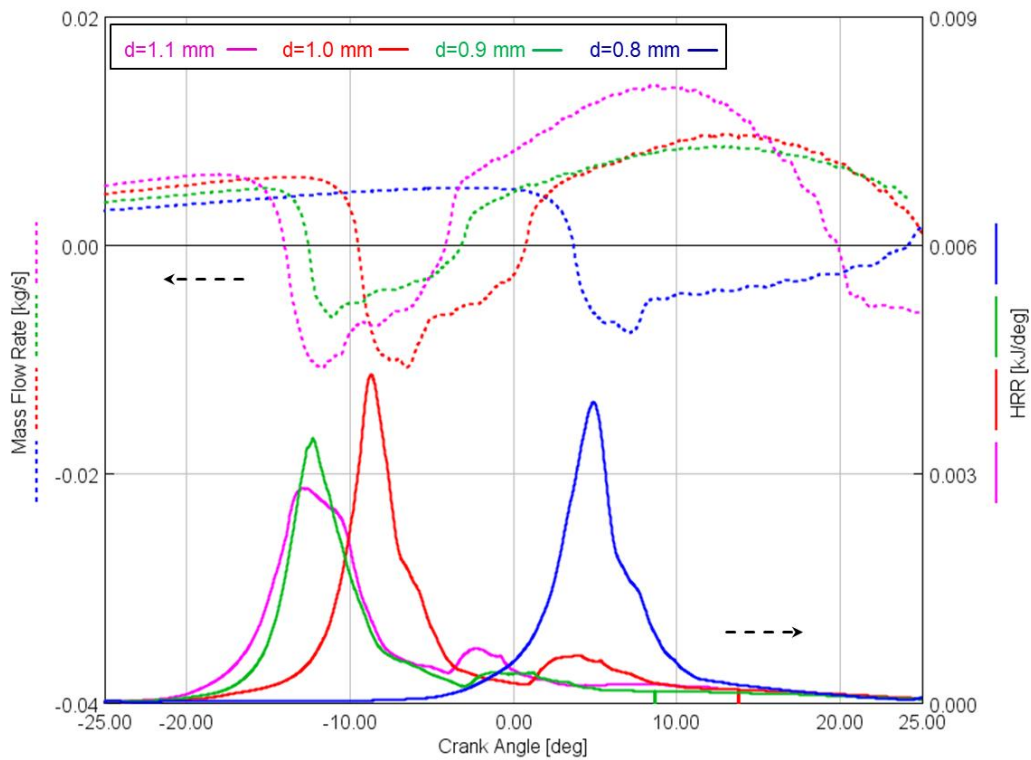


Figure 62: Holes Diameter Sweep – MC/PC Mass Flow Rate and PC HRR

The flow reversal phase is analyzed. Figure 62 reports the mass flow rate and HRR trends in the pre-chamber. The flow reversal phase, as said, can be identified as the moment where the flow reverses back from the cylinder to pre-chamber, where a second HRR peak occurs. Although not fully perceivable from the graph, it is noted that the design with hole diameter equal to 0.8 mm shows little

to no sign of a flow reversal phase. Table 25 reports the numerical values describing the flow reversal phase in terms of peak flow rate and peak HRR; a sensitivity graph (Figure 63) is obtained from it.

| Case     | Peak HRR<br>[kJ/deg] | Peak Mass Flow Rate<br>[kg/s] |
|----------|----------------------|-------------------------------|
| d=1.1 mm | 7.1e-04              | 14.0e-03                      |
| d=1 mm   | 6.2e-04              | 9.7e-03                       |
| d=0.9 mm | 4.0e-04              | 8.6e-03                       |
| d=0.8 mm | -                    | -                             |

Table 25: Holes Diameter Sweep – Flow Reversal

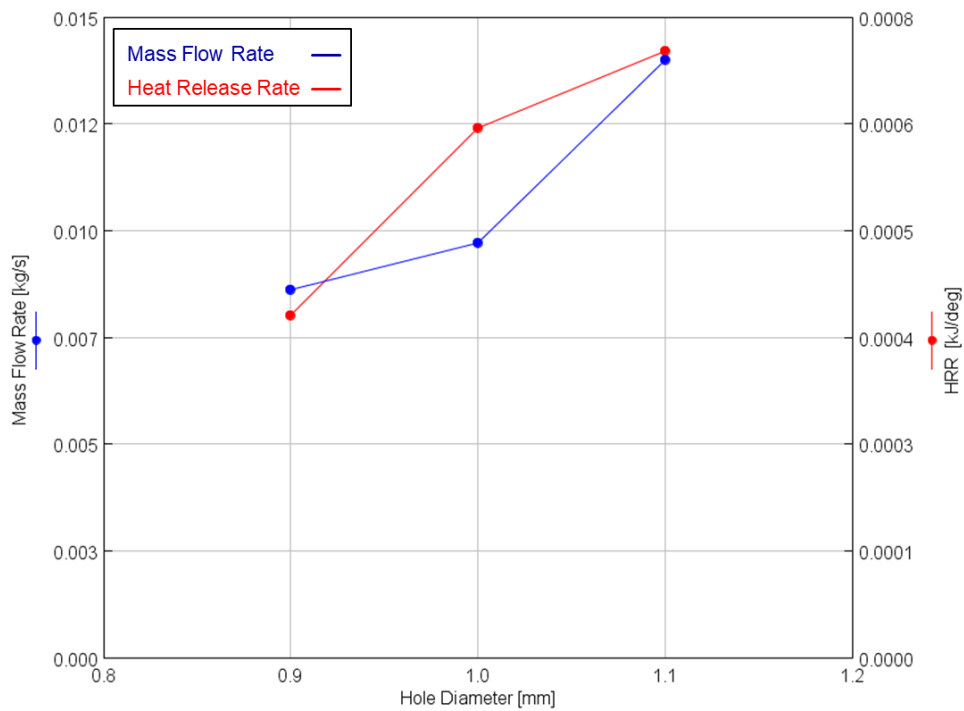


Figure 63: Holes Diameter Sensitivity – Flow Reversal (Peak MFR and Peak HRR)

### 3.2.3 Pre-Chamber Holes Rotation – 4000 rpm

In the framework of a geometry optimization, a new pre-chamber design was tested, with the four holes rotated of 45° with respect to the baseline configuration, as illustrated in Figure 64.

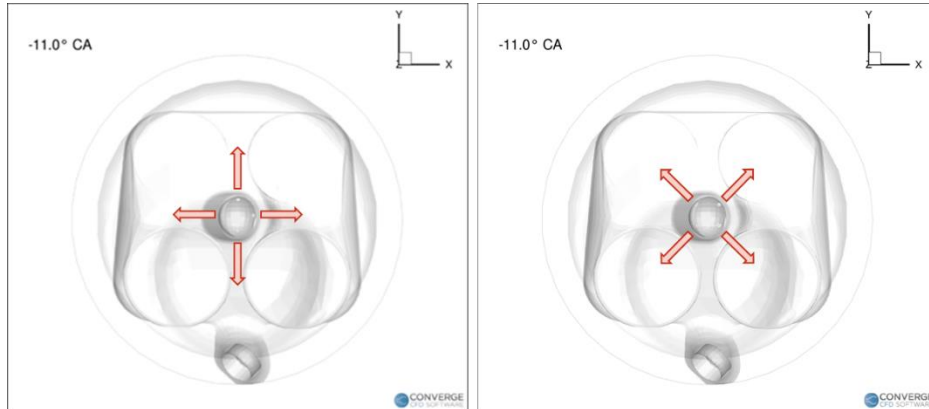


Figure 64: Pre-Chamber Holes Orientation - Baseline (left) VS Rotated (right)

#### 3.2.3.1 Pressure and HRR Results

The results in terms of pressure and HRR are reported in Figure 65.

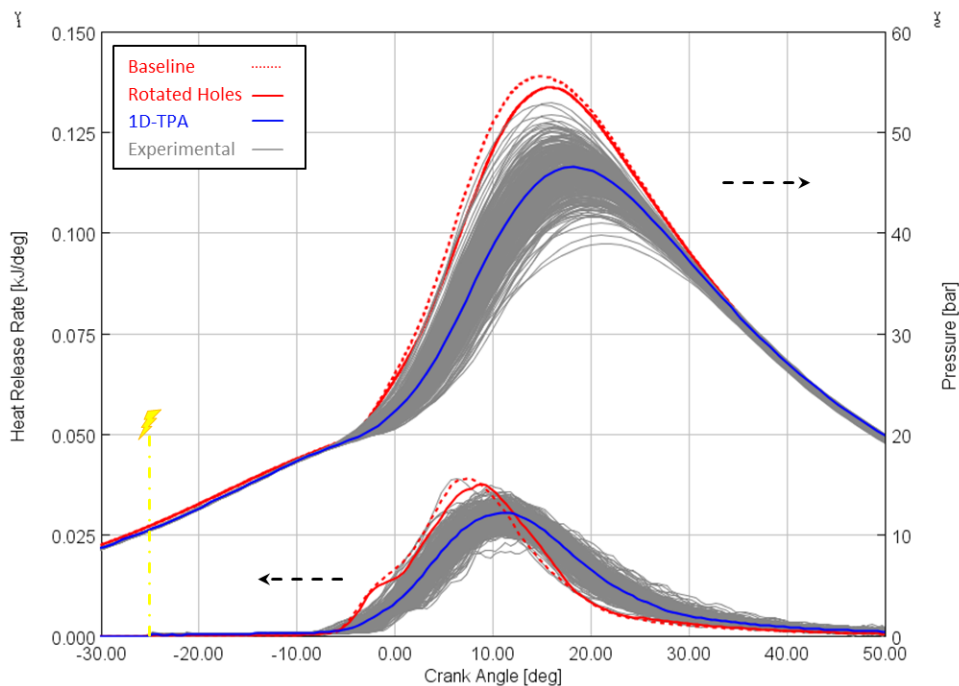


Figure 65: 4000 rpm x  $\lambda=1$  Holes Rotation – Pressure and HRR Profiles

As previously done, an analysis of engine performance is carried out in the following sections.

### 3.2.3.2 Pre-Chamber Scavenging

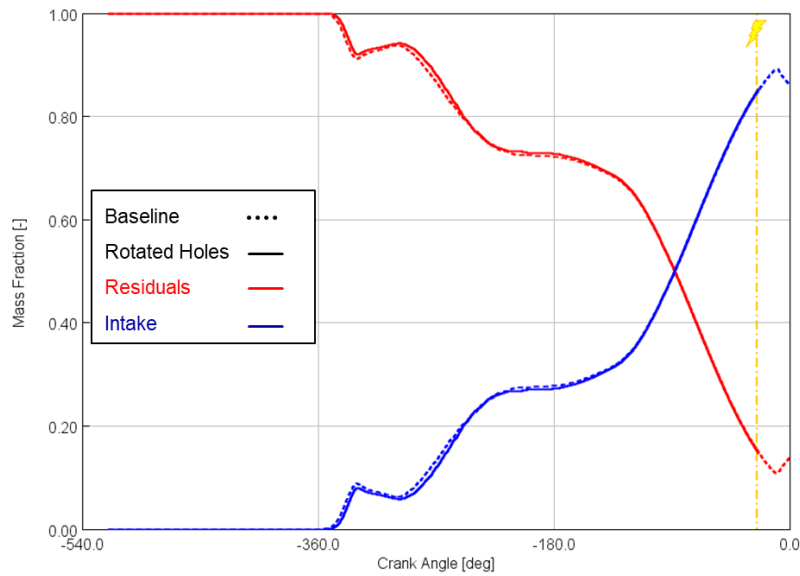


Figure 66: 4000 rpm x  $\lambda=1$  Holes Rotation – PC Residuals and Intake Concentration

Figure 66 highlights the trends in residuals and intake mass concentrations inside the pre-chamber at spark timing. It appears as evident how the rotation of the PC holes leads to practically no difference in the investigated quantities inside the pre-chamber. As proved previously, the main cause for any difference in residuals concentration is the amount of fresh mass pushed inside the pre-chamber during the compression stroke. To confirm once again such expectation, Figure 67 is reported.

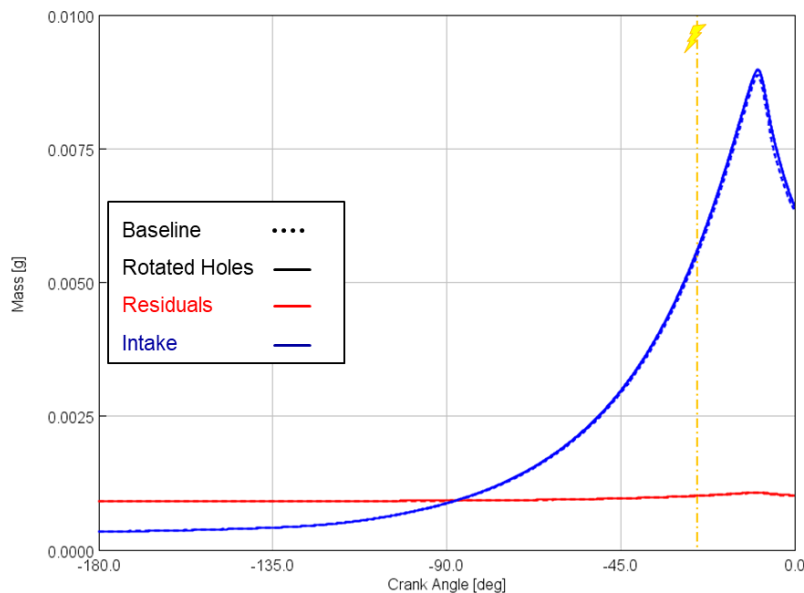


Figure 67: 4000 rpm x  $\lambda=1$  Holes Rotation – PC Residuals and Intake Mass

On the basis of the discussed results, it is reasonable to assess that the rotation of the pre-chamber holes has no impact on the overall scavenging of the pre-chamber, with average values of residuals concentration practically equal one to another.

Instead, residuals concentrations around spark plug seem to be altered by the change in geometry, as noticeable from the region with lower residuals in the bottom part of the SP cross section, lower row

of Figure 68, which is appearing as rotated. This is in agreement with the holes rotation and, certainly, the different flow pattern created by it. In particular, the conditions around SP are improved by the holes rotation, creating a lower concentrations of Residuals, with a decrease of almost 9%. The values for residuals concentration on PC average and around spark plug are reported in Table 26.

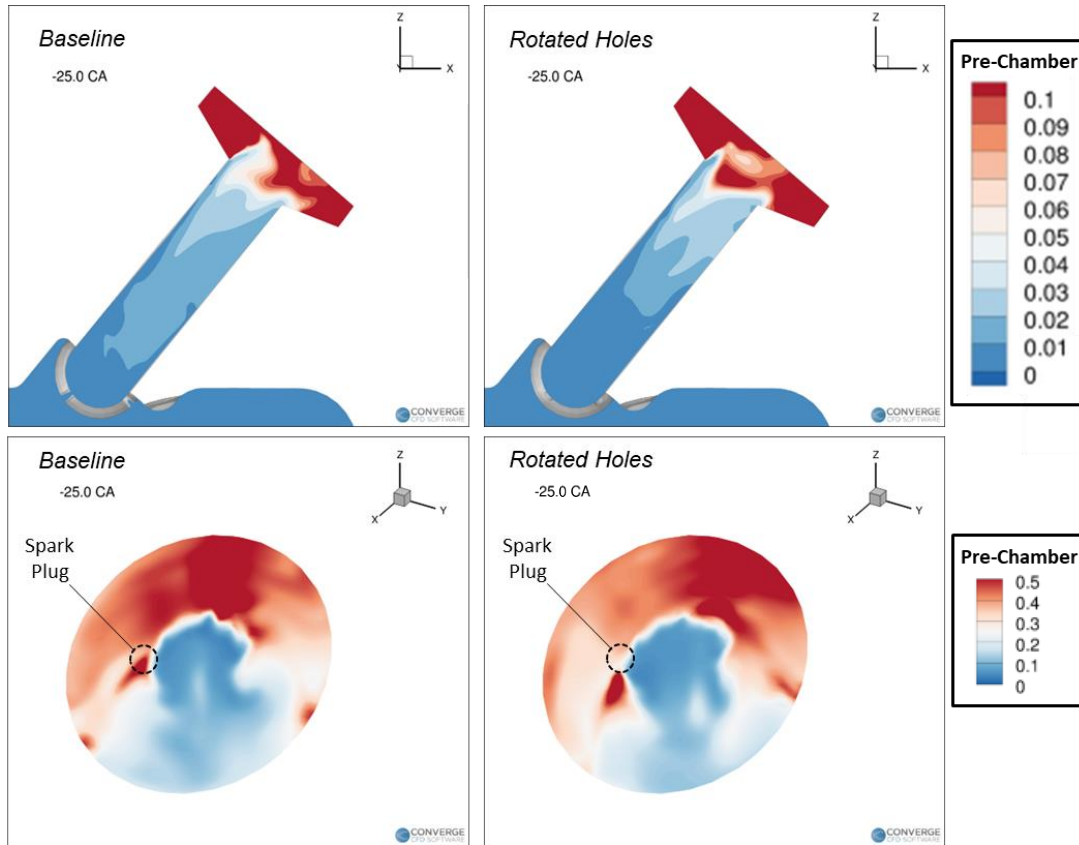


Figure 68: PC Residuals Distribution – Baseline (left) VS Rotated Holes (right)

| Case               | Holes Rotation<br>[deg] | Residuals % (PC avg.)<br>@ST<br>[%] | Residuals % around<br>SP @ ST<br>[%] |
|--------------------|-------------------------|-------------------------------------|--------------------------------------|
| 4000 x $\lambda=1$ | -                       | 15.4%                               | 34.3%                                |
|                    | 45                      | 15.2%                               | 25.9%                                |

Table 26: PC Holes Rotation – PC Scavenging

### 3.2.3.3 Pre-Chamber Turbulent Kinetic Energy

TKE levels inside the pre-chamber are expected to vary significantly with respect to the baseline configuration. In fact, when analyzing starting case, one of the main features of the system was proved to be the TKE distribution obtained thanks to one hole directly aligned with the PC axis.

To confirm this expectation, Figure 69 highlights that the effect of rotating the pre-chamber holes appears as to decrease the overall level of Turbulent Kinetic Energy inside the PC.

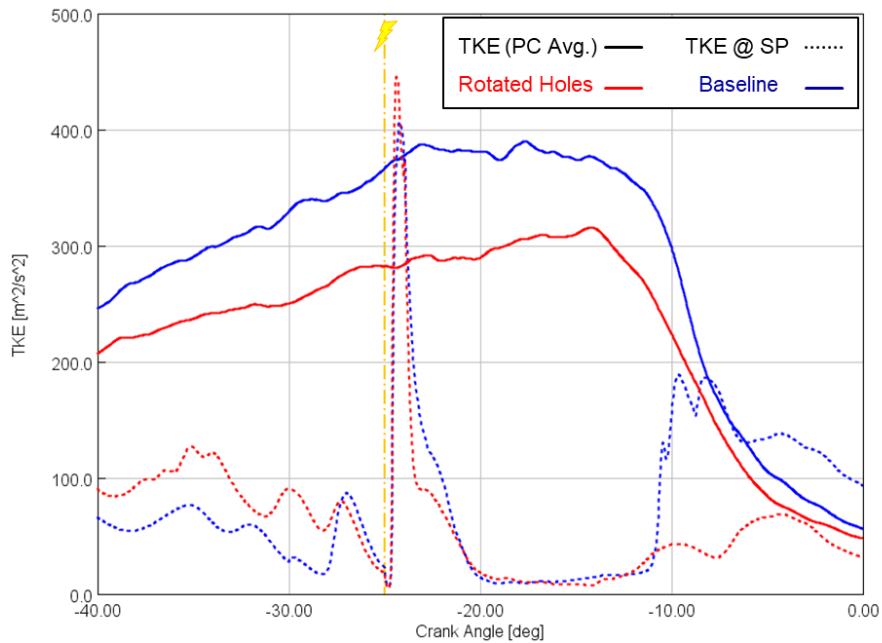


Figure 69: 4000 rpm x  $\lambda=1$  Holes Rotation – PC TKE

Moreover, the distribution of TKE is heavily affected by the new geometry layout, once again due to the different flow pattern created inside the pre-chamber by the rotated holes (Figure 70).

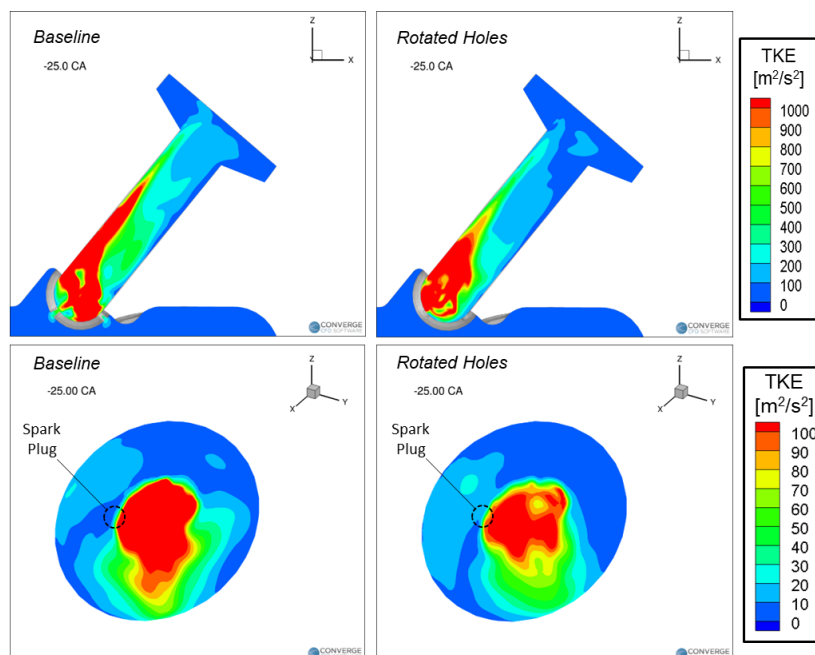


Figure 70: PC TKE Distribution – Baseline (left) VS Rotated Holes (right)

As already assessed, the baseline case features a very turbulent path in the upper part of the PC body. The rotated holes configuration, instead, shows a high turbulence area concentrated in the bottom part of the pre-chamber. Considerable, yet lower, levels of TKE are still found in the upper PC, mainly due to the tilted positioning of the pre-chamber itself.

The distribution of TKE around the spark-plug seems to follow the considerations made for the concentration of residuals, with a trace that looks rotated, just like the holes, around the PC axis. Nevertheless, this results in driving away turbulence from the SP location, with a decrease in its value.

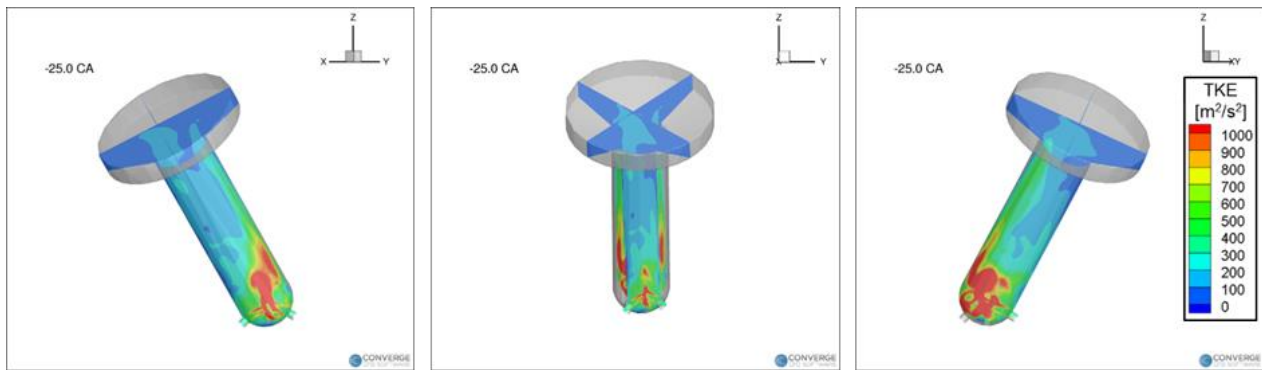


Figure 71: 4000 rpm x  $\lambda=1$  Holes Rotation – PC TKE on Holes Cross-Sections

To further investigate the qualitative characteristics dictated by the new geometry design, two additional sections, cutting through the rotated holes, were considered as in Figure 71. These allow to underline a somewhat symmetric and more homogeneous distribution of TKE inside the pre-chamber, differently from the baseline layout.

Finally, Table 27 summarizes the TKE levels in the pre-chamber, both on average and around SP.

| Case               | Holes Rotation [deg] | TKE (PC avg.) @ ST [m <sup>2</sup> /s <sup>2</sup> ] | TKE around SP @ ST [m <sup>2</sup> /s <sup>2</sup> ] |
|--------------------|----------------------|--|--|
| 4000 x $\lambda=1$ | -                    | 366.5  | 66.6   |
|                    | 45                   | 282.3  | 56.4   |

Table 27: PC Holes Rotation – PC Turbulent Kinetic Energy

### 3.2.3.4 Pre-Chamber Heat Release Rate and Jet Injection

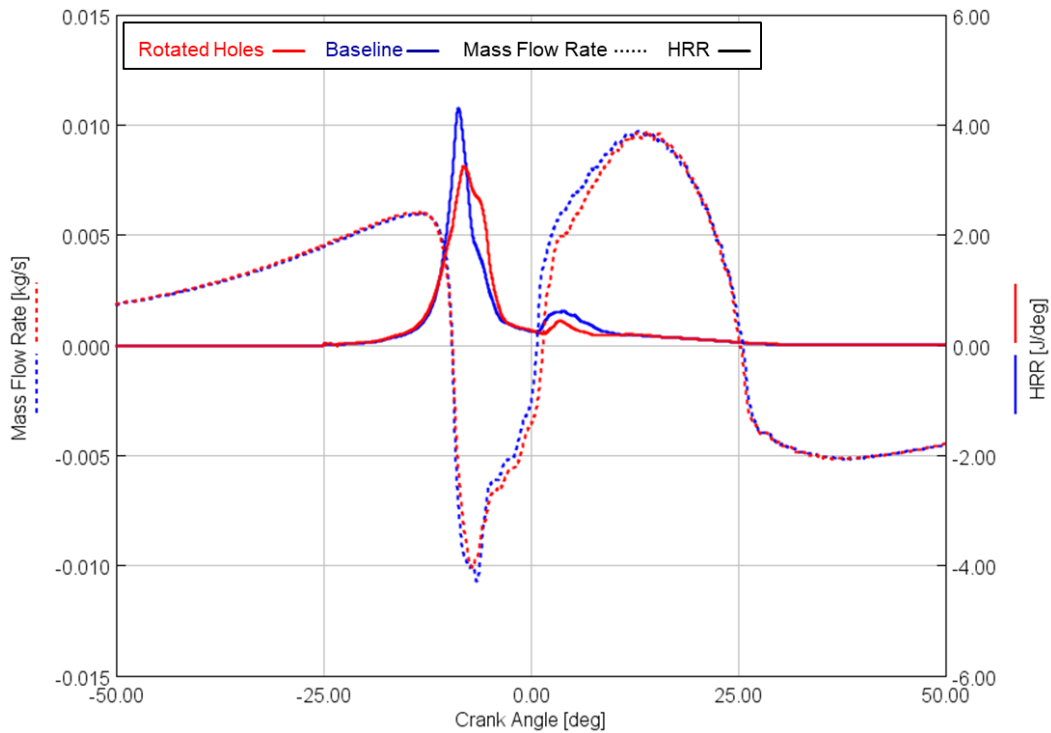


Figure 72: 4000 rpm  $\lambda=1$  Holes Rotation – PC HRR and MC/PC Mass Flow Rate

Figure 72 shows the trace of Heat Release Rate inside the pre-chamber and mass flow rate from cylinder to PC. Results show that the combination of lower residuals concentration around spark plug is evened out by the lower levels of TKE set across the whole pre-chamber. This results in a marginal difference in HRR inside the PC, with a lower peak for the rotated holes design. Being the residuals concentration practically the same in the two cases, it is reasonable to assume that such difference is due to the lower TKE found in the pre-chamber. Nevertheless, the jet injection event seems to be almost unaffected in terms of timing, duration and intensity.

What is left to be addressed is the effect of the change in geometry in jet exit distribution. Figure 73 shows a comparison between the baseline and new design engine setup when the jets exit the pre-chamber. It can be observed how the first jets entering the main chamber are now the ones coming from the holes located next to the exhaust valves.

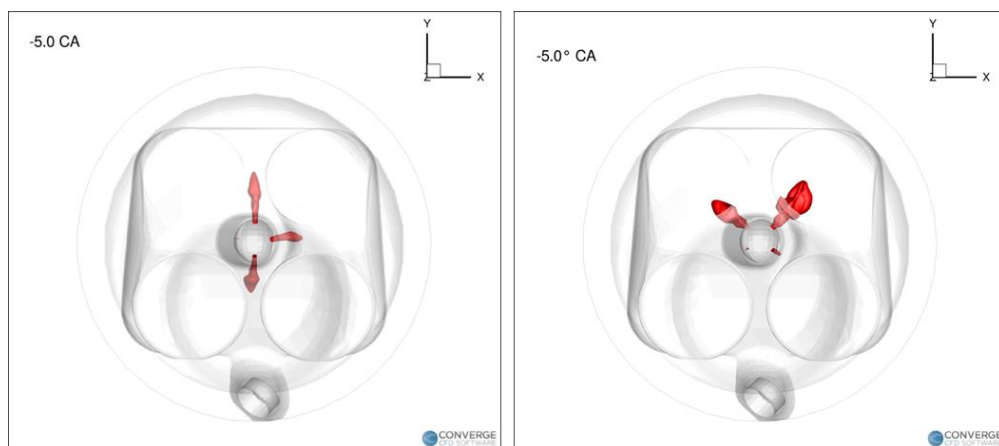


Figure 73: Jet Exit – Baseline (left) VS Rotated Holes (right)

The cause for this different behavior can be found considering the conditions at spark timing previously discussed. Figure 74 provides a view of residuals distribution at ST and temperature isosurface when the flame enters the pre-chamber body. The flame prefers the area with low residuals concentration, which appears to be on the exhaust valves side (on the right); from that point, it is useful to remind how the TKE distribution inside the PC looked pretty symmetrical in the rotated hole case, hence leaving the flame front with no preferred path. It can be stated, finally, that the initial disparity in flame front location is kept up until hole exit.

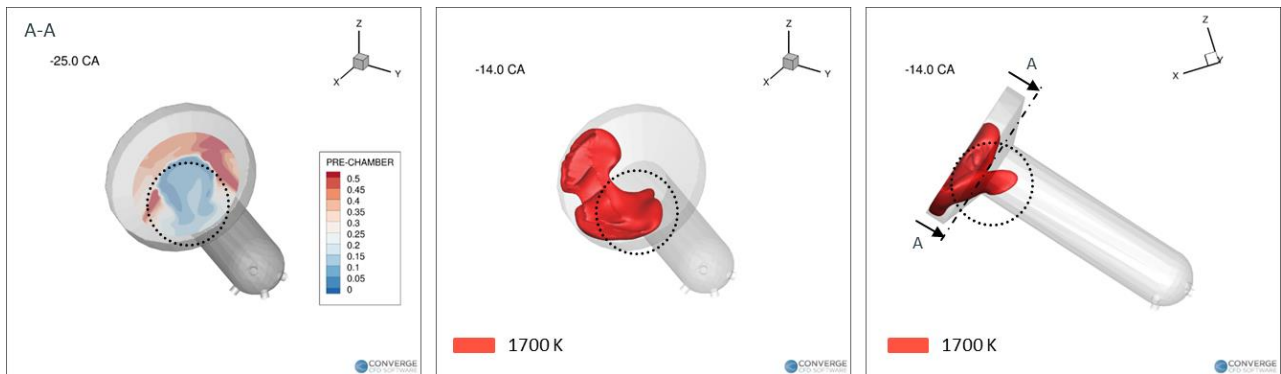


Figure 74: 4000 rpm  $\times \lambda=1$  Holes Rotation – Residuals Distribution and Early Flame Development

### 3.2.3.5 Exhaust Valves Interaction

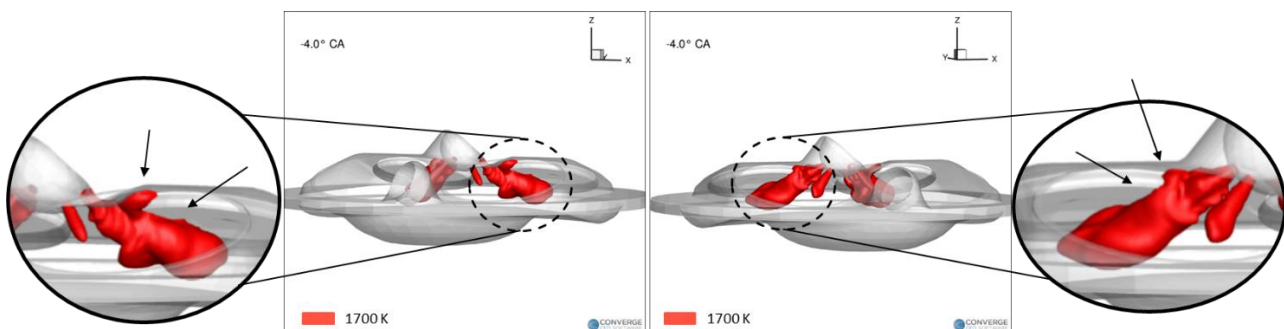


Figure 75: 4000 rpm  $\times \lambda=1$  Holes Rotation – Turbulent Jet Impact

Up to this point of the hole rotation analysis, little to no consideration has been given to the events happening in the main chamber. Analyzing the temperature isosurface inside the cylinder for the rotated holes design (Figure 75), it was observed how the flame exiting the PC holes interacts with the exhaust valves. This was thought to be the reason behind the loss of Heat Release Rate in the main chamber, as highlighted in Figure 76 by the lower HRR slope and peak.

The analysis of this phenomenon was performed based on the blueprint of [13], which explains how, for passive pre-chambers, ignition by means of a turbulent jet is initiated by 2 effects: thermal effect and chemical effect.

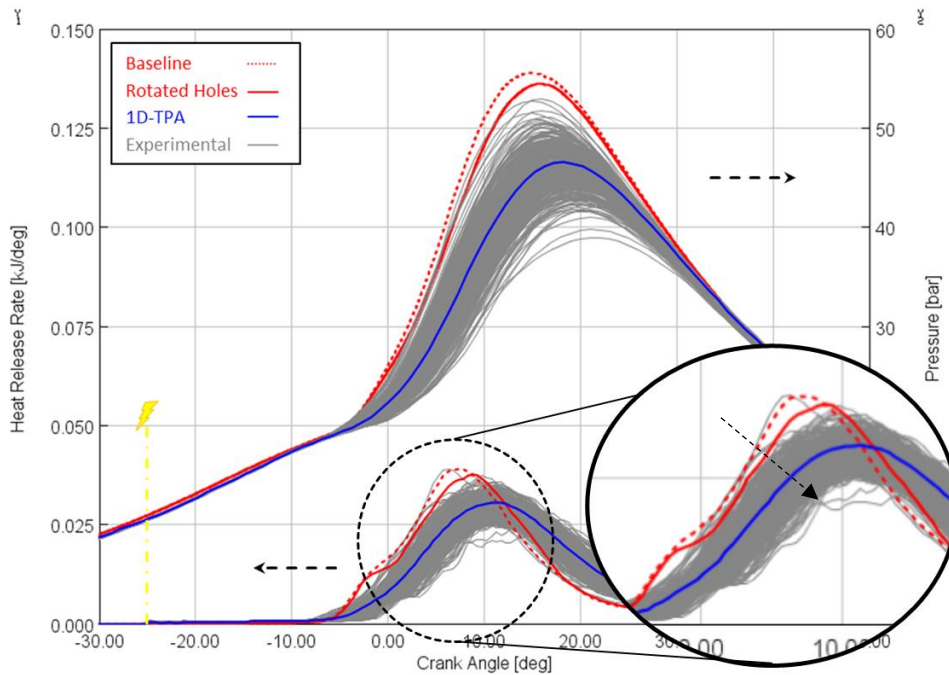


Figure 76: 4000 rpm x  $\lambda=1$  Holes Rotation – Heat Release Rate (Zoomed)

Assuming the use of the same fuel type and quantity and a pretty similar combustion development in the PC, the chemical effect was considered to be the minor effect explaining the difference between the two layouts.

The thermal effect describes the impact of turbulent mixing of hot jets with the fresh mixture. This effect has two separate aspects to be investigated: turbulent mixing and heat transfer coming from hot gases.

### 3.2.3.5.1 Hot Jets Heat Transfer

To address this effect, the heat transfer rate to the exhaust valves boundary (Boundary 11) was analyzed and is represented in Figure 77 for both baseline and rotated holes layout.

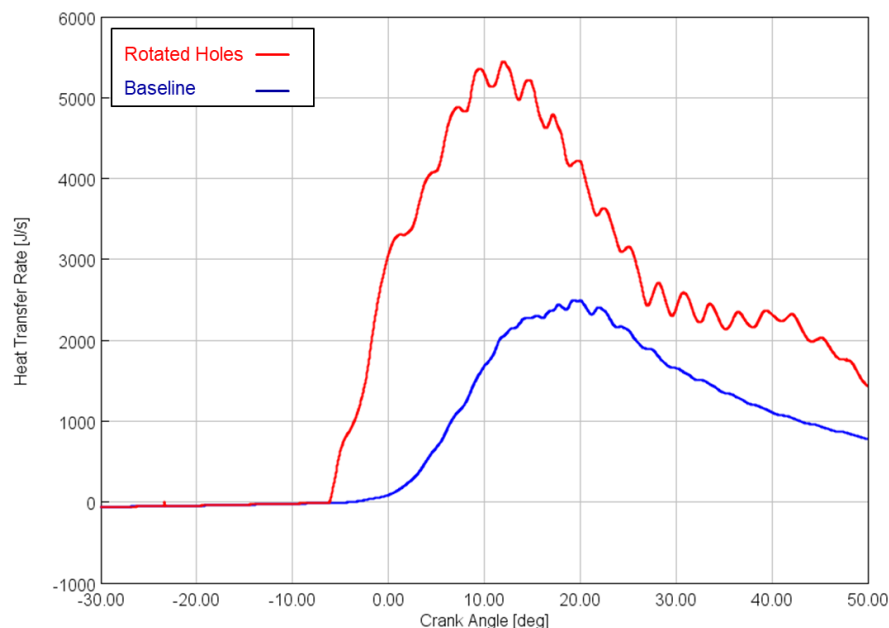


Figure 77: 4000 rpm x  $\lambda=1$  Holes Rotation – Heat Transfer to Exhaust Valves

The results show how the design with rotated holes is characterized by a higher heat transfer rate to the exhaust valves, caused, as said, by the impact of the jet flame with the valves.

The interesting consequence of this evidence is that the heat transferred to the valves is ultimately not transferred to the fresh charge in the cylinder. In turns, having heat exchange with the engine hardware rather than with MC gases leads to a less intense thermal effect, with an influence on the HRR inside the main chamber.

### 3.2.3.5.2 Turbulent Mixing and TKE

Hot jet mixing is expected to be altered by the impact of the turbulent flow with the valves.

The parameter used to analyze this effect is the level of TKE in the cylinder, as reported in Figure 78 along with the traces for mass flow rate from PC to MC, which is used as an aid in defining the jet injection interval. At the start of the jet injection phase, it is noted how the value of main chamber TKE is roughly the same for both cases: this is rightful evidence, as the rotational speed of the engine did not change. Moreover, under this assumption, it is possible to consider any difference in TKE to be caused entirely by the change in geometry.

The levels in Turbulent Kinetic Energy during jet injection show a lower peak for the design with rotated holes: this confirms that the impact with exhaust valves causes dissipation of the turbulent flow field, diminishing the mixing of hot gases with fresh charge.

As a last note, it is highlighted how the absolute values of cylinder TKE could be not entirely representative of the difference between the two layouts, being averaged over the whole MC rather than local.

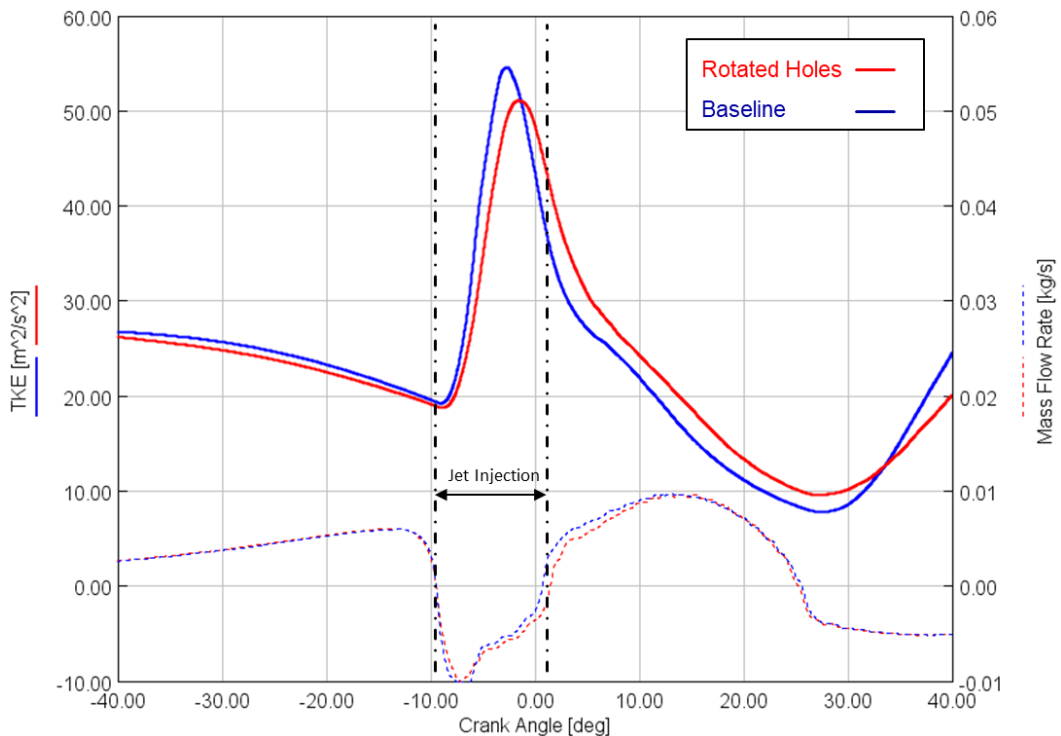


Figure 78: 4000 rpm x  $\lambda=1$  Holes Rotation – Average In-Cylinder TKE

### 3.2.4 Pre-Chamber Holes Rotation at 2000 rpm – $\lambda=1$ VS $\lambda=1.4$

#### 3.2.4.1 Pressure & HRR Results

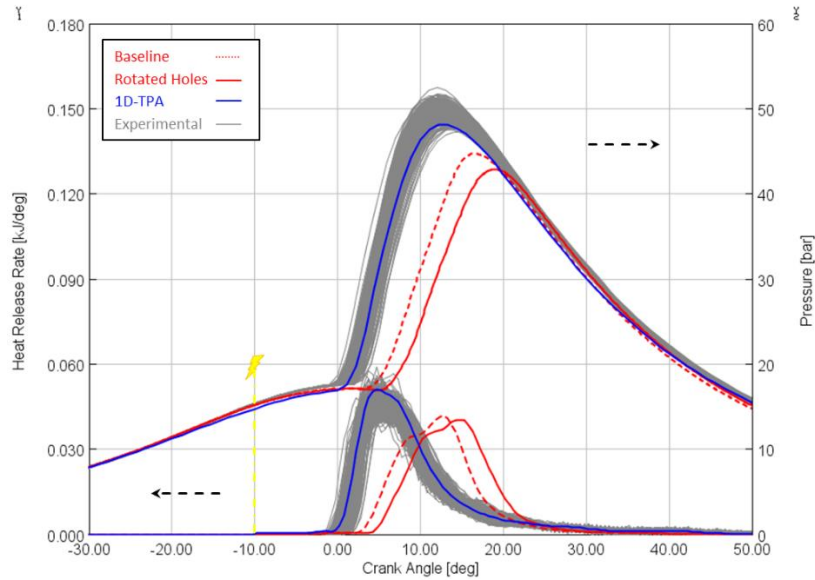


Figure 79: 2000 rpm  $\lambda=1$  Holes Rotation – Pressure and HRR Profiles

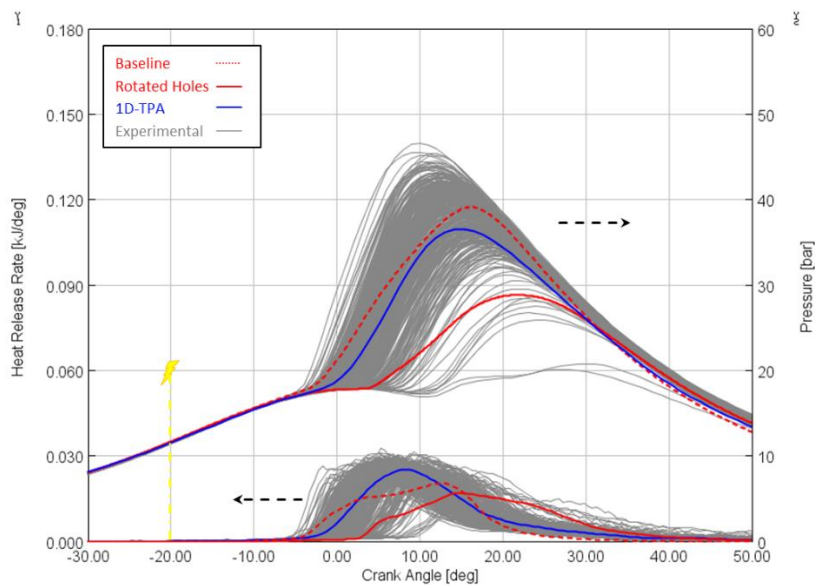


Figure 80: 2000 rpm  $\lambda=1.4$  Holes Rotation – Pressure and HRR Profiles

The resulting outcome seems in agreement with the run in stoichiometric conditions at 4000 rpm, with a decrease in the simulated pressure peak and delayed Heat Release Rate. As such, the same root causes could be expected to be the origin of the observed evidence. With respect to the first case, however, this behavior is much more visible for the 2000 rpm simulations and especially for the lean mixture operation.

### 3.2.4.2 Pre-Chamber Scavenging

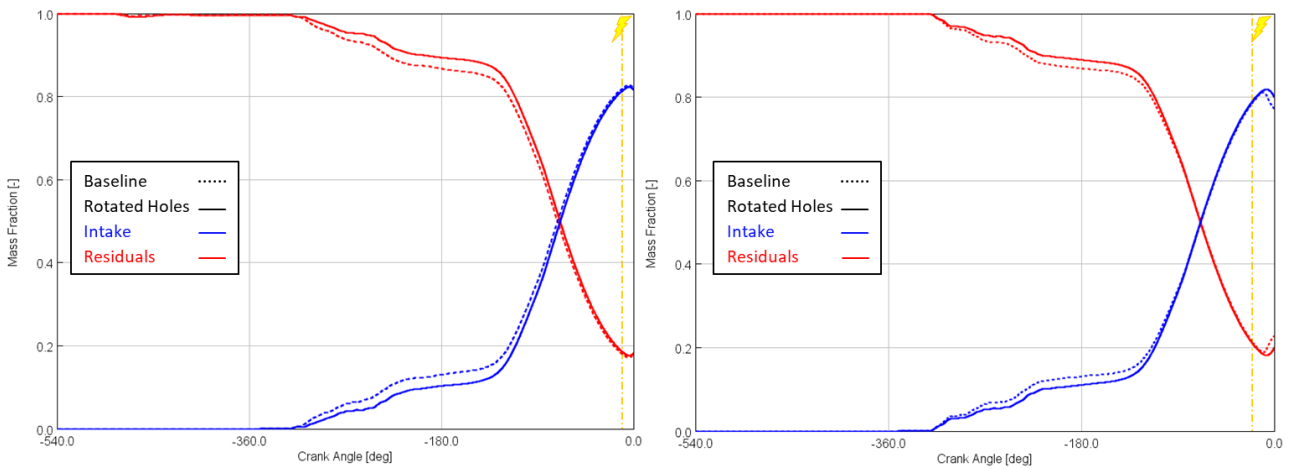


Figure 81: 2000 rpm Holes Rotation –  $\lambda=1.0$  (left) VS  $\lambda=1.4$  (right) PC Scavenging

As for the 4000 rpm case, it appears as if the scavenging performance on pre-chamber average is practically unaffected by the change in layout (Figure 81). The main difference in residuals concentration between the two cases is to be found in the different ST, as already discussed.

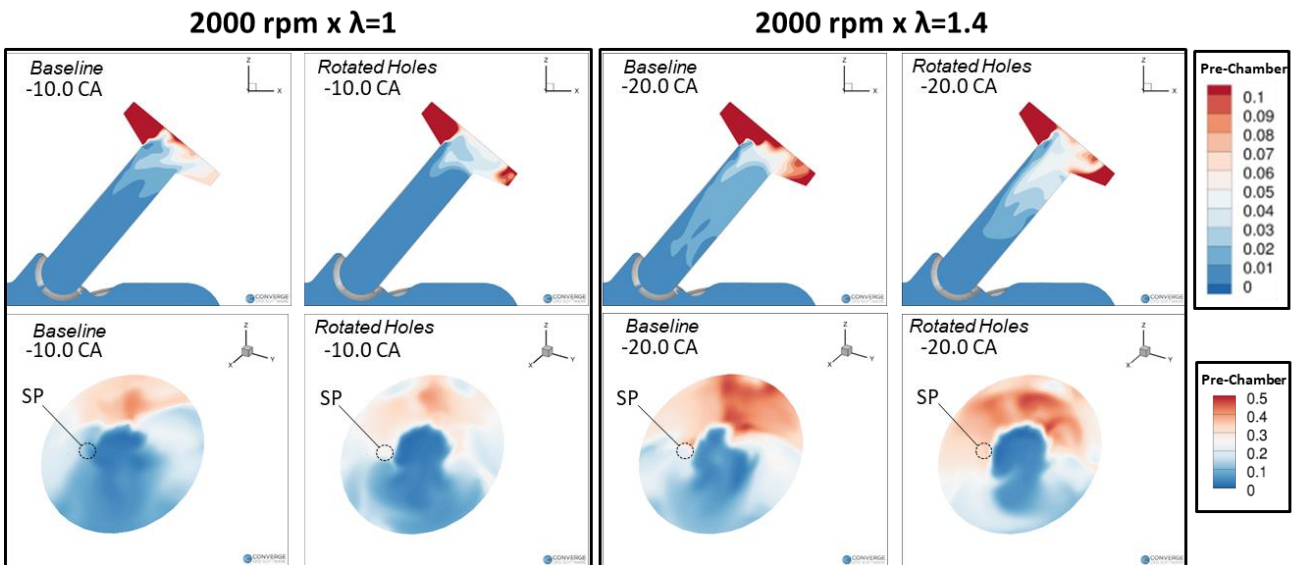


Figure 82: 2000 rpm Holes Rotation –  $\lambda=1.0$  (left) VS  $\lambda=1.4$  (right) PC Residuals Distribution

Nevertheless, differently for the 4000 rpm case, the concentration of residuals around spark plug increases in the configuration with rotated holes (Figure 82), as described in Table 28. Once again, a different ST if the root causes for such results.

| Case                 | Holes Rotation<br>[deg] | Residuals % (PC avg.)<br>@ST<br>[%] | Residuals % around<br>SP @ ST<br>[%] |
|----------------------|-------------------------|-------------------------------------|--------------------------------------|
| 2000 x $\lambda=1$   | -                       | 17.9%                               | 9.2%                                 |
|                      | 45                      | 18.4%                               | 17.5%                                |
| 2000 x $\lambda=1.4$ | -                       | 21.2%                               | 20.8%                                |
|                      | 45                      | 20.9%                               | 34.7%                                |

Table 28: 2000 rpm PC Holes Rotation – PC Scavenging

### 3.2.4.3 Pre-Chamber Turbulent Kinetic Energy

The trends in TKE levels inside the PC at spark timing follow previous evidence, with a decrease in TKE values both on pre-chamber average and around SP. Figure 83, Figure 84 and Table 29 are presented to prove this outcome, while a related discussion is omitted for brevity, as it is the same as for the 4000 rpm x lambda1 case.

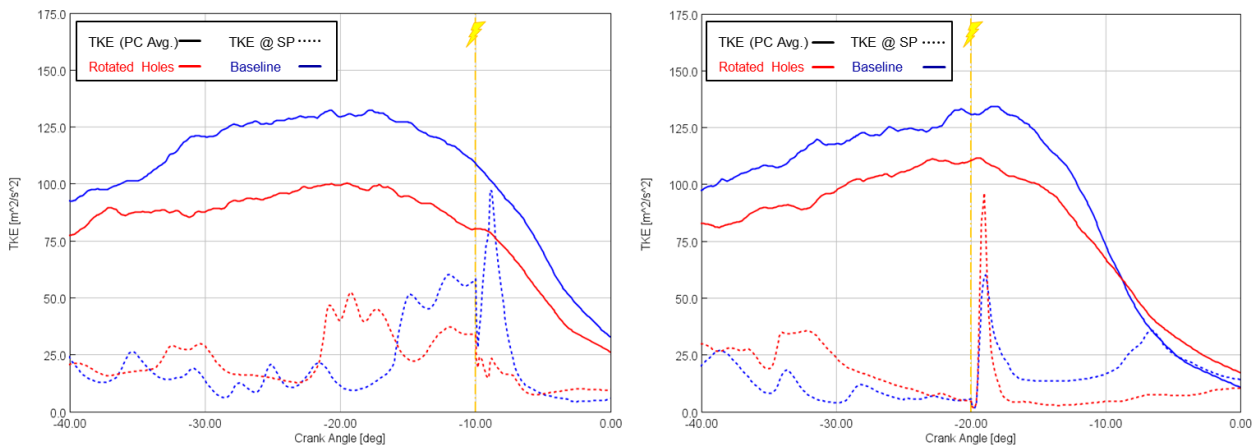


Figure 83: 2000 rpm Holes Rotation –  $\lambda=1.0$  (left) VS  $\lambda=1.4$  (right) PC TKE

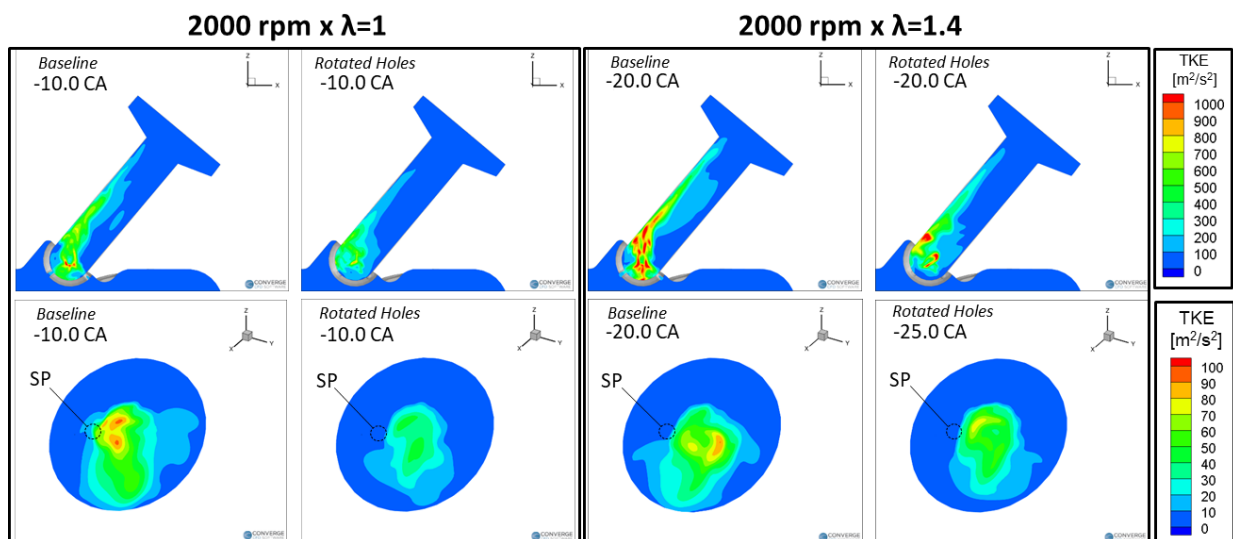


Figure 84: 2000 rpm Holes Rotation –  $\lambda=1.0$  (left) VS  $\lambda=1.4$  (right) PC TKE Distribution

| Case                 | Holes Rotation [deg] | TKE (PC avg.) @ ST [m <sup>2</sup> /s <sup>2</sup> ] | TKE around SP @ ST [m <sup>2</sup> /s <sup>2</sup> ] |
|----------------------|----------------------|--|--|
| 2000 x $\lambda=1$   | -                    | 109.7  | 40.4   |
|                      | 45                   | 80.1   | 12.3   |
| 2000 x $\lambda=1.4$ | -                    | 130.7  | 20.8   |
|                      | 45                   | 110.5  | 19.9   |

Table 29: 2000 rpm PC Holes Rotation – PC TKE

The only additional report on the present investigation is given by comparison of Figure 85 and Figure 86 related to the 2000 rpm x  $\lambda=1$  case, confirming the symmetrical trend in TKE imposed by the rotated holes layout and, with that, confirming how the shape of the PC is fundamental for the turbulence levels obtained inside the PC.

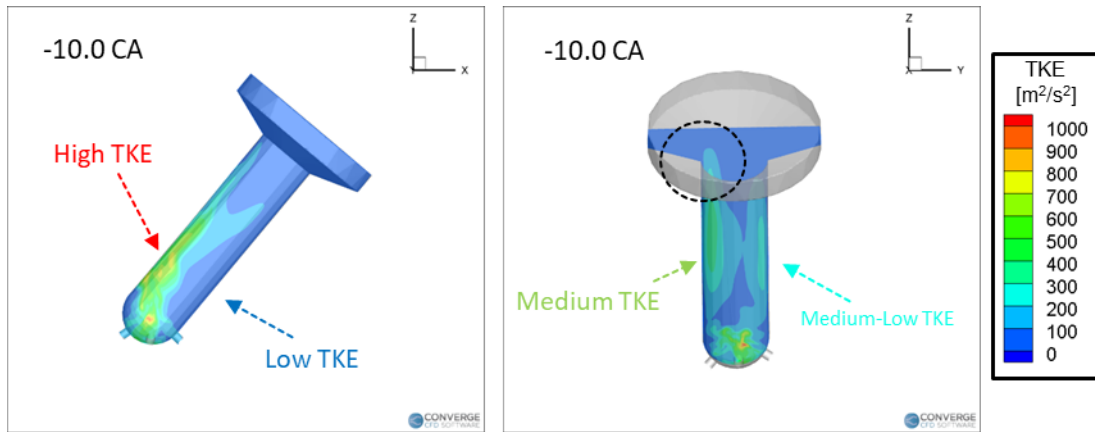


Figure 85: 2000 rpm  $\lambda=1.0$  Holes Rotation – Baseline TKE

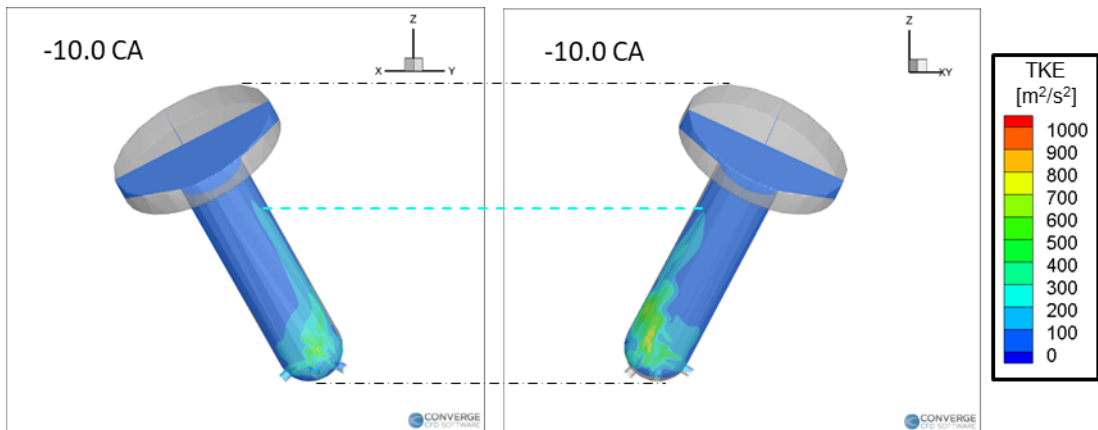


Figure 86: 2000 rpm  $\lambda=1.0$  Holes Rotation – Rotated Holes TKE

### 3.2.4.4 PC/MC Combustion

Figure 87 illustrated the MC-PC pressure and mass flow rate trends for the 2000 rpm x lambda1 and 2000 rpm x lambda 1.4, respectively.

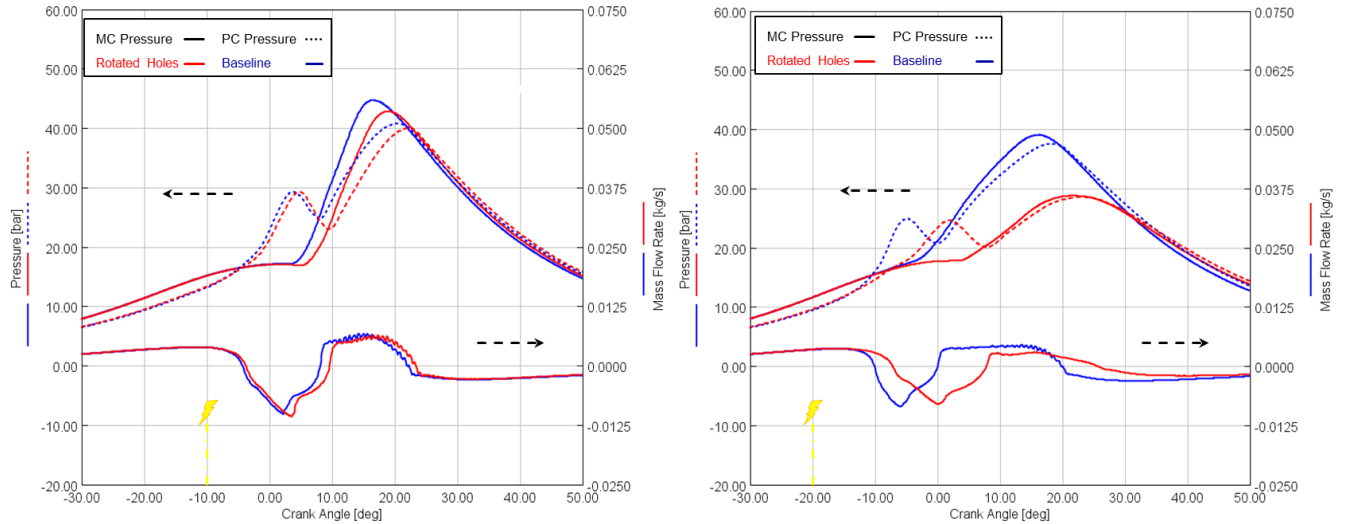


Figure 87: 2000 rpm Holes Rotation –  $\lambda=1.0$  (left) VS  $\lambda=1.4$  (right) PC/MC Pressure Traces

In both cases, the lower values of TKE in the pre-chamber as well as the higher concentration of residuals around spark plug at ST result in a decrease in the pressure levels reached in the cylinder. This fact is particularly evident for the lean case, where the PC combustion event is significantly delayed with respect to the baseline case, as pictured in Figure 88.

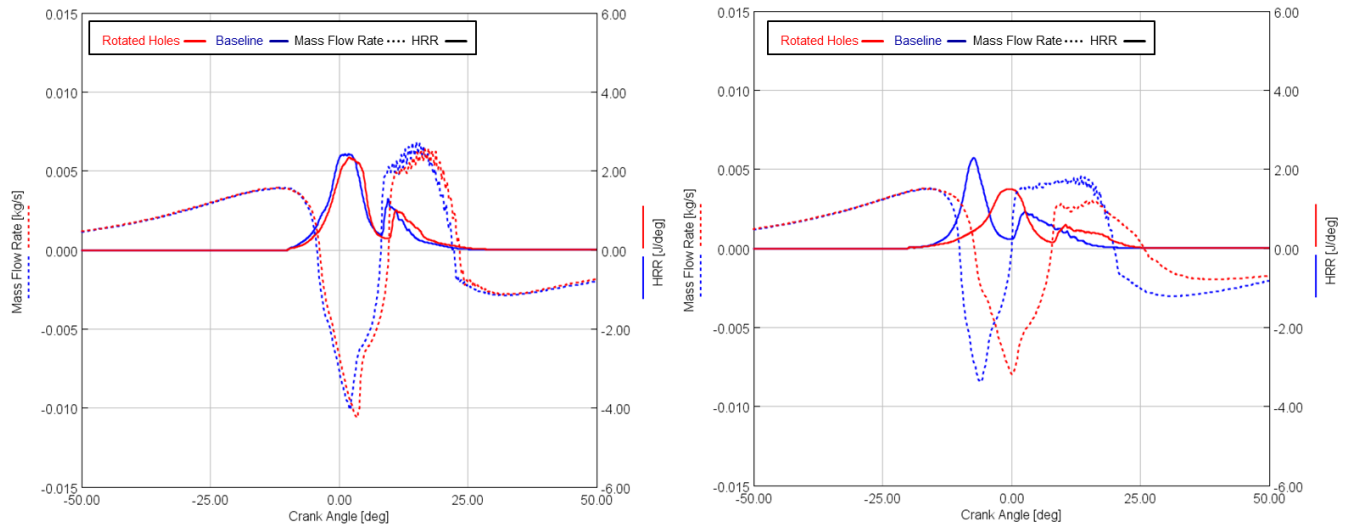


Figure 88: 2000 rpm Holes Rotation –  $\lambda=1.0$  (left) VS  $\lambda=1.4$  (right) PC HRR

As a last comment, it is underlined how the cases at 2000 rpm, differently from the ones at 4000 rpm, show substantial differences when subjected to the rotation of pre-chamber holes. This difference is to be found in the concentration of residuals around SP. In fact, while the cases with holes rotation at 2000 rpm show higher residuals concentration around SP, the simulations at 4000 rpm show the opposite evidence, likely counterbalancing the lower TKE levels inside the PC.

### 3.2.4.5 Flow Reversal: 2000 rpm x $\lambda=1$ VS 4000 rpm x $\lambda=1$

The trends in PC/MC mass flow rate and pre-chamber HRR for both conditions are reported as a comparison in Figure 89, with values of peak HRR and mass flow rate during flow reversal in Table 30.

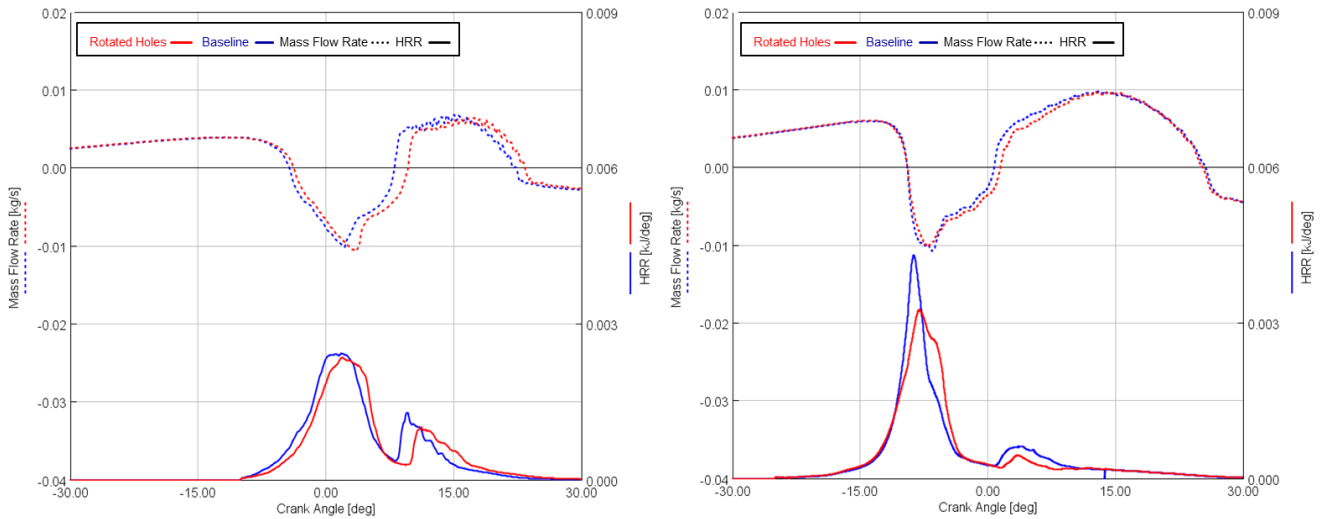


Figure 89: Flow Reversal – 2000 rpm x  $\lambda=1.0$  (left) VS 4000 rpm x  $\lambda=1.0$  (right)

| Case               | Holes Rotation [deg] | Peak HRR [kJ/deg] | Peak Mass Flow Rate [kg/s] |
|--------------------|----------------------|-------------------|----------------------------|
| 2000 x $\lambda=1$ | -                    | 12.9e-04          | 6.0e-03                    |
|                    | 45                   | 10.0e-04          | 6.0e-03                    |
| 4000 x $\lambda=1$ | -                    | 6.2e-04           | 9.7e-03                    |
|                    | 45                   | 4.5e-04           | 9.7e-03                    |

Table 30: Flow Reversal Peak HRR and MFR – 2000 rpm x  $\lambda=1.0$  VS 4000 rpm x  $\lambda=1.0$

A common trend is observed during the flow reversal, regardless of the engine rotating speed: the rotated holes layout resulted in a delayed flow reversal, though with roughly constant duration, and the same peak mass flow rate. Moreover, the second HRR phase shows lower intensity for rotated holes.

The reason for this last evidence is to be found in the mass flow rate of fuel from main chamber to pre-chamber. Figure 90 reports this parameter in hg/s along with the total MC/PC mass flow rate to mark the start of flow reversal and mass of fuel in the cylinder for the stoichiometric 4000 rpm case. This last parameter appears as equal in both cases at the start of flow reversal; vice versa, the rotated holes design shows a small plateau in fuel mass flow rate which does not appear for the baseline case, likely leading to less air/fuel mix pushed back in the PC to burn.

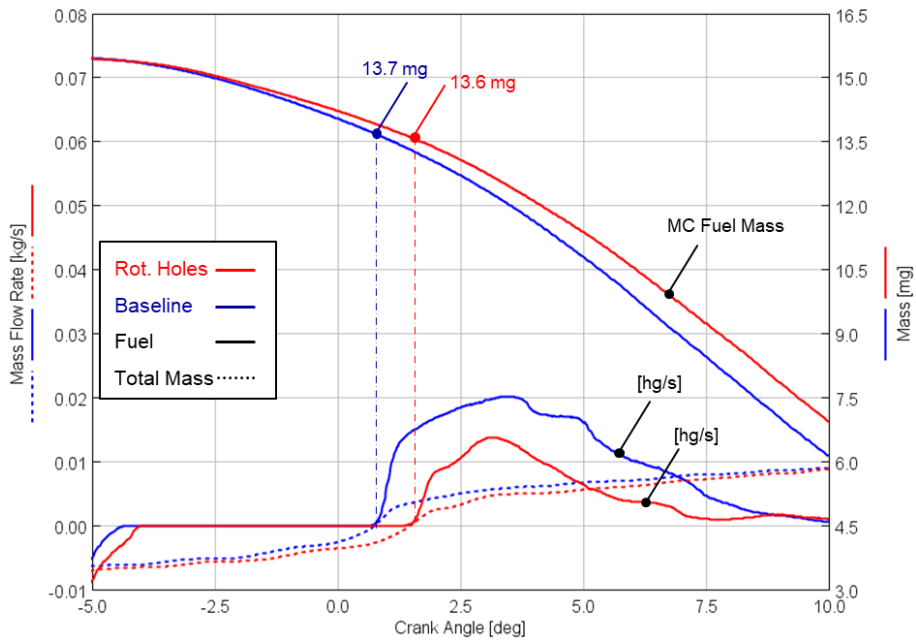


Figure 90: 4000 rpm  $\times \lambda=1.0$  Flow Reversal Characterization

It is interesting to notice how the peak HRR decreases when increasing the engine rotational speed. This fact is to be explained by the amount of fresh charge that goes back from the cylinder into the pre-chamber. Figure 91 reports the traces of mass flow rate and mass flow rate of fuel species from MC to PC, confirming in fact that the slower combustion characterizing the 2000 rpm case leaves more fresh mixture available to enter the PC during the flow reversal and burn.

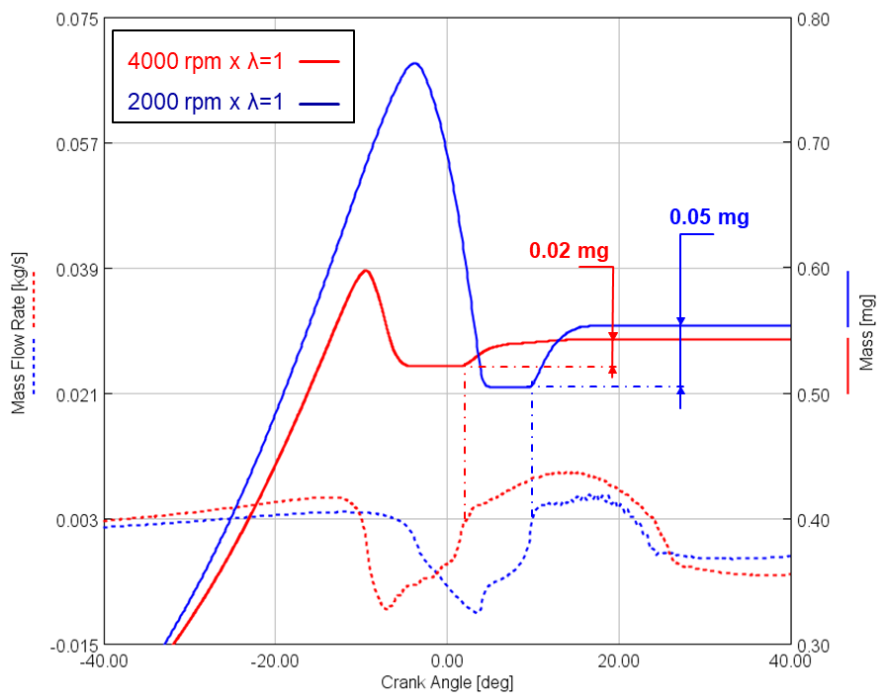


Figure 91: Fuel Flow Reversal – 2000 rpm  $\times \lambda=1.0$  VS 4000 rpm  $\times \lambda=1.0$

### 3.2.4.6 Exhaust Valves Interaction

#### 3.1 2000 rpm vs 4000 rpm (stoichiometric)

This last paragraph is dedicated to the comparison among the different cases about the interaction between exiting hot jets and exhaust valves.

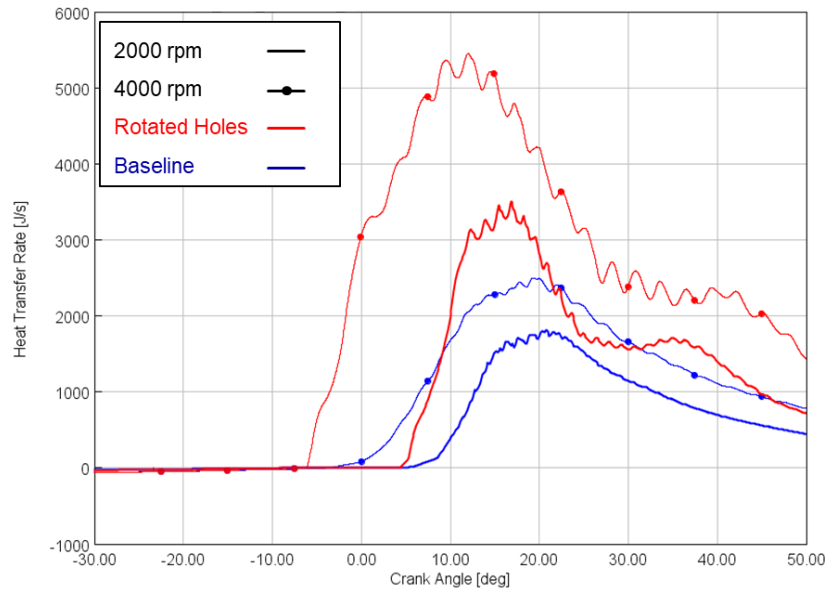


Figure 92: Exhaust Valve Interaction 2000 rpm VS 4000 rpm – Thermal Effect

First of all, the impact of rotational speed in stoichiometric conditions is investigated. Figure 92 shows the trends of heat transfer rate to the exhaust valves at 2000 and 4000 rpm. The difference in heat transfer trend is kept in both cases, with the 4000 rpm one showing a bigger discrepancy between baseline and rotated holes layout. Moreover, the 4000 rpm cases show higher values of heat transfer rate with respect to their 2000 rpm counterparts. The root cause for such evidence is the combustion process inside the pre-chamber and the HRR associated to it (Figure 92). As a matter of fact, the 4000 rpm cycle shows a more intense PC combustion, which leads to higher combustion temperatures and, in turns, higher exiting jets temperatures. This fact, finally, translates in a higher heat transfer to the exhaust valves, which are in both cases at the same temperature. Figure 93 proves this fact by showing the HRR trace in the pre-chamber along the jet exit temperature calculated as average of the four jets.

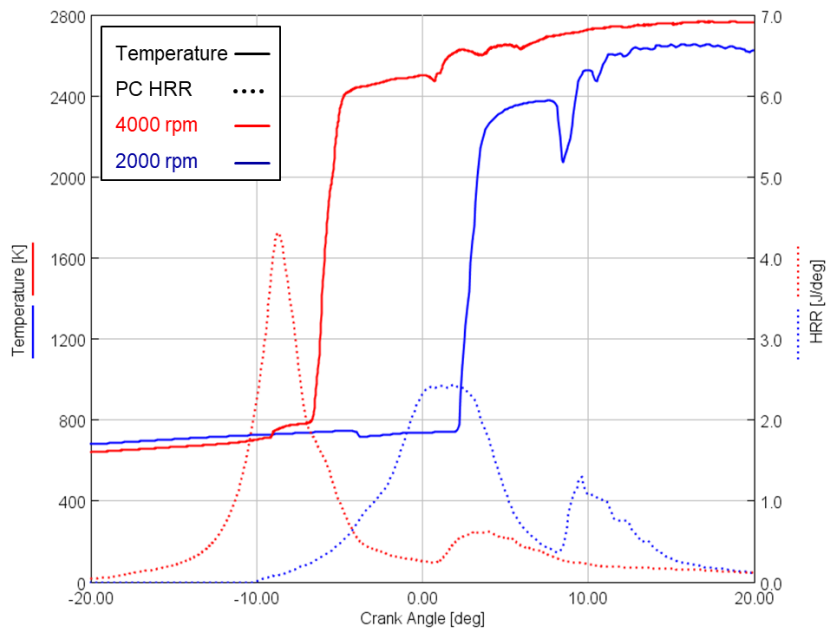


Figure 93: 2000 rpm VS 4000 rpm – PC Combustion and Jet Exit Temperature

The impact on turbulent mixing is expressed in Figure 94, where, once again, it can be seen that the difference in MC Turbulent Kinetic Energy is kept qualitatively the same, with the rotated holes layout showing lower levels of TKE during the jet injection phase.

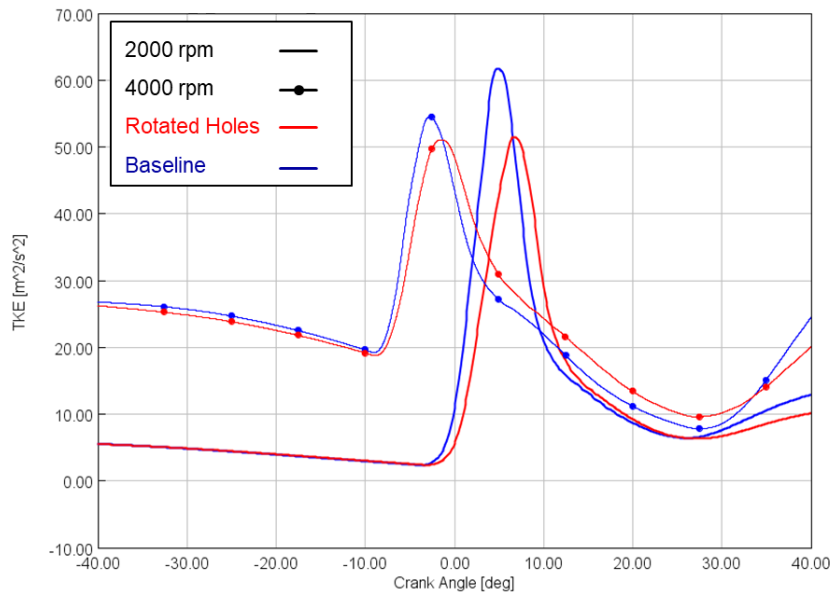


Figure 94: Exhaust Valve Interaction 2000 rpm VS 4000 rpm – Turbulence Effect

The values of TKE at the start of jet injection are lower in the cases at 2000 rpm, a reasonable consequence of the lower engine rotational speed itself. Instead, the fact that during jet injection these cases show higher TKE levels than the cases at 4000 rpm is less intuitive. Two hypotheses were formulated for such observation. First, the injection phase for the 2000 rpm cases occurs mostly during the expansion stroke; this was thought to ease the incoming jet penetration. At the same time, this hypothesis could be discredited by the differential MC-PC pressure during jet injection, which appeared to be quite similar for the two engine rotational speeds. A more numerically related aspect

was also considered; indeed, the values of TKE inside the cylinder are averaged on the whole portion of the computational domain. In particular, the extracted parameter is the mass weighted average in each computational cell of the region, thus, the difference in MC trapped mass could lead to the aforementioned numerical difference. To avoid any possible ambiguity, no numerical values are reported.

### 3.2 Stoichiometric vs Lean mixture: 2000 rpm and 4000 rpm

A comparison between rotated holes and baseline layouts for stoichiometric and lean mixture operated cases is now performed, using the results at 4000 rpm to confirm or disprove the outcomes of the analysis at 2000 rpm.

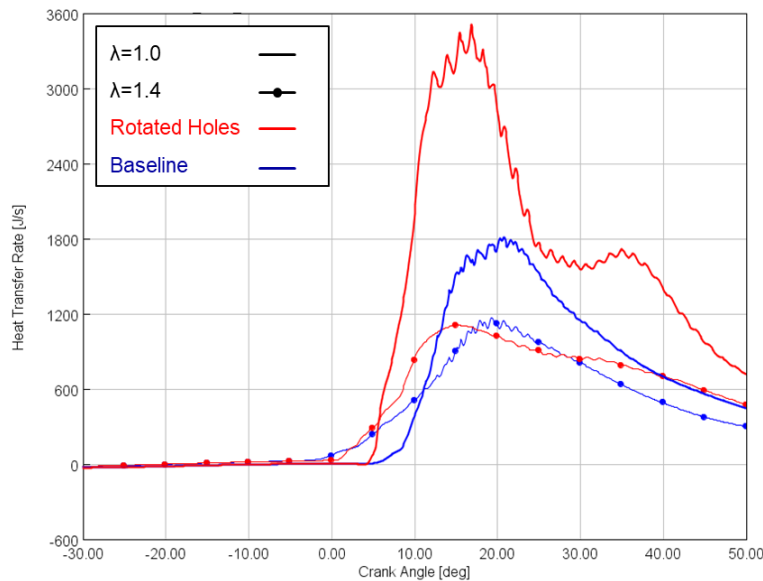


Figure 95: Exhaust Valve Interaction 2000 rpm  $\lambda=1.0$  VS  $\lambda=1.4$  – Thermal Effect

Figure 95 represents the heat transfer rate trends for 2000 rpm at  $\lambda=1$  and  $\lambda=1.4$ . Reasonably, overall values of heat transfer rate are lower for the lean case, as a consequence of lower combustion temperatures inside the pre-chamber. The big difference in profiles observed in the stoichiometric case seems to be slimmed by the lean mixture operation. The initial higher heat transfer for the rotated holes seems to be maintained as well as the one later during the combustion process. Instead, the peak value of such parameter is practically the same in both cases.

The discrepancy between lean and stoichiometric case is not as evident for the 4000 rpm runs (Figure 96). In particular, the lean mixture outcome still shows a significant difference between rotated holes and baseline configuration, although lower than the stoichiometric case.

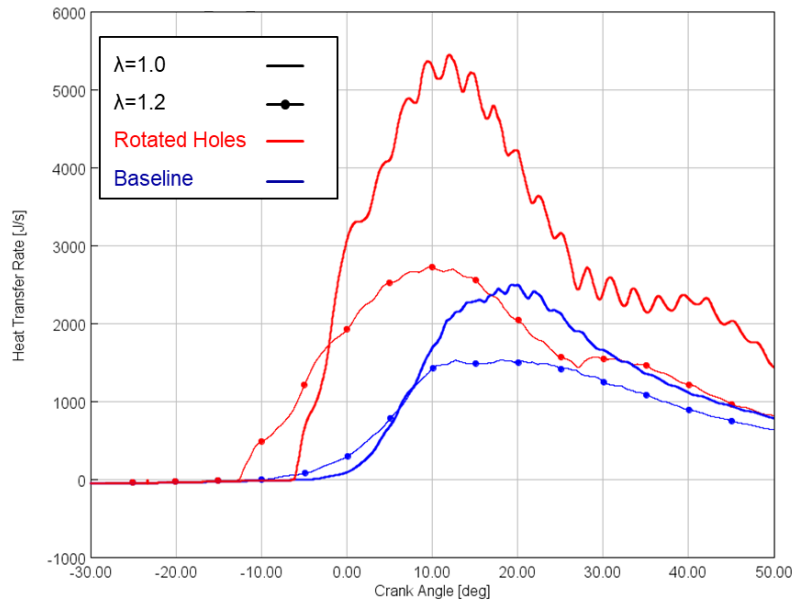


Figure 96: Exhaust Valve Interaction 4000 rpm  $\lambda=1.0$  VS  $\lambda=1.2$  – Thermal Effect

The impact on TKE levels created by jet injection is illustrated in Figure 97. Overall, the lean cases generate a lower peak in MC Turbulent Kinetic Energy, as a reasonable consequence of a less intense combustion event inside the pre-chamber. The difference in TKE between rotated holes and baseline is kept both for stoichiometric and lean mixture operation. Interestingly, such difference appears to be the same for the two cases (roughly  $10 \text{ m}^2/\text{s}^2$ ).

This evidence seems to be confirmed by the runs at 4000 rpm (Figure 98), where, once again, the difference between rotated holes and baseline layout is kept roughly constant in stoichiometric and lean conditions, although slightly lower than for the analysis at 2000 rpm (roughly  $4 \text{ m}^2/\text{s}^2$ ).

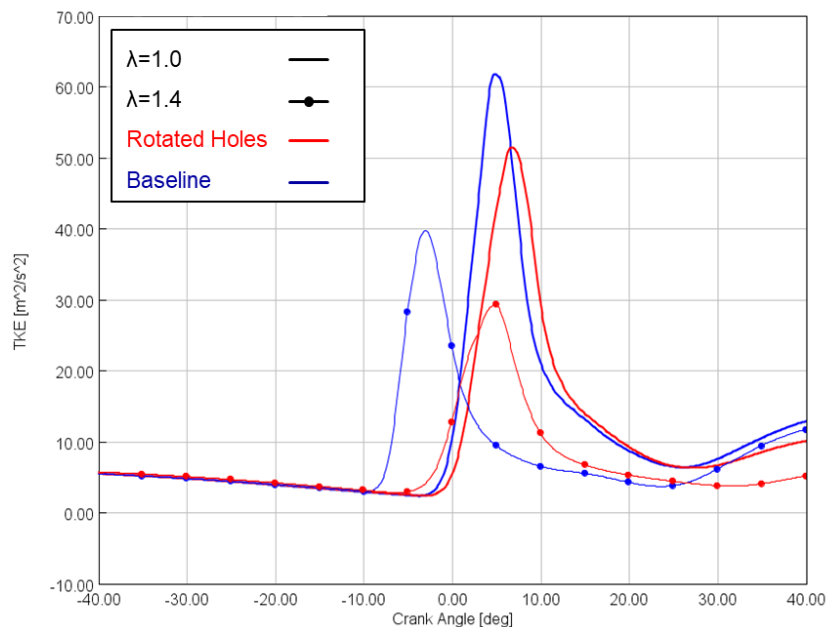


Figure 97: Exhaust Valve Interaction 2000 rpm  $\lambda=1.0$  VS  $\lambda=1.4$  – Turbulence Effect

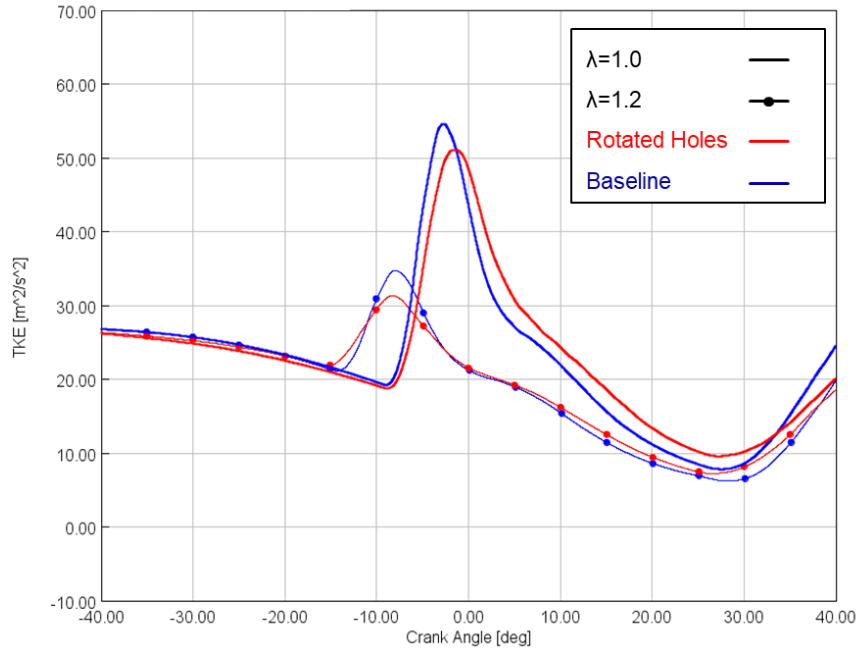


Figure 98: Exhaust Valve Interaction 4000 rpm  $\lambda=1.0$  VS  $\lambda=1.2$  – Turbulence Effect

### 3.3 Effect of Boundary Conditions

To conclude the analysis on TJI combustion, the results at a medium rotational speed of 3000 rpm in stoichiometric and lean conditions are briefly reported. Figure 99 shows the traces of pressure and Heat Release Rate inside the cylinder as the ones inside the pre-chamber.

A common behavior with the tests at 4000 rpm is evidenced, with an overestimation of peak pressure and HRR levels for the 3D-CFD output with respect to the experimental average.

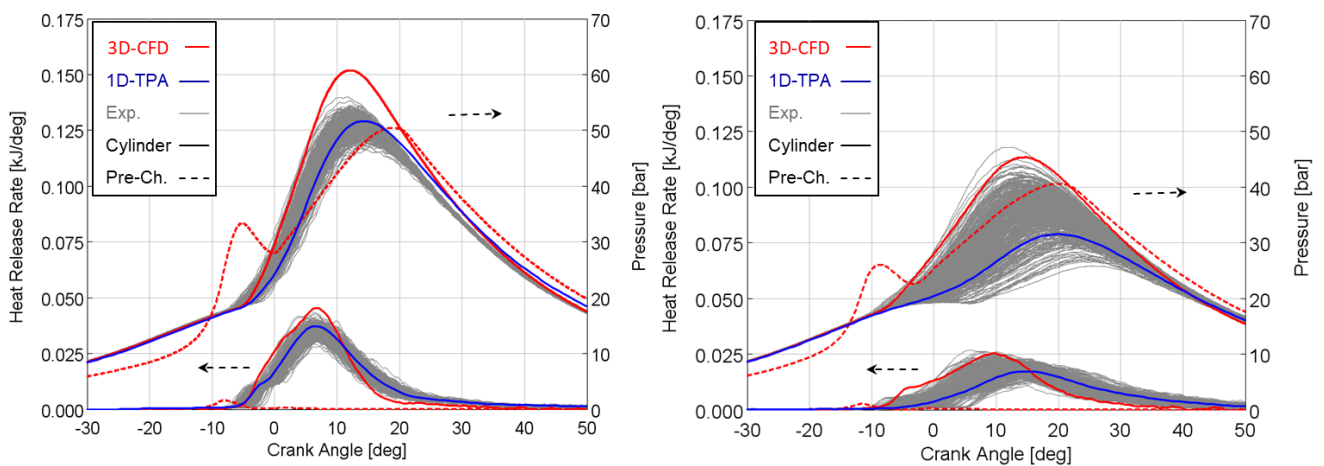


Figure 99: 3000 rpm  $\lambda=1$  (left) VS 3000 rpm  $\lambda=1$  (right)

To address more in depth the reasons for the described deviations, an investigation on the effects of the provided boundary conditions was performed. In particular, the quantity of residuals and intake

mass, as well as the total trapped mass inside the cylinder at IVC were compared between the TPA and 3D-CFD results. This was done after specific tests proving how the model boundary conditions can be assumed as the main source of discrepancy between experimental and numerical results. The last of these tests featured a change in Reaction Multiplier, a parameter used to slow down chemical reactions speed; no difference was found for values of 1.0, 0.98 and 0.95.

Table 31 reports the aforementioned quantities for all the cases discussed in this work.

| At IVC:                      |      | 2000 rpm      |               | 3000 rpm      |               | 4000 rpm      |               |
|------------------------------|------|---------------|---------------|---------------|---------------|---------------|---------------|
|                              |      | $\lambda=1.0$ | $\lambda=1.4$ | $\lambda=1.0$ | $\lambda=1.4$ | $\lambda=1.0$ | $\lambda=1.2$ |
| Residuals Concentr. - TPA    | [%]  | 7.8%          | 7.7%          | 2.3%          | 2.4%          | 2.1%          | 2.5%          |
| Residuals Concentr. - CNV    | [%]  | 9.8%          | 9.5%          | 1.2%          | 1.2%          | 1.7%          | 2.2%          |
| In-Cyl. Residuals Mass - TPA | [kg] | 1.71e-05      | 1.69e-05      | 5.50e-06      | 5.73e-06      | 5.20e-06      | 6.23e-06      |
| In-Cyl. Residuals Mass - CNV | [kg] | 2.05e-05      | 2.00e-05      | 2.87e-06      | 2.97e-06      | 4.20e-06      | 5.33e-06      |
| In-Cyl. Intake Mass - TPA    | [kg] | 2.02e-04      | 2.03e-04      | 2.41e-04      | 2.38e-04      | 2.48e-04      | 2.44e-04      |
| In-Cyl. Intake Mass - CNV    | [kg] | 1.84e-04      | 1.88e-04      | 2.43e-04      | 2.44e-04      | 2.46e-04      | 2.41e-04      |

*Table 31: Effect of Boundary Conditions*

Looking at the results, the 3D-CFD cases at 3000 rpm and 4000 rpm appear as consistently underestimating the concentration of residuals inside the cylinder at IVC.

At the same time, a marginal underestimation of the amount of intake mass, made of air and fuel, is present, except for the lean 3000 rpm case. These observations could explain the overestimation of the pressure trace, common for the 3000 and 4000 rpm results.

The cases at 2000 rpm, instead, display an overestimation of residuals concentration at IVC. Considering that their total amount, and thus their relative importance during the combustion process, is one order of magnitude bigger than the other cases, it can be assumed that such overestimation is the root cause of the lower pressure peak characterizing the simulations at 2000 rpm.

It can be ultimately concluded how the boundary conditions have a major impact on the present results. Further improvements could involve a refinement of the TPA model, necessary to obtain the boundary conditions for the 3D-CFD model.

### 3.4 Flame Hole Interaction

The next section is aimed at describing the results obtained during the analysis of the flame/hole model and the application of the methodology proposed by Mastorakos. Moreover, a further application of such methodology will be carried on other experiments performed by Biswas in ([26]) to confirm or refute the evidence previously found. Finally, an investigation on an engine case, the input data of which comes from 3D-CFD simulation, will be performed, in order to assess qualities and limits of said methodology when applied in the ICE framework.

#### 3.4.1 Flame/Hole Interaction Model

##### 3.4.1 Jet Ignition

At first, the qualitative outcome of the Flame/Hole interaction model is presented with a series of illustrations representing different time steps of the simulation. Traces of Temperature, concentration of OH and Chemical Source Passive (i.e.: a passive indicating the amount of released chemical energy) will be used to trace the flame front propagation, as well as main chamber ignition.

The jet ignition case is the first case analyzed. Figure 100 shows the first time sequence investigated, starting from the moment at which the flame front arrives at the pre-chamber hole inlet. It is interesting to notice that the flame front is able to propagate inside the pre-chamber, as indicated by the presence of OH and the trace of Chemical Source Passive, being the latter a passive representative of chemical reactions intensity.

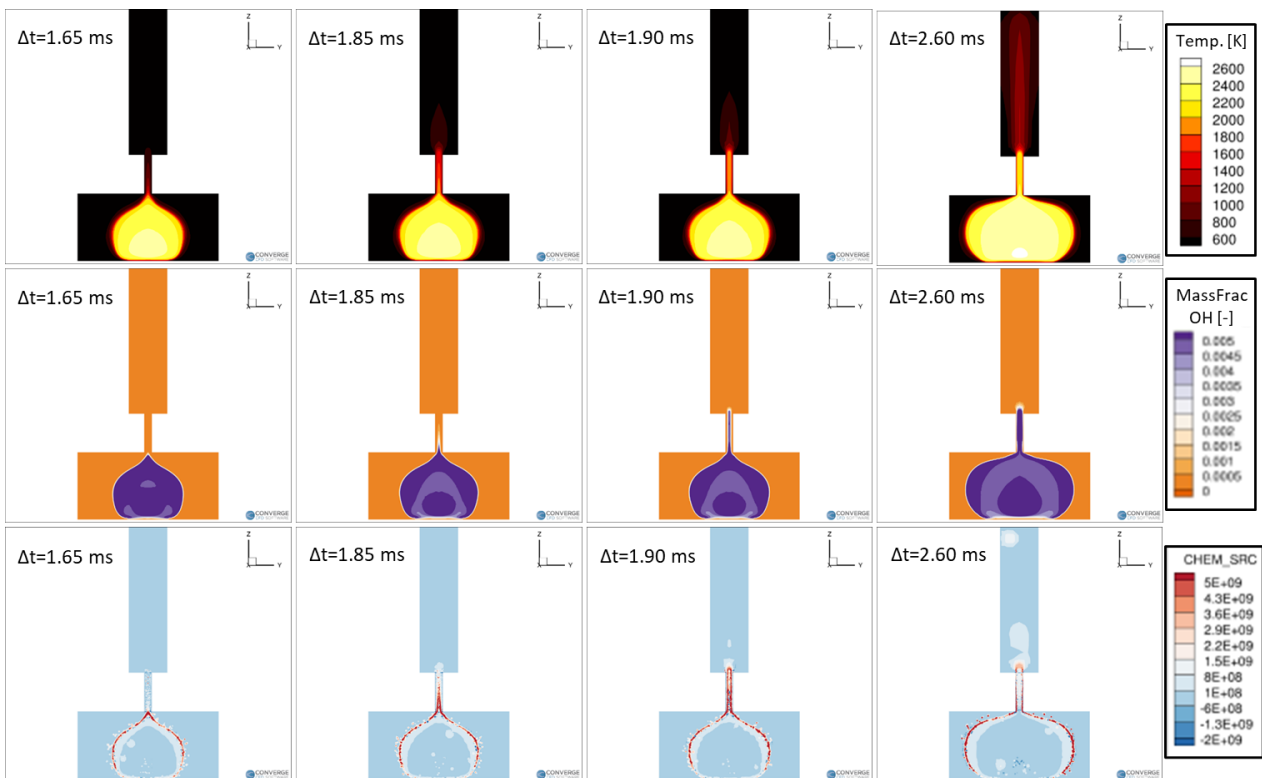


Figure 100: Jet Ignition Model - Top: Temperature; Middle: OH Mass Fraction; Bottom: Chemical Source; Delta-time values refer to time passed after spark timing

Vice versa, the flame does not propagate within the main chamber, as the traces of OH and Chemical Source disappear after the hole outlet. The outcome is a stream of high temperature partial oxidation products inside the main chamber via a jet with a hot core.

Figure 101 represents the following time steps. The jet with high temperature core formed by partial oxidation products keeps being injected into the main chamber, with its core temperature progressively increasing. No sign of ignition is present after 2.60 ms, although the region with low level of Chemical Source Passive starts to expand along the main chamber.

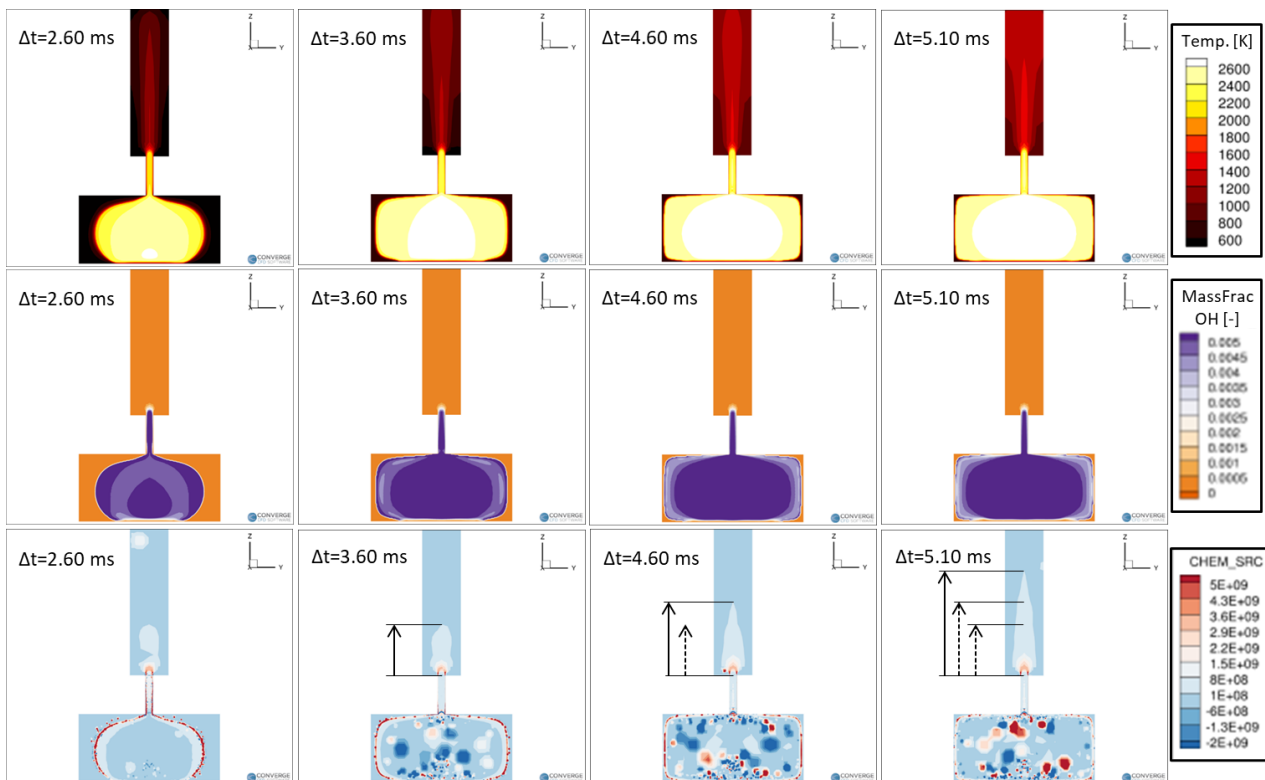


Figure 101: Jet Ignition Model - Top: Temperature; Middle: OH Mass Fraction; Bottom: Chemical Source; Delta-time values refer to time passed after spark timing

As the high temperature jet and Chemical Source Passive trace expand along the main chamber, a change in view is required: hence, from Figure 102, the system is shown from a larger point of view, allowing to better capture the events inside the main chamber.

Figure 102 shows the instant at which ignition finally occurs inside the main chamber. In particular, the trace of Chemical Source Passive suddenly shows an area of very high intensity together with local high temperature; moreover, at the same time, OH species are appearing. It is interesting to notice how ignition occurs far away from the pre-chamber hole, a typical sign of turbulent jet ignition. Ignition seems to occur after 5.75 ms, differently from Biswas' experimental outcome.

After ignition, a flame front propagates inside the main chamber. Any preferential direction of propagation is not observable from the model, having, as said, the side of the main chamber “cut” to save computational cost.

It can be concluded that the model is successful in capturing the jet ignition event from a qualitative standpoint.

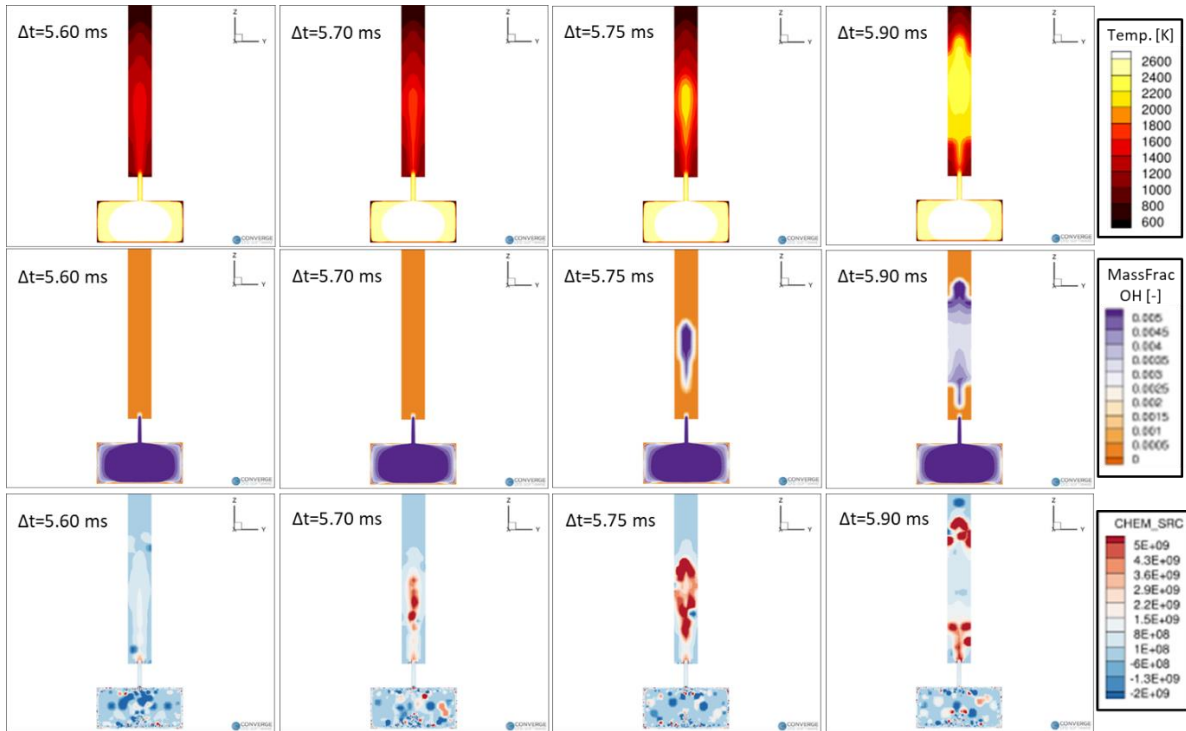


Figure 102: Jet Ignition Model - Top: Temperature; Middle: OH Mass Fraction; Bottom: Chemical Source; Delta-time values refer to time passed after spark timing

### 3.4.2 Flame Ignition

To conclude this first qualitative analysis, the flame ignition case is investigated in the same way as the jet ignition one. Figure 103 describes the most interesting time steps associated to such case. As it appears, the flame ignition simulation is far simpler than the jet ignition one. As a matter of fact, the flame is able to pass through the hole and travel inside the main chamber without any extinction.

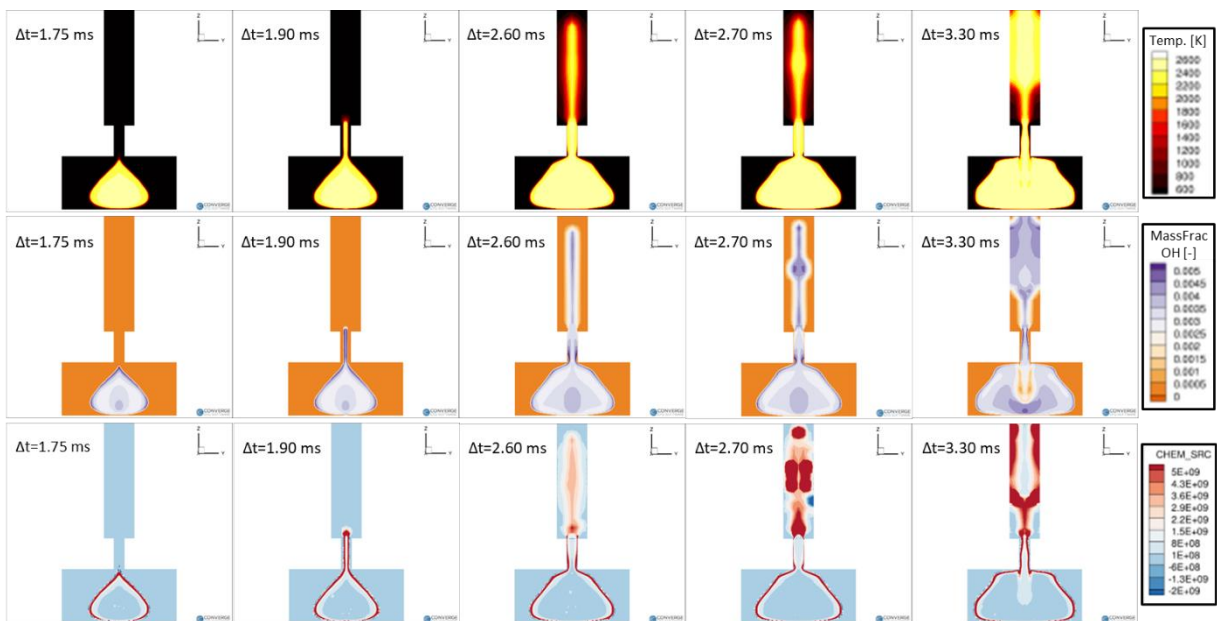


Figure 103: Flame Ignition Model - Top: Temperature; Middle: OH Mass Fraction; Bottom: Chemical Source; Delta-time values refer to time passed after spark timing

More in details, the flame is injected in the main chamber in the form of a cylindrical jet, propagating along the axis of the hole and main chamber. Once the flame jet has successfully penetrated in the main chamber, flame propagation starts from the periphery of the jet.

To conclude, the signs of OH and Chemical Source are indicating a flame passing through the hole, thus allowing the model to correctly describe the flame ignition phenomenon. It is interesting to notice how the different behaviors for 2.5 mm and 4.5 mm holes are in agreement with measurements on methane quenching diameter, often found in the literature to have a value of 3.5 mm ([33]).

### 3.4.2 Application of Mastorakos' Theory

The methodology proposed by Mastorakos was applied to the previously discussed cases, calculating the Laminar Flame Thickness with the Converge Chemistry Tools. Values for unburned temperature and pressure were assumed to be the ones at start of simulation, while no EGR or residuals were considered. The obtained values are reported in Table 32.

| Case           | Hole Diameter (d)<br>[mm] | Laminar Flame Thickness (LFT)<br>[m] | 2*LFT/d<br>[-] |
|----------------|---------------------------|--------------------------------------|----------------|
| Jet Ignition   | 2.5                       | 3.65e-04                             | 0.29           |
| Flame Ignition | 4.5                       | 1.32e-04                             | 0.06           |

*Table 32: Jet Ignition and Flame Ignition Model Results*

As evident, the results are far from the unitary value proposed by Mastorakos, highlighting a quantitative discrepancy in the analysis. The cause for this evidence is assumed to be the gas temperature and pressure levels, which are different from the atmospheric conditions upon which the methodology was developed.

Still, a qualitative trend is highlighted. In fact, while values are still not close to unitary values, there is a big difference of one order of magnitude between the jet and flame ignition cases; the flame ignition cases show a value much lower than unity, thus being very likely in the realm of flame passage; vice versa, the jet ignition case shows a value lower but much closer to unity, hinting to be closer to a condition of flame extinction.

### 3.4.3 Extension of Biswas Experiments

Given the results obtained with Mastorakos' theory in the 3D-CFD jet and flame ignition cases, the application of such theory was extended to a new set of available experimental data (Figure 104).

Qualitatively, the consequence that can be drawn is that extinction likelihood is increased by using smaller diameters and leaner mixtures.

The investigated methodology was applied to the results in Figure 104, in order to replicate it in terms of 2\*LFT/d ratio values. For each combination of equivalence ratio provided, the Laminar Flame Thickness was calculated with the Converge Chemistry Tools, and the 2\*LFT/d ratio was calculated with the information on hole diameter.

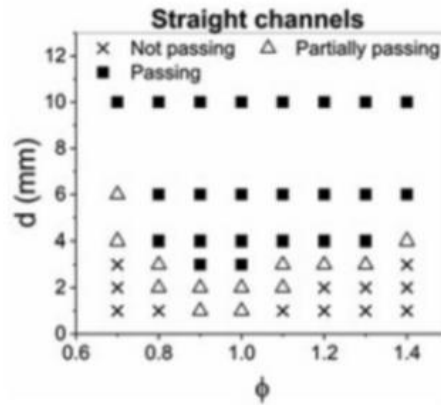


Figure 104: Experimental results concerning flame-hole interaction in straight channels as a function of diameter and equivalence ratio ([26])

Figure 105 shows the results of the  $2*LFT/d$  ratio for each case reported in Figure 104. Based on the conclusions drawn from the first analysis and willing to define a range describing the different flame behavior, a value of 0.29 was used to divide cases of flame extinction and flame passage. The definition of “flame barely passing” represented quite a challenge in this type of description, being a not-so-clear phenomenological aspect. Nevertheless, a further threshold of 0.4 was introduced to divide barely passing and passing flames. The results of the described approach are represented by the indicated colors in Figure 105. Moreover, dashed squares are introduced to indicate the experimental outcome in the case of a discrepancy with the proposed methodology.

| phi [-] \ d [mm] | 0.7  | 0.8  | 0.9  | 1    | 1.1  | 1.2  | 1.3  | 1.4  |
|------------------|------|------|------|------|------|------|------|------|
| 10               | 0.10 | 0.08 | 0.08 | 0.07 | 0.07 | 0.07 | 0.09 | 0.12 |
| 8                | 0.12 | 0.10 | 0.10 | 0.09 | 0.09 | 0.09 | 0.11 | 0.15 |
| 6                | 0.16 | 0.14 | 0.13 | 0.12 | 0.12 | 0.12 | 0.15 | 0.20 |
| 4                | 0.24 | 0.21 | 0.19 | 0.18 | 0.18 | 0.19 | 0.22 | 0.30 |
| 3                | 0.32 | 0.28 | 0.25 | 0.24 | 0.24 | 0.25 | 0.29 | 0.39 |
| 2                | 0.48 | 0.41 | 0.38 | 0.37 | 0.36 | 0.37 | 0.44 | 0.59 |
| 1                | 0.96 | 0.83 | 0.76 | 0.73 | 0.72 | 0.75 | 0.87 | 1.18 |

- Flame Passing
- Barely Passing
- Flame Extinction
- No Evidence
- Experimental Outcome

Figure 105: Results of  $2*LFT/d$  analysis, with Expected Outcome (color) and Phenomenological Evidence (dashed shapes)

As it appears, the proposed methodology and the defined extinction index are in good agreement with the experimental evidence. In particular, more errors arise when moving further way from the stoichiometric operation. For such reason it could be possible that the threshold values adopted are varying with equivalence ratio, however this aspect was not investigated in the present work. Nevertheless, the 0.29 threshold seems to consistently define a threshold with the flame passage condition.

It is worth highlighting, though, that the experimental definition of “Barely Passing” is uncertain and test cases defined by that evidence were not investigated with a 3D-CFD simulation. As such, no

insight about the behavior of a “Barely Passing” flame was gathered; nevertheless, the points manifesting the “Barely Passing” outcome were kept in order to provide a direct comparison with the work carried out in [26].

### 3.4.4 Engine Application

Finally, an application in engine conditions is performed to address how the results could change based on different pressure and temperature levels, which, in turns, have an impact on the Laminar Flame Thickness characterizing the combustion flame. It is anticipated that values of unburned temperature and pressure will be in the range of 700 K and 20 bar, much different with respect to the previous cases.

In particular, results coming from a 3D-CFD simulation at 3000 rpm with  $\lambda=1$  and  $\lambda=1.4$  of the already discussed TJI single cylinder will be used to obtain the levels of unburned pressure and temperature. Moreover, additional results with a pre-chamber diameter of 0.8 mm in stoichiometric conditions will be used to provide a further comparison. Calculations were performed on the average unburned temperatures and pressures of the four pre-chamber holes at flame arrival, a time instant defined by the rise in temperature and OH mass fraction of the monitor point placed inside the holes. Table 33 reports the results addressing, respectively, the impact of different mixture composition and different pre-chamber hole diameter.

| Cases →     | 3000 rpm x $\lambda=1$ |          | 3000 x d=1 mm |               |
|-------------|------------------------|----------|---------------|---------------|
|             | d=1 mm                 | d=0.8 mm | $\lambda=1$   | $\lambda=1.4$ |
| 2*LFT/d [-] | 0.052                  | 0.070    | 0.052         | 0.061         |

*Table 33: Mastorakos Methodology and Engine Application*

Qualitatively, the results appear in agreement with the experimental evidence of [26]. In fact, both a decrease in hole diameter and increase in dilution ratio increase the value of 2\*LFT/d ratio, meaning that the outcome of the flame-wall interaction is moving towards a higher extinction likelihood.

Yet, there is still a big difference between the value proposed by Mastorakos and the values obtained in the current study. In fact, it is quoted in [25] that the LFT is obtained at atmospheric conditions of unburned gases and in the order of magnitude of 10<sup>-4</sup> m; meanwhile, LFT values for the engine combustion cases is in the order of magnitude of 10<sup>-5</sup> m. This difference is due to the different conditions at which combustion is taking place, which are way higher in the engine case. Higher unburned temperatures and pressures at flame arrival have the effect of decreasing the Laminar Flame Thickness: consequently, the 2\*LFT/d ratio is decreased in a significantly.

Combining the results coming from the application on the experiments of Biswas and the engine simulations it can be concluded that levels of gas temperature and pressure significantly influence the values resulting in the calculation of the critical factor 2\*LFT/d according to the theory of Mastorakos. It is still not clear if the threshold values of such critical factor characterizing flame extinction and flame ignition are also functions of pressure and temperatures. Further analyses would

be required to investigate this aspect and better quantify the switch from flame ignition to jet ignition in engine-like conditions.

# Chapter 4

## Conclusions

The present work underlined by means of 3D-CFD simulations the main features of combustion development in a TJI single cylinder engine. Moreover, an investigation on the interaction between hole wall and flame, and its outcome in terms of flame passage or extinction, was carried out by applying a methodology proposed in the literature.

The test case at 4000 rpm and stoichiometric conditions, which was used as reference for the subsequent comparisons, showed an overestimation of the heat release event inside the cylinder, indicating that the numerical cycle is representative of a fast-burning cycle, rather than the experimental average cycle. A detailed analysis highlighted the strong influence of the particular shape of the pre-chamber on all the key aspects of the engine cycle, from PC scavenging and TKE, up to jet injection and main chamber combustion. A comparison with the lean mixture case proved how spark timing is a fundamental calibration parameter in the engine system being studied. Too early ST translate into higher residuals concentration within the PC, due to reduced time for the piston to push fresh mass inside the pre-chamber, and lower TKE, due to lower time available for a turbulent field to develop across the pre-chamber. The stoichiometric and lean cycles showed phenomenological similarities, though characterized by different intensity due to the different spark timing, which affected the concentration of residuals and levels of Turbulent Kinetic Energy. This fact led the lean case to lower peak pressures during PC combustion, with a jet injection and flow reversal event featuring lower intensity with respect to the stoichiometric case.

A sensitivity study of the 3D-CFD model results to turbulent heat transfer was performed by changing the turbulent Prandtl number in the main chamber region. Changing said global transport parameter showed promising results in terms of in-cylinder combustion, effectively bringing the pressure trace closer to the experimental average results. Unfortunately, these benefits are only obtained in small range of turbulent Prandtl number, which for this case was not sufficient to make the 3D-CFD model match the experimental average results in a satisfactory way. This fact could indicate that the change in turbulent Prandtl number should be made in addition to a change of a second parameter.

The effect of a change in pre-chamber geometry was then explored. A sweep of pre-chamber hole diameter was performed, to overcome uncertainties concerning the local geometry of the PC after several hours of engine operations. Smaller holes have proved to bring less fresh mass inside the pre-chamber during the compression stroke, with higher residuals concentration, and higher levels of TKE at spark timing. Yet, pre-chamber combustion is also affected by residuals and TKE distribution around spark plug, the outcome of which is dictated by how well the hole is able to bring intake mass and turbulence to the end of the pre-chamber. The case having diameter equal to 0.9 mm, in particular, showed low levels of residuals around SP despite its relatively small size. The jet injection phase was analyzed, showing that larger holes are able to discharge turbulent jets in shorter time and with larger mass flow rates peaks. Moreover, an investigation on the flow reversal event proved that its intensity, in terms of peak flow rate and HRR, decreases with smaller diameter holes.

Pre-chamber holes rotation was also explored, as other research studies performed on the same engine suggested that a mismatch between expected and effective holes orientation could be present. Hole

orientation at 4000 rpm proved that such feature implies no change in residuals concentration. Instead, lower residuals distribution and lower TKE levels are found with holes rotation, which also grants TKE a more symmetric distribution. The jets interaction with the exhaust valves was proved to be causing a loss in main chamber HRR, due to a thermal and turbulent effect.

The cases at 2000 rpm proved the same qualitative description as the simulation at 4000 rpm, with the only exception of residuals concentration around spark plug, which appears as worsened. Moreover, the flow reversal event appeared less intense with the holes rotated. A comparison among all the simulations regarding the jet-exhaust valves interaction highlighted a thermal effect decreasing its impact for diluted mixtures; the turbulent mixing effect appears as having consistently the same impact between diluted and stoichiometric mixtures, regardless of engine rotational speed.

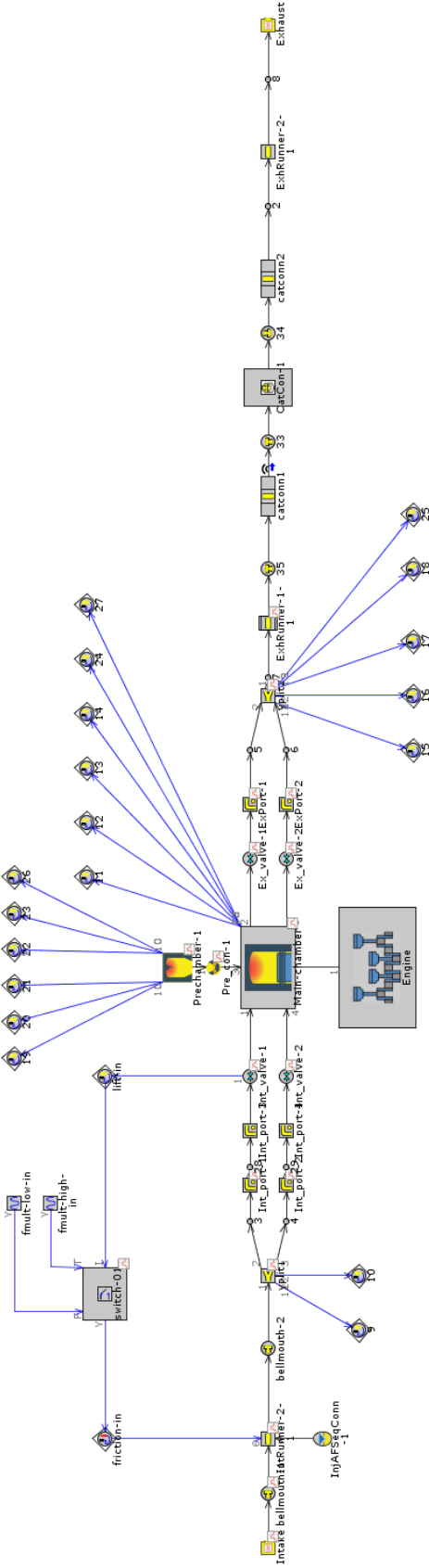
Finally, the impact of boundary conditions on the model was explored, showing that, for this numerical model, they are an especially sensitive input. Future improvements could include the refinement of the TPA model providing the aforementioned boundary conditions.

Additionally, an in-depth study with the aim of investigating the interaction between hole and flame was performed, featuring the application of a methodology proposed by the literature alongside the analysis of a specific 3D-CFD model.

The 3D-CFD model proved to be capable of describing two different phenomena: jet ignition and flame ignition. The application of the theory proposed by Mastorakos, developed under atmospheric conditions, in test conditions led to the definition of a new extinction index, which showed good agreement when applied on a new set of experiments. The same methodology was applied on engine cases, proving that the the ratio between laminar flame thickness and holes diameter is very sensitive to the levels of pressure and temperature of the unburned gases. A specific research in this framework would be necessary to better characterize the distinction between flame passage or extinction in engine-like conditions.

# Appendix

## TPA Model (GT-Suite)



# References

- [1] F. Leach, G. Kalghatgi, R. Stone e P. Miles, «The scope for improving the efficiency and environmental impact of internal combustion engines,» *Transportation Engineering*, vol. 1, June 2020.
- [2] International Energy Agency, "Energy and Air Pollution," *World Energy Outlook*, p. 26, 2016.
- [3] P. Aakko-Saksa, P. Roslund e P. Koponen, «Development and validation of comprehensive emission measurement methods for alternative fuels at VTT,» VTT Technical Research Centre of Finland, 2017.
- [4] O. Delgado e F. Rodriguez, «CO2 emissions and fuel consumption standards for heavy-duty vehicles in the European Union,» ICCT, 2018.
- [5] International Energy Agency, «Global EV Outlook,» 2020.
- [6] International Energy Agency, «World Energy Outlook,» 2016.
- [7] P. Senecal e F. Leach, «Diversity in transportation: Why a mix of propulsion technologies is the way forward for the future fleet,» *Elsevier - Results in Engineering*, vol. 4, 2019.
- [8] B. Thelen, G. Gentz e E. Toulson, «Computational Study of a Turbulent Jet Ignition System for Lean Burn Operation in a Rapid Compression Machine,» *SAE Technical Paper 2015-01-0396*, 2015.
- [9] R. Novella, J. Pastor, J. Gomez-Soriano, I. Barbery, C. Libert, F. Rampanarivo, C. Panagiotis e M. Dabiri, «Experimental and Numerical Analysis of Passive Pre-Chamber Ignition with EGR and Air Dilution for Future Generation Passenger Car Engines,» *SAE Technical Paper 2020-01-0238*, 2020.
- [10] M. Shelef e R. McCabe, «Twenty-five years after introduction of automotive catalysts: what next?,» *Elsevier - Catalysis Today*, vol. 62, 2000.
- [11] B. Thelen e E. Toulson, «A Computational Study of the Effects of Spark Location on the Performance of a Turbulent Jet Ignition System,» *SAE Technical Paper 2016-01-0608*, 2016.
- [12] M. Gholamisheeri, E. Toulson e B. Thelen, «CFD Modeling and Experimental Analysis of a Homogeneously Charged Turbulent Jet Ignition System in a Rapid Compression Machine,» *SAE Technical Paper 2017-01-0557*, 2017.
- [13] M. Muller, C. Freeman, P. Zhao e H. Ge, «Numerical Simulation of Ignition Mechanism in the Main Chamber of Turbulent Jet Ignition System,» *Proceedings of the ASME 2018 Internal Combustion Engine Division Fall Technical Conference*, vol. 2, 2018.
- [14] F. Qin, A. Shah, Z.-w. Huang, L.-n. Peng, P. Tunestal e X.-S. Bai, «Detailed numerical simulation of transient mixing and combustion of premixed methane/air mixtures in a pre-chamber/main-chamber system relevant to internal combustion engines,» *Elsevier - Combustion and Flame*, vol. 188, 2018.
- [15] W. Attard, E. Toulson, P. Parsons e N. Fraser, «A Turbulent Jet Ignition Pre-Chamber Combustion System for Large Fuel Economy Improvements in a Modern Vehicle Powertrain,» *SAE Int. J. Engines 3(2):20-37*, 2010.

- [16] P. Sementa, F. Catapano, S. Di Iorio, M. Todino e B. M. Vaglieco, «Turbulent Jet Ignition Effect on Exhaust Emission and Efficiency of a SI Small Engine Fueled with Methane and Gasoline,» *SAE Technical Paper 2020-24-0013*, 2020.
- [17] J. Benajes, R. Novella, J. Gomez-Soriano, P. Martinez-Hernandez, C. Libert e M. Dabiri, «Evaluation of the passive pre-chamber ignition concept for future high compression ratio turbocharged spark-ignition engines,» *Elsevier - Applied Energy*, vol. 248, pp. 576-588, 2019.
- [18] A. Zingarelli, *Analisi sperimentale e numerica di un motore monocilindrico con sistema Passivo Turbulent Jet Ignition (TJI)*, Master Thesis, Politecnico di Torino.
- [19] G. Quattrone, *Turbulent Jet Ignition (TJI) Combustion Modelling in GT-Suite*, Master Thesis, Politecnico di Torino.
- [20] J. Ferziger, M. Peric e R. Street, *computational Methods for Fluid Dynamics*, Springer, 2020.
- [21] Convergent Science, «Converge Studio Manual».
- [22] Y. Wu, P. Pal, S. Som e T. Lu, «A skeletal chemical kinetic mechanism for gasoline and gasoline/ethanol blend surrogates for engine CFD applications,» in *10th International Conference on Chemical Kinetics*, Chicago (USA), 2017.
- [23] N. Morgan, A. Smallbone, A. Bhave, M. Kraft, R. Cracknell e G. Kalghatgi, «Mapping surrogate gasoline compositions into RON/MON space,» *Elsevier - Combustion and Flame*, vol. 157, 2010.
- [24] Z. Han e R. Reitz, «A temperature wall function formulation for variable-density turbulent flows with application to engine convective heat transfer modeling,» *Elsevier - International Journal of Heat and Mass Transfer*, vol. 40, 1997.
- [25] E. Mastorakos, P. Allison, A. Giusti, P. De Oliveira, S. Benekos, Y. Wright, C. Frouzakis e K. Boulouchos, «Fundamental Aspects of Jet Ignition for Natural Gas Engines,» *SAE Int. J. Engines 10(5):2429-2438*, 2017.
- [26] S. Biswas, *Physics of Turbulent Jet Ignition*, Springer, 2018.
- [27] G. Onofrio, P. Napolitano, P. Tunestal e C. Beatrice, «Combustion sensitivity to the nozzle hole size in an active pre-chamber ultra-lean heavy-duty natural gas engine,» *Elsevier - Energy*, vol. 235, 2021.
- [28] *GRI Mechanism; available from: <http://combustion.berkeley.edu/gri-mech/>*.
- [29] J. Kim, R. Scarcelli, S. Som, A. Shah, M. S. Biriduganti e D. E. Longman, «Numerical investigation of a fueled pre-chamber spark-ignition natural gas engine,» *International Journal of Engine Research*, 2021.
- [30] M. Wenig, N. Fogla e K. Roggendorf, «Towards Predictive Dual-Fuel Combustion and Pre-Chamber Modeling for Large Two-Stroke Engines in the Scope of 0D/1D Simulation,» in *CIMAC Congress 2019*, Vancouver, 2019.
- [31] G. Onofrio, C. Li, P. G. Valladolid, J. De la Morena, A. Garcia, P. Tunestal e C. Beatrice, «Experimental and Numerical Assessment of Active Pre-chamber Ignition in Heavy Duty Natural Gas Stationary Engine,» *SAE Technical Paper 2020-01-0819*, 2020.
- [32] E. Distaso, R. Amirante, E. Cassone, F. Catapano, P. De Palma, P. Sementa e P. Tamburrano, «Experimental and Numerical Analysis of a Pre-Chamber Turbulent Jet Ignition Combustion System,» *SAE Technical Paper 2019-24-0018*, 2019.

[33] J. R. Grove, «The Measurement of Quenching Diameters and Their Relation to the Flameproof Grouping of Gases and Vapours,» *I.Chem.E - Symposium Series No. 25* .